MFI ZEOLITE MEMBRANES ON CERAMIC HOLLOW FIBERS: SCALABLE FABRICATION PROCESSES AND HYDROCARBON SEPARATION PROPERTIES

A Dissertation
Presented to
The Academic Faculty

by

Byunghyun Min

In Partial Fulfillment
of the Requirements for the Degree
Doctor of Philosophy in Chemical Engineering
School of Chemical & Biomolecular Engineering

Georgia Institute of Technology
August 2020

MFI ZEOLITE MEMBRANES ON CERAMIC HOLLOW FIBERS: SCALABLE FABRICATION PROCESSES AND HYDROCARBON SEPARATION PROPERTIES

Approved by:

Dr. Sankar Nair, Advisor
School of Chemical & Biomolecular Engineering
Georgia Institute of Technology

Dr. Christopher W. Jones, Co-Advisor
School of Chemical & Biomolecular Engineering
Georgia Institute of Technology

Dr. David S. Sholl
School of Chemical & Biomolecular Engineering
Georgia Institute of Technology

Dr. Sven H. Behrens
School of Chemical & Biomolecular Engineering
Georgia Institute of Technology

Dr. Yongsheng Chen
School of Civil & Environmental Engineering
Georgia Institute of Technology

Date Approved: April 27th , 2020

To my family

Thanks for always being there for me

ACKNOWLEDGEMENTS

I would like to express my sincere appreciation to my advisors, Dr. Sankar Nair and Dr. Christopher. W. Jones, for all persistent guidance, support and continuous encouragement throughout my Ph.D. study. Whenever I encountered failures in research and I was depressed, they convincingly and continually conveyed their enthusiasm and insightful knowledge for my research and led me to do the right thing. I got enriched with much fundamental knowledge and research logic. I believe that working with them will be remembered as a milestone in my professional and personal life. I will never forget every single piece of advice and lesson I learned from them for my entire life.

I would like to thank my committee members, Dr. David S. Sholl, Dr. Sven H. Behrens, and Dr. Yongsheng Chen, for their invaluable and critical input for my research, which led me to think more and develop concrete knowledge. It was a great honor to have these great committee members.

Now I would like to extend my sincere thanks to my collaborators Akshay Korde, Dr. Shaowei Yang, Dr. Kiwon Eum, Dr. Yeon Hye Kwon, and Dr. Hyuk Taek Kwon for their great collaborations and their warmhearted supports for me. I was very lucky that I had the right person at the right time.

Also, many thanks to Nair and Jones research group. I enjoyed every activity and discussion and I was able to enjoy American life and build up good memories with them. It was great to have such warmhearted and intelligent people around me for the last five years. I also thank Korean graduate students at ChBE for sharing their time with me and

giving me an unforgettable memory. I always cheer for their continued success. I would like to also mention my best friends from high school, Bum Jun, Hyungjoo, and Taehwang. Thank you for encouraging me all the time and sharing every joy and sorrow with me. To know that there are friends who, though distant, encourage each other always cheers me up.

I am extremely grateful to my beloved family – father, mother, and a little sister. They are always being there for me. No words can ever be strong enough to express my gratitude to my family for their unconditional love and dedication. I owe all that I have accomplished to my family. I also thank my in-laws. They always trust me and support me, which makes me feel confident.

Finally, I deeply thank my wife, Sukyeong. I am so blessed she came into my life. She comforts me and brings joy to my life. I believe I can do anything no matter how hard it may be. I love you.

TABLE OF CONTENTS

LIST OF TABLES

LIST OF FIGURES

SUMMARY

Low-energy membrane-based separation technologies have the potential to replace or debottleneck current energy-intensive separation processes such as distillation [1]. Of all the interesting membrane materials, zeolites have desirable properties for separation applications including precisely defined pore structures of molecular dimension (0.2 – 2 nm), size/shape selectivity, and thermal/structural/chemical stabilities [2]. In particular, MFI zeolite membranes are attractive for the separation of industrially important hydrocarbon gas mixtures such as xylene isomers [3, 4], butane isomers [5, 6] and natural gas components [7], based on the differences in the chemical and physical properties. The large-scale industrial application of zeolite membrane systems can be realized by overcoming the following barriers: firstly, develop scalable and reliable membrane fabrication strategies to produce the high-performance membrane; secondly, reduce the cost and achieve performance intensification of the membrane system by employing hollow fiber modules with high membrane area per unit volume; and thirdly, obtain a thorough understanding of multicomponent separation behavior in zeolite membranes at industrially interesting conditions. In the above context, the overall focus of my thesis is to develop novel, technologically scalable fabrication strategies to make thin and highly selective MFI zeolite membranes and to understand their synthesis-structure-permeation property relations by a combination of experiment and modeling. My work has focused on the MFI zeolite type, because of its particularly attractive properties for a wide range of hydrocarbon separations.

Chapter 1 presents an overview of state-of-the-art MFI zeolite synthesis including 2D MFI nanosheets, MFI zeolite membrane fabrication, major challenges for zeolite membranes regarding industrial applications, and the principles of molecular transport through zeolite membranes. This chapter provides the required background and rationale for my research.

Chapter 2 presents a discussion on the development of scalable fabrication methods based upon 2D MFI zeolite nanosheets. Coatings of the nanosheets on membrane support materials, followed by hydrothermal treatment to create a continuous zeolite membrane, is an attractive new way to obtain thin (submicron) and defect-free MFI membranes. Such 2D MFI nanosheet-based zeolite membranes have been previously demonstrated on specially engineered silica disk supports and exhibited unprecedented separation performances for xylene isomers and butane isomers. However, this approach does not hold promise for scalable and inexpensive membrane processing. To address this important issue, my research focused on the fabrication of thin (submicron), *b*-oriented, selective MFI zeolite membranes on low-cost ceramic hollow fibers (O.D. 750 μm), starting from 2D MFI nanosheet materials. I have developed a membrane fabrication process that involves two-step hydrothermal treatments with an appropriate choice of structure-directing agents. This fabrication process is effective in improving adhesion of the membrane on the support, closing macroscopic voids/nanoscale gaps between the 2D nanosheets, as well as highly suppressing the overgrowth/twinning of crystals and maintaining a high degree of out-of-plane *b*-orientation. Then, I investigated in detail the relationship of the membrane microstructures with their separation properties for butane isomers.

In chapter 3, I conducted a thorough experimental and modeling investigation of the microstructurally optimized 2D MFI-based hollow fiber membranes for the removal of natural gas liquid (NGL) components from methane. NGL removal from shale gas is a very large-scale and energy-intensive process that currently is done by cryogenic distillation. The influence of feed compositions (unary, binary, ternary, quaternary) and feed pressures (1 – 10 bar) on C_{1-4} hydrocarbon permeation was experimentally investigated, and combined with multicomponent Maxwell-Stefan transport equations integrated with a cross-flow membrane model to generate performance predictions over a range of operating conditions. An interesting outcome of this chapter is the application-specific evaluation of the operating conditions and associated separation performance of MFI hollow fiber membranes.

In chapter 4, the previous insights on MFI hollow fiber membrane fabrication gained in chapter 2 were used to develop an alternative and further simplified membrane synthesis route. Specifically, I introduce a scalable one-step MFI hollow fiber membrane fabrication process which does not require an initial seeding or nanosheet coating step. The use of highly concentrated precursor gels containing MFI nanocrystals enables the formation of continuous MFI films in one step by promoting the fast formation of a high density of nuclei and inducing heterogeneous crystallization in the vicinity of the support. The membranes prepared from this method outperform previous MFI membranes prepared by the previously developed multiple-step methods. Furthermore, the successful demonstration of simultaneous synthesis of multiple membranes (10 ea) in a single batch and their applications for butane isomers separation and removal of NGL components (*n*-butane, propane, ethane) from methane demonstrates their pressure-stable high-quality

microstructures and the scalability of the method. An additional variation of this one-step method, i.e. solid-gel vapor-phase crystallization is also developed and discussed.

In summary, my work has moved zeolite MFI membrane fabrication science and technology to a new level of scalability and practical feasibility. It has considerable potential to enable technological implementation of thin and highly selective MFI zeolite membranes for the separation of industrially important hydrocarbons.

CHAPTER 1. INTRODUCTION

1.1 Energy-efficient Membrane Separation Technology

Separation technologies are ubiquitous in the chemical, petroleum refining, and materials processing industries and they account for about 4,500 TBtu/yr energy use (22 % of all industrial sector in-plant energy use) in the United States [8]. Since the traditional separation processes utilized in the industrial section such as distillation are energy-intensive thermally-driven processes, there are potential opportunities for implementing energy-saving separation technologies that can separate the molecules based on the differences in the chemical and physical properties [1]. Such low-energy separation by membranes, sorption, and hybrid system (e.g. membrane-distillation) (**Figure 1.1**) have become emerging technologies in the last few decades but they are yet underdeveloped to be utilized. My research of interest is the membrane-based separation technology which can be scalable due to their compactness and modular design. The successful industrial implementation of the membrane separation process requires developing scalable membrane material manufacturing strategies along with quality control and thorough understanding of operating conditions.

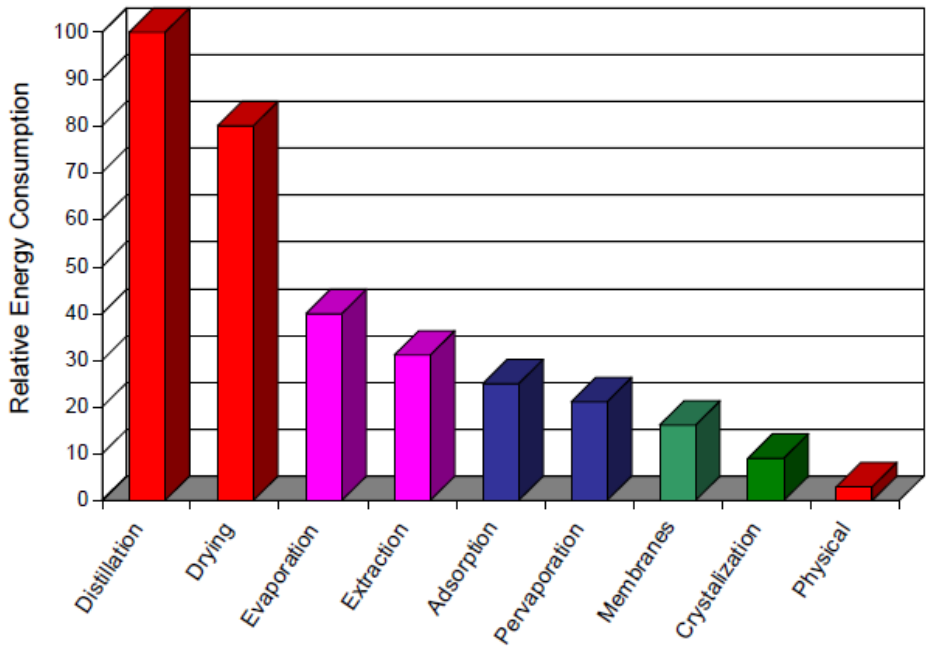

Figure 1.1 Relative energy consumption by various separation processes (adapted from [8])

1.2 Zeolite Membrane-based Separation Technology

Zeolites are microporous aluminosilicate crystalline materials that are mainly constructed from Si, Al and O. So far, over 200 different types of zeolite frameworks have been discovered and each of them can be discriminated by its unique pore size, shape, and volume. Common features of the zeolites are as follows: (1) uniformly and precisely defined pore structures of molecular dimension (0.2 – 2 nm), (2) size and shape selectivity, (3) thermal, structural, chemical stabilities and (4) ion-exchange properties [2]. These properties allow zeolites' applications in adsorptions [9], catalysis [10], corrosion-resistant coatings [11], dielectric films [12] and membrane separations [3-6, 13-16].

Of all the interesting applications, zeolite membrane-based separations have been extensively studied in the previous researches [17-20] because they can potentially provide alternatives to energy-intensive industrial separation processes such as distillation by constituting a stand-alone membrane process or hybrid membrane/distillation process[1, 21]. Membrane-base separation operated non-thermally would use 90% less energy compared to the conventional heat-driven distillation process [2]. Among several candidates for the membrane materials, zeolite membranes offer desirable features such as chemical/structural robustness, high permeability, and high separation selectivity originated from precisely defined nanometer level pore structures in contrast to polymer-based membranes [22]. With the zeolite membranes, it is feasible in principle to separate the gas mixtures by their molecular characteristics, such as adsorption strength and molecular size [1].

1.2.1 MFI Zeolite Membranes and Their Applications

Compared to other membrane materials, MFI zeolites have been the focus of the majority of the research in the membrane separation fields because they possess suitable pore size in the range of industrially relevant important molecules such as xylene isomers and butane isomers. Also, they have a strong adsorptive affinity toward some of the hydrocarbon components present in natural gas, thus providing the potential for natural gas processing. MFI zeolite framework has straight channels with a pore size of 0.54 nm × 0.56 nm along the crystallographic *b*-axis and zig-zag channels with a pore size of 0.51 × 0.55 nm along crystallographic a-axis (**Figure 1.2**) [23]. Those *b*- and *a*-axis channels are

interconnected with each other, therefore *c*-axis channels are also accessible and molecules can diffuse through.

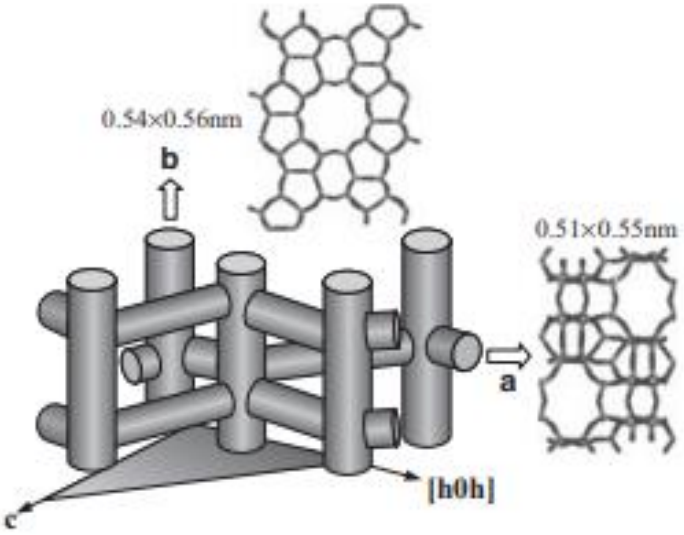

Figure 1.2 Schematic of the pore structure of the MFI zeolite (adapted from [23])

MFI zeolites have been extensively studied and shown good separation capabilities at laboratory scale for various separation applications such as xylene isomers [3, 4], butane isomers [5, 6], natural gas processing [7], CO_2 removal [14-16], and ethanol/water separations [13]. Here are some details on butane isomers separation and extraction of higher hydrocarbons from natural gas streams.

Separation of *n*-butane from *i*-butane is one of the important industrial separations, currently carried out by the distillation process. *n*-Butane is primarily used in liquefied petroleum gas (LPG) as a heating/transportation fuel. The main uses of *i*-butane are as a refrigerant that is less harmful to the environment, and in refineries as a feedstock to the alkylation unit for the production of plastics. Separation of butane isomers will become more critical, particularly since the global butane market size is expected to substantially

grow from US$ 84 billion in 2018 to US$ 156 billion by the end of 2027 with a CAGR (Compound Annual Growth Rate) of 7.1 % from 2019 to 2027, in terms of value [24].

Separation of natural gas liquids (NGL) from methane is one of the important natural gas processing steps to produce pure methane fuel and to avoid condensation issues from higher hydrocarbon during transportation. NGLs are essentially the higher hydrocarbons (C_2 and higher) present in natural gas (including shale gas). Also, NGL components have considerably high economic value when they are sold separately [25]. Moreover, US natural gas production has increased substantially since 2007 with the development of extraction of shale gas and it is predicted that demand will rise by 10 % to 2040 [26]. Currently, removing higher hydrocarbons (C_{2+}) relies on the energy-demanding cryogenic expansion process followed by fractionation. These separation processes, which cannot easily be performed by conventional polymeric membranes, offer important opportunities for the application of zeolite membrane separation technology.

1.2.2 2D MFI Nanosheets for the Membrane Applications

In 2009, multilamellar MFI was synthesized by Choi. et al. [27] using a specially designed di-quaternary ammonium-type surfactant, $C_{22}H_{45}$-$N^+(CH_3)_2$-C_6H_{12}-$N^+(CH_3)_2$-C_6H_{13} ($C_{22\text{-}6\text{-}6}$) (**Figure 1.3**). The $C_{22\text{-}6\text{-}6}$ surfactant is composed of a long alkyl chain group (C_{22}) and two quaternary ammonium groups spaced by a C_6 alkyl linkage. With the $C_{22\text{-}6\text{-}6}$, the di-quaternary ammonium groups act as structure-directing agent (SDA) for the MFI zeolite and the hydrophobic interaction between the long alkyl chain restricts the crystal growth along the *b*-axis, resulting in the multilamellar layered MFI zeolite. This

multilamellar MFI was then exfoliated by the melt-blending method into the individual MFI nanosheets with straight pore channels on the surface, nanometre-scale thickness and high-aspect-ratio by Varoon. et al. in 2011 [28]. Then, the exfoliated MFI nanosheets were dispersed in water and deposited on the porous alumina disk support by vacuum filtration. This initial 2D MFI layer is then intergrown into the ultrathin and highly *b*-oriented MFI membranes via secondary growth (**Figure 1.4**). The obtained MFI membranes after single secondary growth exhibited very high separation performances for xylene and butane isomers.

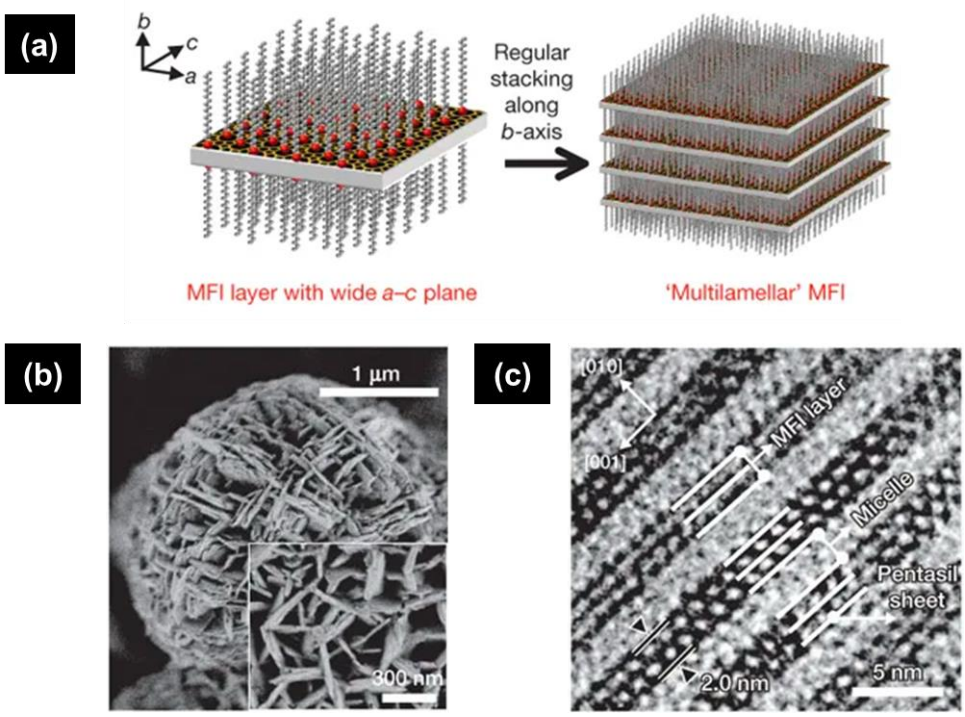

Figure 1.3 (a) Schematic drawing of the SDA alignment along the straight channel of the MFI framework and multilamellar stacking of the MFI nanosheets, (b) SEM image of the multilamerllar MFI zeolite, (c) TEM image showing multilamellar stacking of alternating layers of MFI nanosheets and surfactant micelle (reproduced from [27])

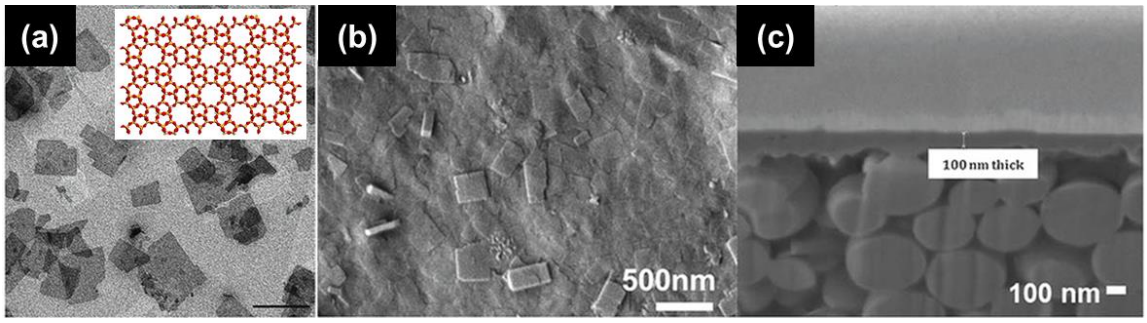

Figure 1.4 (a) TEM image of the exfoliated MFI nanosheets along with (inset) schematic of MFI nanosheet viewed along with the *b*-axis, (b) top and (c) cross-section SEM images of the MFI nanosheets-based membranes (reproduced from [28, 35])

However, the exfoliation of the layered MFI requires multiple processes based on the exfoliation by melt-blending, followed by purification to remove non-exfoliated particles. This is a time-consuming and low-yield process and it produces fragmented nanosheets of small lateral dimensions (few hundred nanometers). In 2017, Jeon. et al. reported the direct synthesis approach. In this work, high-aspect-ratio MFI nanosheets were synthesized by a rotational intergrowth from MFI nanocrystals triggered by a specially designed structure-directing agent (**Figure 1.5**). 2D MFI nanosheets have a 1.5 – 2.0 µm lateral dimension with nanometre-scale thickness along the *b*-axis and the straight micropores are present on the surface of the nanosheets [29]. This bottom-up seed-based approach provides advantages over previous exfoliation method such as higher yield and increased lateral dimension. Therefore, these 2D MFI nanosheets were found to be favorable for fabricating uniform seed layer coatings and high-quality membranes.

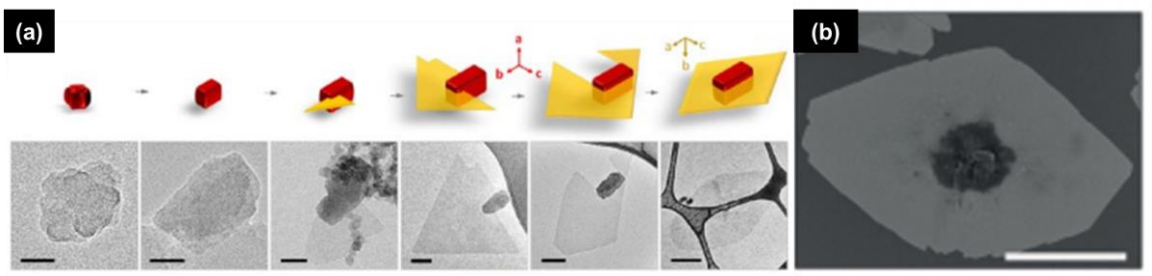

Figure 1.5 (a) Schematic and the corresponding TEM images representing growth stages of MFI nanosheet from seed (b) SEM image of MFI nanosheet. Scale bars from left to right in (a) are 20 nm, 20 nm, 50 nm, 100 nm, 100 nm, and 500 nm, in (b) is 1 µm (reproduced from [29,65])

1.2.3 MFI Zeolite Membrane Fabrication Methods

There are three methods for the preparation of the zeolite membranes on porous support: the secondary growth method, the in situ growth method, and the direct deposition-based method. In the secondary growth method, the porous support is firstly coated with a layer of zeolite seed crystals then followed by secondary growth to form a continuous membrane by closing intercrystalline gaps in a hydrothermal process [30]. Using the secondary growth technique, it is possible to manipulate the microstructures of the membrane such as the orientation and the thickness by using anisotropic zeolite seed crystals (e.g. 2D MFI nanosheets) and precise optimization of the synthesis conditions [31].

In the in situ growth method, the porous support is directly contacted with the zeolite precursor sol and then subjected to a hydrothermal reaction to promote the nucleation and crystal growth on the surface of the support. The zeolite film can be formed in one step without a separate seeding step. Despite this method is simple, multiple fabrication steps are still required including the modification of the support and repeated hydrothermal reactions. Since it is difficult to induce a high density of nuclei due to the

absence of the seed layer, it generally requires multiple hydrothermal reactions until the membrane is fully intergrown. As a result, the in situ growth method leads to very thick membranes and thus increased resistance to molecular transport [32].

Recently, the MFI membrane was fabricated by the direct deposition of 2D MFI nanosheets on the low-cost polymer support without the secondary growth [33]. The multilamellar MFI was exfoliated by the melt-blending method and then treated with an acidic solution to remove the SDA. The SDA-free 2D MFI nanosheets were then dispersed in water and deposited on the porous polymer support by a filtration. The coating exhibits separation performance that is characteristic of MFI membranes, with an *n*-butane/*i*-butane separation selectivity of 5. This is the first demonstration of the MFI membranes without a hydrothermal reaction. However, it shows relatively lower separation performances compared to typical MFI membranes and it still requires several complex processes.

1.2.4 Challenges in Commercialization of Zeolite Membranes

Despite the attractive features of zeolite membranes for separation applications, so far only small-pore hydrophilic NaA zeolite membranes were successfully commercialized for the dehydration of organic solvents (EtOH, IPA, MeOH, etc) [34]. It has been found that aqueous and other liquid-phase environments are quite ‘forgiving’ of defects in scaled-up zeolite membranes (due to condensation of liquids in the defects leading to their partial sealing during operation). Conversely, other types of zeolite membranes including MFI membranes have been unsuccessful in achieving economic viability for industrial-scale gas

separation applications due to the challenges in scalable, reproducible and quality-controlled fabrication strategies.

At the same time, many advances have been achieved so far, including control over preferential pore orientation/the thickness [20, 35, 36], elimination of grain boundaries/defects [37], healing of the defects [38-40] and developing cost-effective fabrication methods such as in situ [41, 42] or gel-free crystallization methods [36] as stated earlier. However, despite these advances the estimated production cost of zeolite MFI membranes remains high (> \$1000/m^2 membrane area) [43, 44]. A large fraction (often more than 75%) of the fabrication cost is accounted for by the support material, an issue that has hindered industrial applications of MFI zeolite membranes for separation. Zeolite membranes are usually required to be grown on macroporous ceramic supports such as silica and alumina, one reason being that they have to be calcined at temperatures > 773 K to remove the organic structure directing agents (templates) and activate their porosity. On a laboratory scale, it is common to use the support in disk or tubular geometries, which are very expensive to fabricate by compaction and extrusion processes. Also, the macroporous surface of the support is often not suitable for growing high-quality zeolite films. Therefore, it is typical to specially engineer the support by forming a thin gutter layer with smaller pores by additional steps including slip-casting [45] or vacuum-coating [46], thus resulting in the increased production costs of the support itself. Furthermore, membrane packing density (the ratio of the membrane area to the packing volume) and membrane surface to volume ratio are the one of the critical parameters to reduce the engineering and installation costs. Unlike the flat sheet configuration, the main advantages of the hollow fiber module are high packing density (500 – 9,000 m^2/m^3) [47] high membrane surface to

volume ratio and low-energy consumption. The membrane surface to volume ratio is about 300-500 m^2/m^3 for plate module and about 6,000-13,000 m^2/m^3 for hollow fiber module [48].

Therefore, it is highly required to develop the cost-effective zeolite membrane fabrication strategies that can be applied to the mass-producible low-cost hollow fiber supports while allowing the quality-control of the membranes.

1.3 Transport Mechanisms in Zeolite Membranes

Industrial implementation of the membrane system should involve the understanding of the permeation behaviors and optimization of the operating conditions.

Zeolite membranes can separate the mixtures by the combined effect of adsorption and diffusion characteristics. The permeation of gases across the membrane is governed by both the diffusion and the concentration gradient of the species across the membrane [49]. The process of the mass transport through a zeolite membrane (**Figure 1.6**) is as follows [50]

1. Mass transfer from the bulk gas phase through a stagnant gas film near the membrane surface
2. Mass transfer from the surface of the membrane to zeolitic pores by a sorption process
3. Diffusion through the microporous region
4. Desorption at the micropore exit to the bulk

Therefore, in order to understand the gas transport through the zeolite membrane, adsorption/desorption of species from the zeolite membranes and diffusion through the microporous zeolitic pores need to be considered

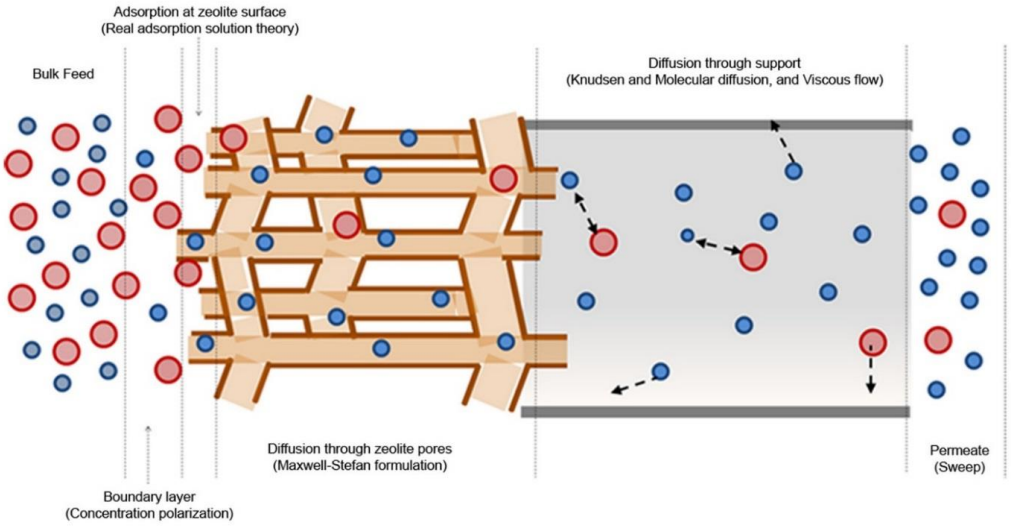

Figure 1.6 Schematic of a permeation of species through the zeolite membranes from bulk feed to permeate (adapted from [21])

1.3.1 Multicomponent Adsorption

To describe the adsorption of gas mixtures in micropores, two different approaches can be employed.

First, the dual-site Langmuir (DSL) model for the single-component adsorption can be extended to a multicomponent mixture case. It is well known that the DSL model provides an excellent fit for the adsorption isotherms of hydrocarbons in MFI since the MFI framework includes two different sorption sites like intersection and straight channel. Using the parameters given by the single-component adsorption isotherm fitting to the dual-site Langmuir (DSL) isotherm model (Equation (1)), the mixture adsorption loadings

are predicted by the extended dual-site Langmuir (EDSL) model. The adsorbed loading of component i (q_i) in a mixture is obtained by Equation (2) [51, 52].

$$q_i = q_{iA}^{sat} \frac{K_{iA} P_i}{1 + K_{iA} P_i} + q_{iB}^{sat} \frac{K_{iB} P_i}{1 + K_{iB} P_i} \quad (1)$$

$$q_i = q_{iA}^{sat} \frac{K_{iA} p_i}{1 + \sum_{i=1}^{n} K_{iA} p_i} + q_{iB}^{sat} \frac{K_{iB} p_i}{1 + \sum_{i=1}^{n} K_{iB} p_i} \quad (2)$$

where A or B represents the two different sites, q_i^{sat} is saturation loading of component i (mol.kg^{-1}), K_i is parameter in the Langmuir adsorption isotherm (Pa^{-1}), P_i is the pressure (Pa), and p_i is the partial pressure (Pa).

Second, the ideal adsorbed solution theory (IAST) [53] can predict the multicomponent adsorption by using parameters obtained from the DSL model. IAST is another widely used theory for estimation of the multicomponent adsorption behavior. It assumes that the gas phase and adsorbed phase are in equilibrium and the adsorbed phase follows Raoult's law.

The solutions to the IAST model can be obtained by solving a system of non-linear equations (Equation (3) to Equation (6)) [54]

The reduced spreading pressure, π_i^* (Equation (3)), can be defined as

$$\pi_i^* = \frac{\pi_i A}{RT} = \int_0^{P_i^0} \frac{q_i^0(P)}{P} dP \quad (3)$$

where π is the spreading pressure (kg.m.s^{-2}.m^{-1}), R is the gas constant (8.314 m^3.Pa.K^{-1}.mol^{-1}), T is the temperature (K), A is the surface area per kg of zeolite (m^2.kg^{-1}), P_i^0 is the pressure of component i in the gas phase (Pa), q_i^0 is the adsorption isotherm of pure component i (mol.kg^{-1}), and P is the total pressure (Pa).

For ideal mixtures, P_i^0 satisfies Raoult's law and follows the Equation (4),

$$y_i P = x_i P_i^0 \tag{4}$$

where y_i represents the adsorbed phase and x_i is the molar fraction of i in the gas phase. P and P_i^0 are total pressure (Pa) and pressure of component i in the gas phase (Pa), respectively. The spreading pressure can be expressed as a function of y_i, x_i or P_i^0.

The thermodynamic state is obtained by solving the Equation (5),

$$\pi_1^* = \pi_2^* = \pi_3^* = \cdots = \pi_N^* \tag{5}$$

The total amount adsorbed for the mixture, n_t, is given by the Equation (6) with the constraint of $\sum_i x_i = 1$.

$$\frac{1}{n_t} = \sum_{i=1}^{N} \left[\frac{x_i}{n_i^0(P_i^0)} \right] \tag{6}$$

IAST is a thermodynamically consistent model and it can take into account the size exclusion in the competitive adsorption of different species, while the EDSL model cannot.

Adsorption separation factor (AS) can be defined as the ratio of mole fractions of more adsorbing component i and less adsorbing component j in the adsorbed phase divided by the same ratio of mole fractions in the gas phase (Equation (7)).

$$AS_{ij} = \frac{y_i/y_j}{x_i/x_j} \tag{7}$$

1.3.2 Multicomponent Mass Transport

For the description of the mass transport of a multicomponent mixture through the zeolite membrane, the interplay between adsorption and diffusion and the correlation effects in species diffusion need to be considered [55]. It is widely accepted that the M-S equation provides a proper description of the multicomponent transport in the zeolite membrane [55, 56].

First, I will introduce the Fick's law for a single component diffusion. Fick's law for describing the diffusion of a single component is expressed as Equation (8).

$$N_i = -\rho D_i \nabla q_i \tag{8}$$

where N_i is molecular flux of component i (mol.m^{-2}.s^{-1}), ρ is density of the membrane (kg m^{-3}), D_i is the Fick diffusivity (also called as transport diffusivity) (m^2.s^{-1}), and q_i is the molecular loading (mol.kg^{-1}).

While Fick's law is valid for gas mixtures at low to moderate pressures, it fails to capture non-ideality effects and it is not appropriate to account for the multicomponent diffusion in a non-dilute system.

The M-S diffusion model is considered more comprehensive than Fick's law since it provides the kinetic and equilibrium contributions separately and takes account of thermodynamic non-ideality arising from the interaction between adsorbed species [57]. Therefore, the M-S equation is more useful for describing the multicomponent diffusion considering the inter-related diffusion and sorption.

The M-S formulation for a single component diffusion is expressed as Equation (9).

$$N_i = -\rho q_i^{sat} Đ_i \left(\frac{\theta_i}{RT} \nabla \mu_i\right) \tag{9}$$

where N_i is molecular flux of component i (mol.m^{-2}.s^{-1}), ρ is density of the membrane (kg m^{-3}), q_i^{sat} is saturation loading (mol.kg^{-1}), $Đ_i$ is the M-S diffusivity (m^2.s^{-1}), θ_i is fractional occupancy of species, R is the gas constant (8.314 J.mol^{-1}.K^{-1}), T is the temperature (K), μ_i is molar chemical potential of the adsorbed component (J.mol^{-1}).

In the M-S formulation, the chemical potential is the driving force for diffusion, and it is expressed in terms of the gradients of the occupancy ($\nabla\theta_i$) (Equation (10)-(11)).

$$\frac{\theta_i}{RT} \nabla \mu_i = \Gamma \nabla \theta_i \tag{10}$$

$$\Gamma \equiv \theta_i \frac{\partial ln p_i}{\partial \theta_i} \tag{11}$$

Here, thermodynamic correction factor (Γ) is introduced which portrays the non-ideal behavior and it depicts the relationship between the Fick diffusivity (D_i) and the M-S diffusivity ($Đ_i$) as Equation (12).

$$D_i = Đ_i \Gamma \tag{12}$$

The M-S diffusivity is the thermodynamically corrected diffusivity describing the jump frequency of species hopping from site to site [58]. For the limiting cases such as gas mixtures at low to moderate pressures, the thermodynamic correction factor is equal to 1 (the mixture is thermodynamically ideal) and M-S diffusivity and Fick diffusivity are identical to each other [59].

M-S formulation for describing the permeation of multicomponent in zeolite can be written as Equation (13) [60].

$$-\rho \frac{\theta_i}{RT} \nabla \mu_i = \sum_{j=1, j \neq i}^{n} \frac{q_j N_i - q_i N_j}{q_i^{sat} \, q_j^{sat} Đ_{ij}} + \frac{N_i}{q_i^{sat} Đ_i} \tag{13}$$

where ρ is density of the membrane (kg.m^{-3}), θ_i is fractional occupancy of species, R is the gas constant (8.314 J.mol^{-1}.K^{-1}), T is the temperature (K), μ_i is molar chemical potential (J.mol^{-1}), q_i is the molecular loading (mol.kg^{-1}), q_i^{sat} is saturation loading (mol.kg^{-1}), N_i is the molar flux of species (mol.m^{-2}.s^{-1}), $Đ_i$ is the M-S diffusivity (m^2.s^{-1}).

There are two types of M-S diffusivities, $Đ_i$ and $Đ_{ij}$, in the formulation. The pure component M-S diffusivity ($Đ_i$) corresponds to the diffusivities for each gas molecules in single component diffusion. The counter-exchange diffusivity ($Đ_{ij}$) corresponds to the

diffusivities associated with the interaction between two different gas species. In the case of MFI zeolite, counter-exchange between species cannot be neglected. Due to this counter-exchange, weakly absorbing but faster species can be slowed down by permeation of species which is highly absorbing but less mobile. The counter-exchange diffusivity can be estimated based on information from the pure component diffusivity using the empirical correlation based on the Vignes relationship (Equation (14)) [51, 61].

$$Đ_{ij} = Đ_i^{\theta_i/(\theta_i+\theta_j)} Đ_j^{\theta_j/(\theta_i+\theta_j)} \tag{14}$$

The chemical potential gradients ($\nabla\mu_i$) in the M-S formulation for a multicomponent diffusion is expressed in terms of the gradients of the occupancies (θ_i) (Equation (15)-(16)).

$$\frac{\theta_i}{RT}\nabla\mu_i = \sum_{j=1}^{n} \Gamma_{ij}\nabla\theta_j \tag{15}$$

$$\Gamma_{ij} \equiv \left(\frac{q_j^{sat}}{q_i^{sat}}\right)\frac{q_i}{p_i}\frac{\partial p_i}{\partial q_j} \tag{16}$$

Equation (13)-(16) then can be casted into the matrix form. More details will be provided in **3.3 Modeling Methods**.

1.3.3 Gas Permeation in the Zeolite Membranes

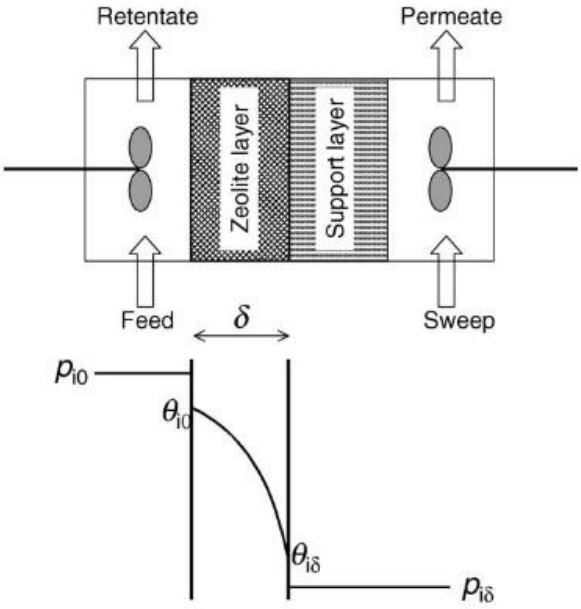

Figure 1.7 Schematic of zeolite membrane separation device and loading profile within the zeolite membrane (adapted from [55])

Schematic description of the zeolite membrane separation device and loading profile within the zeolite membrane is given in **Figure 1.7**. The zeolite membrane layer is generally facing the feed side and the permeate side is purged to keep the low partial pressures and maintain the driving force across the membrane layer.

The permeance is the flux divided by the partial pressure driving force across the membrane given by Equation (17)

$$Permeance = \frac{Flux}{\Delta p}\ (mol.m^{-2}.s^{-1}.Pa^{-1}) \tag{17}$$

where flux is the gas molar flow through the membrane (mol.m^{-2}.s^{-1}), Δp is the pressure difference across the membrane (Pa).

The ideal selectivity (*IS*) is the ratio of the permeance of two different gas species obtained when they permeate through the membrane independently (Equation (18)).

$$IS_{ij} = \frac{P_i}{P_j} \tag{18}$$

where P_i and P_j are the permeance (mol.m^{-2}.Pa^{-1}.s^{-1}) of the gas species *i* and *j* respectively obtained from single gas permeation measurement.

For a mixture of gases, the separation factor (*SF*) is the ratio of the mole fractions of the more permeable gas and the less permeable gas in the permeate divided by the same ratio of mole fractions in the feed (Equation (19)).

$$SF_{ij} = \frac{{y_i}/{y_j}}{{x_i}/{x_j}} \tag{19}$$

where y and x represent the percentage concentration in the permeate and feed side.

1.4 Impact of This Work

Key findings and advances in this thesis are presented as follows.

Firstly, I develop the sequential hydrothermal treatment methodology for the scalable fabrication of the 2D MFI nanosheet-based membranes on simple and low-cost macroporous supports. This achievement includes the uniform 2D MFI nanosheet coating via vacuum filtration on a α-alumina hollow fiber support and the sequential hydrothermal treatments with the selected SDAs (TPA-Fluoride, TEAOH) while eliminating the multiple manufacturing steps required for the support itself. In particular, I observe the microstructural characteristic changes such as degree of interparticle gaps, pore orientation, and thickness at each synthesis stage and investigate the relationship of synthesis-microstructure-permeation property. These findings can provide insight for utilizing zeolite nanosheets to enable the scale-up of thin and highly selective zeolite membranes.

Second, this work extends the application of the as-developed 2D MFI hollow fiber membranes to the removal of natural gas liquid (NGL) components (*n*-butane, propane, ethane) from methane. I demonstrate excellent separation performances in multicomponent (binary, ternary, quaternary) hydrocarbon mixtures at elevated pressure (1 - 10 bar) and investigate the permeation behaviors at such different operating conditions combined with the experimental and modeling approach. Maxwell-Stefan modeling provides qualitative predictions of the separation performances of the present membrane under a wide range of operating conditions (e.g. feed pressures, feed compositions, sweep effect) that is essential to the successful transfer of the membrane separation technology to industrial applications.

Third, I present the pseudo in situ membrane fabrication methodology for the scalable fabrication of high-quality MFI membranes. This achievement includes the preparation of the highly concentrated precursor gel containing MFI nanocrystals and subsequent one-time crystallization. This enables thin (~ 1 μm) and highly selective MFI membranes on low-cost macroporous supports without a separate seeding step. The scalability and reliability of the current approach are demonstrated by a simultaneous multiple membrane (10 ea) synthesis. I further extend this method toward the vapor-phase crystallization method which has the potential to provide more scalability regardless of support geometries and reduce manufacturing cost and environmental impacts. I establish synthesis-microstructure-permeation property relations of both liquid-, vapor-based approaches according to important synthesis parameters. This provides insights for cost-effective membrane growth under such conditions and demonstrates the versatility of our new methodology.

Overall, this work will significantly contribute to the implementation of the advanced membrane separation technologies in the chemical industries that would provide a substantial reduction in energy consumption and capital cost.

CHAPTER 2. SYNTHESIS OF MFI HOLLOW FIBER MEMBRANES FROM 2D MFI NANOSHEETS AND PERMEATION PROPERTIES OF BUTANE ISOEMRS[1]

2.1 Introduction

Membrane-based separations have high potential for energy efficiency and cost reduction in chemical processes. Inorganic molecular sieving zeolite membranes [62, 63] can offer a number of advantages such high permeability and selectivity as well as excellent thermal and chemical stability in many applications. However, the difficulty of low-cost and scalable fabrication of zeolite membranes is a key barrier to their widespread application. In the last few years, the emergence of zeolitic membranes based upon 2-dimensional (2D) zeolite nanosheets [29] has created an opportunity to overcome this barrier. In principle, one can deposit uniform and thin (0.1-1 μm) coatings of high-aspect ratio zeolite nanosheets on nearly any kind of porous membrane substrate and then perform a final zeolite growth step to close the nanoscopic gaps between the nanosheets, thereby creating very high-flux molecular sieving membranes. For example, nanosheets (3-5 nm in thickness) of zeolite MFI have been synthesized both by exfoliation of 2D MFI layered stacks [28, 46, 64] as well as by seed-assisted bottom-up methods [29]. The MFI nanosheets produced by the latter route offer particularly attractive structural features such as a very high aspect ratio favorable for thin coatings, very short diffusion pathways through the nanosheet, high-yield production without need for an exfoliation process, and good dispersibility in water. MFI membranes fabricated from theses MFI nanosheets have shown high fluxes and excellent separation of xylene isomers and also of butane isomers

[29, 65]. Despite the excellent separation performance of the above MFI membranes, their current fabrication process faces considerable hurdles in practical feasibility and scalability. At present the fabrication process is only possible on porous Stöber silica-derived disk-type supports. It has been hypothesized that such a support provides an optimal delivery of silicate reactants to the 2D MFI nanosheet coating and facilitates its growth into a defect-free membrane, and its properties are difficult to replicate with other types of silica-containing supports [35, 36]. However, Stöber silica disk supports are difficult to fabricate, and their fabrication in the form of tubular or hollow fiber supports is even more challenging.

Therefore, the next key challenge is to be able to fabricate 2D MFI nanosheet-based membranes on simple and scalable macroporous supports that do not require any surface engineering and can be produced at low cost. This is a significant issue because new processes for 2D MFI nanosheet coating and MFI membrane fabrication must be developed, due to the fact that silicate reactants can no longer be obtained from the underlying support. Inorganic (specifically α-alumina) hollow fiber supports are of particular interest because of their high packing density (membrane surface area/volume ratio of 1,000-10,000 m^2/m^3), excellent chemical and thermal stability, and good mechanical strength under ordinary processing conditions. The Nair group has recently demonstrated examples of fabrication of high-quality zeolitic gas separation membranes on 750 μm OD α-alumina hollow fibers produced in-house [66, 67]. Here I demonstrate a method for fabrication of selective MFI membranes based upon 2D MFI nanosheets, on α-alumina hollow fibers. This method allows preparation of continuous 2D MFI nanosheet coatings on the hollow fibers, and subsequently the selective sealing of microscale/nanoscale gaps between nanosheets while

preserving the preferred (0*k*0) out-of-plane orientation and maintaining a low membrane thickness of <800 nm. The resulting MFI hollow fiber membranes retain the same high fluxes and butane isomers separation selectivities as those prepared by previous authors on silica disk supports.

2.2 Experimental Methods

2.2.1 Materials

For MFI nanosheet crystal and membrane preparation, tetraethyl orthosilicate, tetraethylammonium hydroxide solution (35 %), hydrofluoric acid (40-45 %), potassium chloride and LUDOX SM-30 colloidal silica (30 %) were purchased from Sigma-Aldrich. Potassium hydroxide was purchased from Merck. Sulfuric acid (95-97 %) and tetrapropylammonium hydroxide solution (40 %) were purchased from EMD Millipore.

2.2.2 Preparation of α-Alumina Hollow Fibers

The preparation of α-alumina hollow fibers generally followed our recent work [66] with a slight change of the alumina powder source (changed to Baikalox CR6, average particle size of 500 nm) and sintering temperature (changed to 873 K). The spinning dope suspension had a composition (wt.%) of 38.0 NMP: 6.8 PES: 54.7 Al_2O_3: 0.5 PVP. Hollow fiber spinning was conducted at Georgia Tech with an apparatus constructed in-house. Dope and bore fluid flow rates of 120 and 80 mL/h respectively were used. Deionized (DI) water and tap water were used as the bore fluid and external coagulant fluids respectively. Both the dope and water bath were at room temperature. The air gap was 3 cm. The fibers fell freely into the water bath bucket and were collected, soaked in DI water for 3 days

(with the water changed daily) to exchange the residual solvent, and thoroughly dried. The raw/"green" fibers were then sintered at 873 K for 2 h followed by 6 h at 1673 K with a temperature ramping rate of 5 K/min. The finished fibers were of 750 µm OD, 150 µm wall thickness, 46 % porosity, and 259 nm average limiting pore size and 835 nm finger-like internal voids as obtained from mercury porosimetry. Their N_2 permeance at 298 K was ~200,000 GPU.

2.2.3 Preparation of 2D MFI Nanosheet Suspension

MFI nanosheets were synthesized by bottom-up synthesis as reported by previous authors, with minor modifications. Firstly, bis-1,5(tripropyl ammonium) pentamethylene diiodide (dC5) and MFI seed nanocrystals were synthesized as reported by Jeon et al [29]. MFI nanosheets were synthesized with the precursor sol composition of 80 TEOS : 3.75 dC5 : 20 KOH : 9500 H_2O : 5 H_2SO_4. The precursor sol was hydrolyzed at room temperature for 16 h and filtered through a 0.45 µm syringe filter. The filtered precursor sol was then mixed with the as-prepared MFI seed nanocrystals with the silica content in the seed suspension and the gel being in a 1:200 molar ratio. Then, the mixture was poured into a Teflon-lined stainless-steel autoclave and subjected to hydrothermal treatment at 413 K) for 7 days. The as-synthesized products typically contain 2D MFI nanosheets with negligible amounts of an amorphous phase. Typically, 2.5 g of as-obtained product was mixed with 2.5 g of an alkaline salt solution (0.1 M KOH + 2 M KCl) and stirred at 600 rpm. After stirring for 8 h, it was diluted with 15 mL of H_2O and then centrifugated at 8500 rpm for 5 min. After decantation of the supernatant, the recovered sediment was re-dispersed in H_2O. The above procedure was repeated 3 times. Finally, the MFI nanosheet sediment was dispersed in H_2O with the concentration of 0.01 wt% or 0.02 wt%.

2.2.4 Nanosheet Coating on α-Alumina Hollow Fibers

The MFI nanosheet suspension was sonicated several times (1 min each time) to ensure complete dispersion. Nanosheet coatings were made on hollow fibers by a vacuum filtration process as shown in **Figure 2.3**. One tip of the fiber was sealed by epoxy (3M-DP 100) to prevent infiltration of liquid, and the other tip was connected to a PTFE tube by epoxy. The other tip of the homemade tube was connected to vacuum pump through a Swagelok fitting. The alumina hollow fiber was immersed into the MFI nanosheet suspension under bore-side vacuum for the desired time (typically 30 s) in order to deposit the nanosheet coating on the outer surface ("shell side"). Then the fibers were dried under vacuum for 5 min, followed by calcination (353 K for 6 h and 823 K for 4 h, with ramping rate of 2 K/min).

2.2.5 Hydrothermal Growth of 2D MFI Nanosheet Layer

The calcined MFI nanosheet coatings on the hollow fibers were treated by two sequential hydrothermal growths. In the fluoride-medium "secondary growth", a sol with a 1 SiO_2 : 0.02 Na_2O : 0.12 TPAOH : 0.12 HF : 60 H_2O molar composition was hydrolyzed for 16 h (Na_2O content is from LUDOX SM-30 colloidal silica source). The MFI nanosheet coated fibers were then immersed in the sol and treated hydrothermally in an autoclave at 373 K for 12 h. These initial membranes were rinsed with a 0.2 M ammonia solution and dried at 353 K overnight. To evaluate the membrane properties at this stage, calcination was carried out at 753 K for 4 h with a ramping rate of 0.5 K/min before permeation measurements. However, uncalcined membranes were used for the subsequent "tertiary growth". A sol with molar composition 1 TEOS : 0.3 TEAOH : 100 H_2O was hydrolyzed

for 16 h and the membranes were treated hydrothermally in this sol at 443 K for 48 h. After this step, the final membranes were rinsed, dried and calcined as above.

2.2.6 Characterizations

Surface and cross-section SEM images of the membranes were collected with a Hitachi SU 8010 scanning electron microscope. XRD patterns were measured at room temperature on a PANalytical X'Pert Pro diffractometer equipped with an incident beam monochromator, so that only the Kα1 radiation was used (scan step size: 2theta = 0.004°). The thin membrane supported on a α-alumina hollow fiber was difficult to characterize with reflection (Bragg-Brentano) XRD analysis due to its curvature. To obtain sharper XRD patterns, membranes were also prepared on flat α-alumina disk supports using the same nanosheet deposition and hydrothermal treatment conditions. TEM images were collected by a FEI Tecnai 30 at an acceleration voltage of 300 kV. Before permeation measurements, the membranes were degassed in the membrane module at 298 K under argon (Ar) gas flow for 8 h. Single-component permeation measurements were carried out using a membrane module constructed in-house, operated in dead-end mode. The pressure rise on the (initially evacuated) permeate side was recorded versus time and used to calculate permeance and ideal selectivity (defined as the ratio of single-component permeances). Binary gas permeation measurements were obtained in Wicke-Kallenbach mode at the specified temperature. An equimolar butane isomers mixture (50 mL/min) was supplied to the feed side (shell side) of the hollow fiber membrane, while Ar (30 mL/min) was used as a sweep gas at the permeate side (bore side). Both feed and permeate were maintained at atmospheric pressure. The permeate was analyzed by an online gas chromatography unit (GC2014, Shimadzu) to obtain the compositions and fluxes of the

two isomers. This data was used to calculate the permeances of each component (i.e., the flux divided by the partial pressure driving force across the membrane) and the separation factor (i.e., the ratio of the mole fractions of the more permeable gas and the less permeable gas in the permeate divided by the same ratio of mole fractions in the feed). The same permeation procedures were used to test the separation properties of *n*-butane/methane and propane/methane mixtures at the desired feed compositions, while Ar (60 mL/min) was used as a sweep gas.

2.3 Results and Discussion

2.3.1 Characterizations of 2D MFI Nanosheet Layer

The methods for preparation and characterization of α-alumina hollow fibers [66, 67] and high-aspect-ratio 2D MFI nanosheets were adapted from previous works [29] and are described in the **2.2 Experimental Methods**. The bottom-up synthesis results in MFI nanosheets (**Figure 2.1**) of large lateral dimension (~2 μm) and much smaller thickness (~5 nm), with straight pore channels of 0.56 nm×0.54 nm running through the sheet in the [010] crystallographic direction. XRD confirms the synthesis of an MFI-type material.

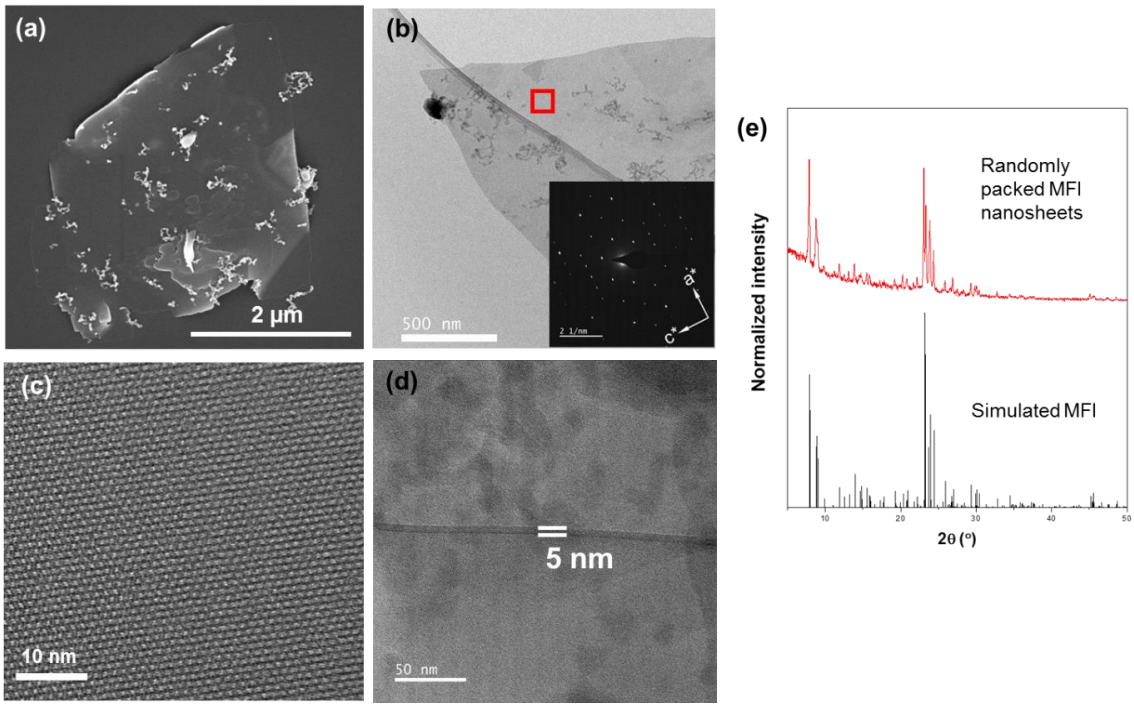

Figure 2.1 (a) SEM image of individual MFI nanosheet. Small amounts of aggregated amorphous particles are also typically seen. (b) TEM image showing top view of a single MFI nanosheet (ac plane), along with and electron diffraction patterns (inset) from the red-outlined area. (c) HRTEM image of the nanosheet showing the MFI pore channels in the (b-direction). (d) TEM image of the edge of a single nanosheet measuring approximately 5 nm in thickness. (e) Powder XRD pattern of the randomly packed MFI nanosheets and comparison with the simulated MFI powder pattern.

Figure 2.2(a) shows a section of the bare α-alumina hollow fiber. After application of vacuum filtration (**Figure 2.3** shows the schematic) with a 0.01 wt% nanosheet suspension for 30 s, a continuous coating of 2D MFI nanosheets is obtained on the outer surface of the hollow fiber (**Figure 2.2(b)-(c)**). The thickness of the coating is <500 nm, and no defects (such as cracks, delaminated areas, or uncovered areas) were found. The lamellar stacking of the nanosheets can be clearly observed from magnified SEM cross-section images (**Figure 2.4**). The XRD pattern of the coating (**Figure 2.2(d)**) has one prominent diffraction peak at ~8.8° 2θ, which corresponds to (020) out-of-plane orientation [20]. This orientation is advantageous for fast diffusion of molecules through the straight

pore channels that are oriented perpendicular to the plane of the membrane. The single-gas permeance of *n*-butane at room temperature decreases sharply from ~186,000 GPU (bare fiber) to ~79,000 GPU after nanosheet coating from the 0.01 wt% suspension, and is further reduced to ~57,000 GPU after coating from a more concentrated 0.02 wt% suspension, thus indicating that the coating thickness is adjustable by varying the MFI nanosheet concentration in the suspension (**Figure 2.5**)

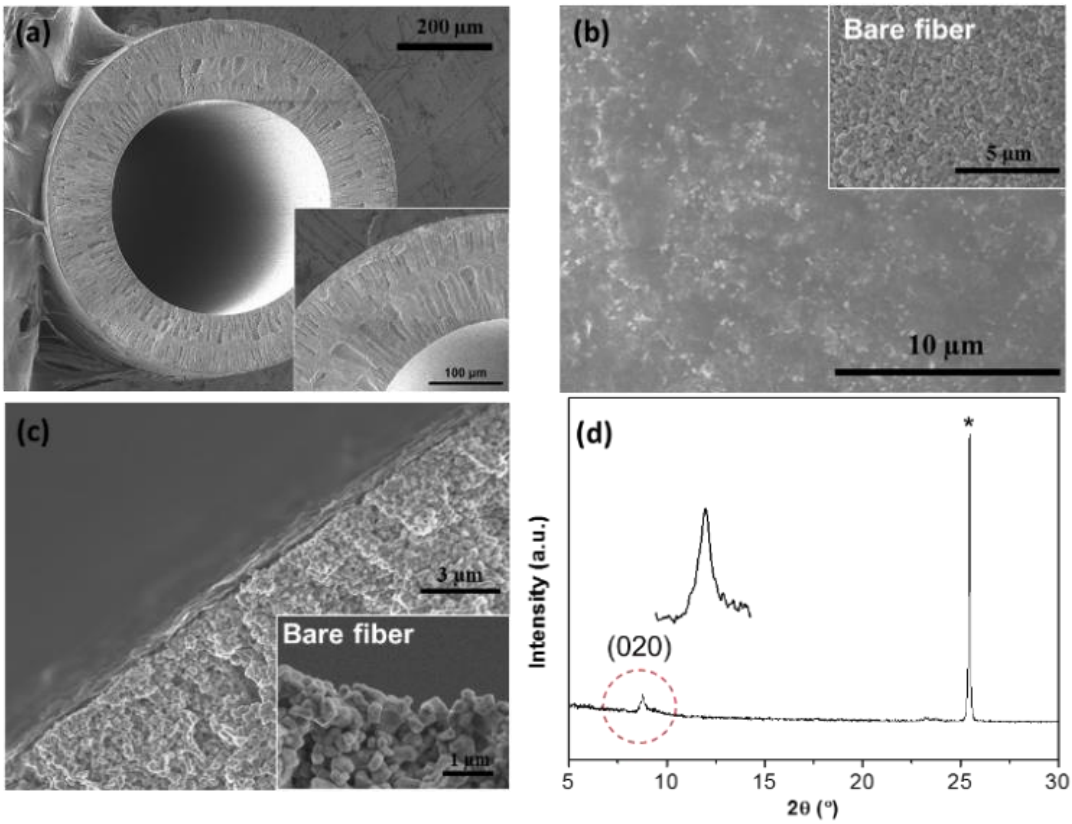

Figure 2.2 (a) SEM image of an α-alumina hollow fiber with (inset) an enlarged cross-section; (b) top-view and (c) cross-sectional images of the MFI nanosheet coating on the hollow fiber along with (inset) the bare fiber morphology; (d) XRD pattern of the nanosheets coating showing (0*k*0) out-of-plane orientation. The asterisk (*) indicates the peak from the α-alumina support.

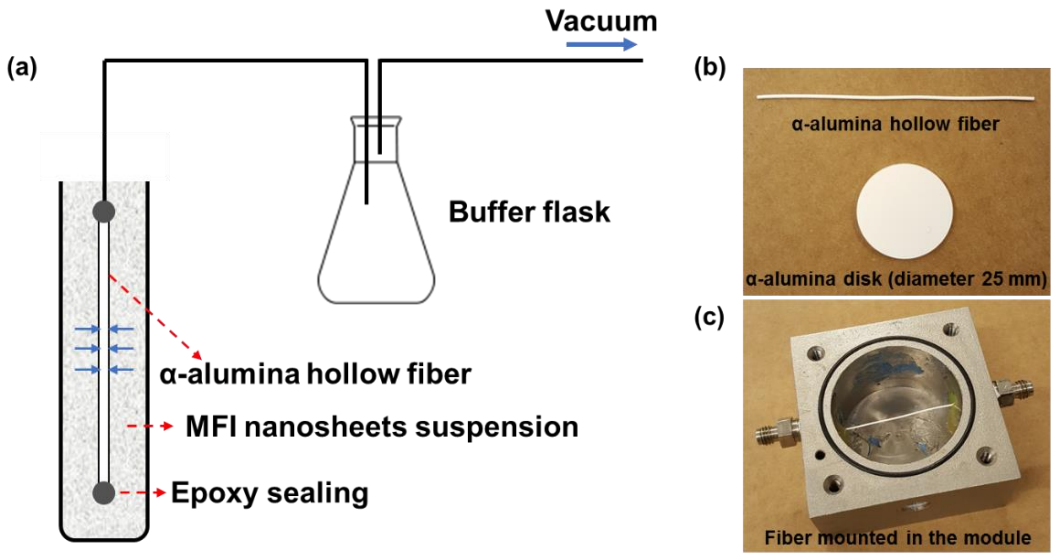

Figure 2.3 (a) Schematic diagram of the vacuum filtration setup; (b) photograph of a hollow fiber and a disk-type support; (c) hollow fiber membrane mounted in a module for permeation measurements.

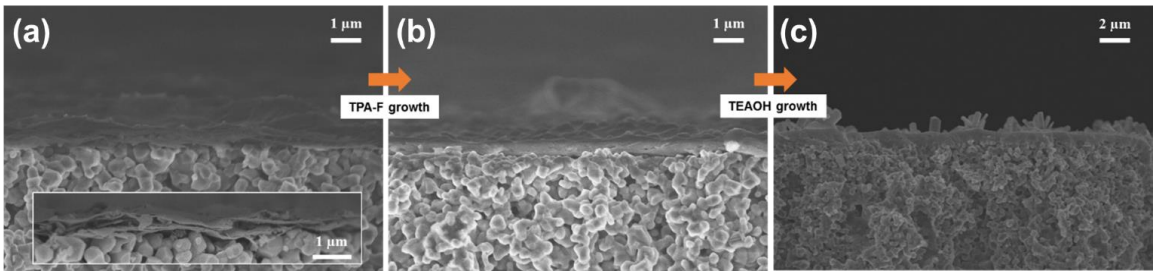

Figure 2.4 (a) Cross-sectional image of the nanosheet coating; (b) (TPA-F) secondary growth membrane; (c) and (TEAOH) tertiary growth membrane.

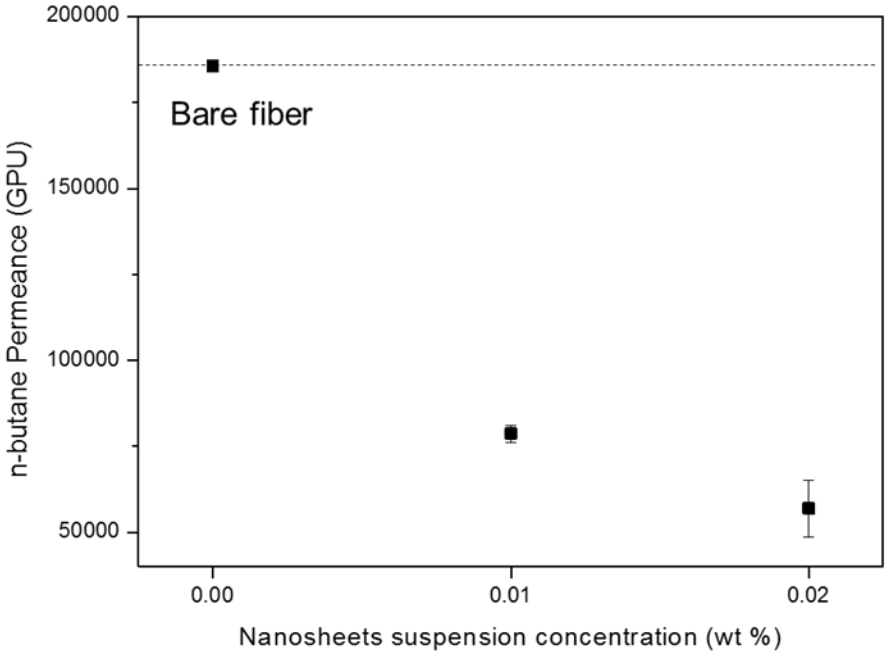

Figure 2.5 Room temperature *n*-butane single gas permeance (dead-end mode) of the bare hollow fiber and the nanosheet coatings at two different concentrations of the suspension. No ideal selectivity for *n*-butane/*i*-butane is observed. 1 gas permeation unit (GPU) = 3.348×10^{-10} mol.m^{-2}.s^{-1}.Pa^{-1}.

2.3.2 Gap Sealing via Sequential Hydrothermal Growth

Although the 2D MFI nanosheet coating is uniform and continuous, it has no butane isomers separation capability because of the large void spaces between the stacked nanosheets where gas molecules can freely diffuse regardless of their kinetic diameter. Further treatments must be applied to the coating to render it capable of molecular sieving. In recent works [35, 36, 65], it has been shown that the void spaces can be effectively closed by growth of MFI domains, driven by supply of silicate reactants from an underlying Stöber silica-derived disk support. Towards the goal of a more easily applicable fabrication process, I describe a two-step hydrothermal method. It is seen that conventional

hydrothermal treatments with tetrapropylammonium or tetraethylammonium hydroxide (TPAOH or TEAOH) are not successful (**Figure 2.6**). In the case of TPAOH, the MFI nanosheet coating quickly loses its (0*k*0) orientation due to abundant twinning and secondary nucleation (**Figure 2.6(a)** and **Figure 2.9**), as has also been shown for MFI membranes grown from (0*k*0)-oriented exfoliated nanosheets [46, 68] and seed particles [20]. This surface roughening can be explained by the mechanism of the MFI growth in TPAOH conditions, in which aggregated precursor nanoparticles evolve into MFI particles [68, 69]. This could be potentially avoided by the use of TEAOH, which is known to delay nucleation and suppress surface roughening [68, 70]. Moreover, the in-plane growth rate is known to be considerably faster than the out-of-plane growth rate, thus promoting the formation of highly intergrown thin films. Indeed, after TEAOH-based hydrothermal growth, the 2D MFI nanosheets were seemingly laterally well-intergrown (**Figure 2.6(b)-(c)**), but with some mis-oriented crystals. However, the membranes were prone to extensive cracks and delamination from the alumina fiber support surface (**Figure 2.6(d)**), which can be attributed to insufficient adhesion of the MFI film to the alumina support as a result of slow out-of-plane growth.

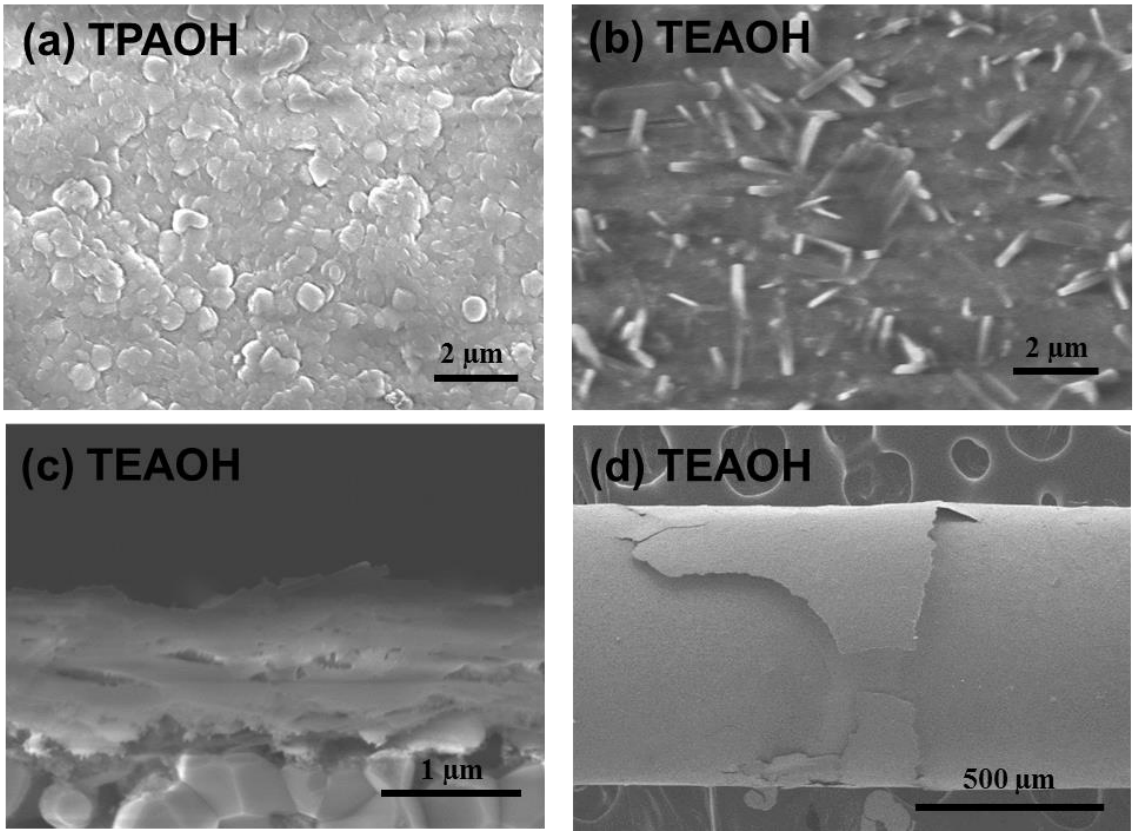

Figure 2.6 Top-view SEM images of MFI nanosheet-based membranes treated hydrothermal with silicate solutions that contain the structure-directing agents (a) TPAOH and (b) TEAOH; (c) Cross-sectional SEM image of the membrane from (b); and (d) Top-view low-magnification SEM image of the membrane from (b) showing extensive delamination and crack formation. The TEAOH secondary growth membranes showed *n*-butane permeances of 44000 – 59000 GPU even before SDA removal (and no isomer selectivity), confirming the SEM observation of membrane delamination.

Therefore, I adopted hydrothermal treatment in a tetrapropylammonium fluoride (TPAF) medium. Fluoride-medium synthesis generally yields MFI crystals with smooth and large grains [71]. Furthermore, addition of fluoride ions is known to alter the relative rates of in-plane and out-of-plane growth [72]. The MFI nanosheet-coated hollow fibers were immersed in a sol with a molar composition of 1 SiO_2: 0.02 Na_2O : 0.12 TPAOH: 0.12 HF: 60 H_2O and subjected to the hydrothermal growth at 373 K. The influence of treatment duration on the microstructure was explored (**Figure 2.7**). It is evident from SEM

observation that all treatments carried out between 6 h - 48 h are able to fill in the voids of the 2D MFI nanosheet coating. However, the longer durations lead to considerable overgrowth of a polycrystalline MFI layer on the nanosheet membrane. The overgrowth layer does not preserve the (0*k*0) out-of-plane orientation of the membrane. The shorter treatment durations of 12 h and 6 h appear to selectively fill the voids without significant overgrowth and also without delamination or crack formation.

The microstructure of the membrane after 12 h hydrothermal treatment was examined in more detail. SEM images **Figure 2.8(a)-(b)** confirm the selective filling of voids between the 2D MFI nanosheets and the suppression of overgrowth. The membrane thickness was preserved as ~500 nm. The XRD pattern (**Figure 2.8(c)**) confirmed intense peaks from (0*k*0) reflections, which indicates that the out-of-plane orientation is preserved and only a small number of (*h*0*l*)-oriented grains are present [20, 23]. The integrated peak intensity ratio (I(101)/I(020)) is 0.11, which is much lower than the corresponding values of 0.52 for a membrane grown in TPAOH medium and 1.42 for a randomly oriented calcined MFI powder (**Figure 2.9**). Also, the enlarged inset shows the distinct (040) peak and absence of the (400) peak, demonstrating that the (*h*00) orientation is not yet seen in the membrane.

The above results strongly suggest that TPAF-based hydrothermal treatment is effective for selective void sealing between 2D MFI nanosheets while maintaining a desirable out-of-plane orientation and good adhesion with the alumina support surface, without need for specially engineered support surfaces. However, we still cannot rule out the presence of the non-selective nanoscopic gaps. Indeed, SEM images shown in **Figure 2.10** indicate the presence of nanoscale intergrain gaps. To selectively close the nanoscopic

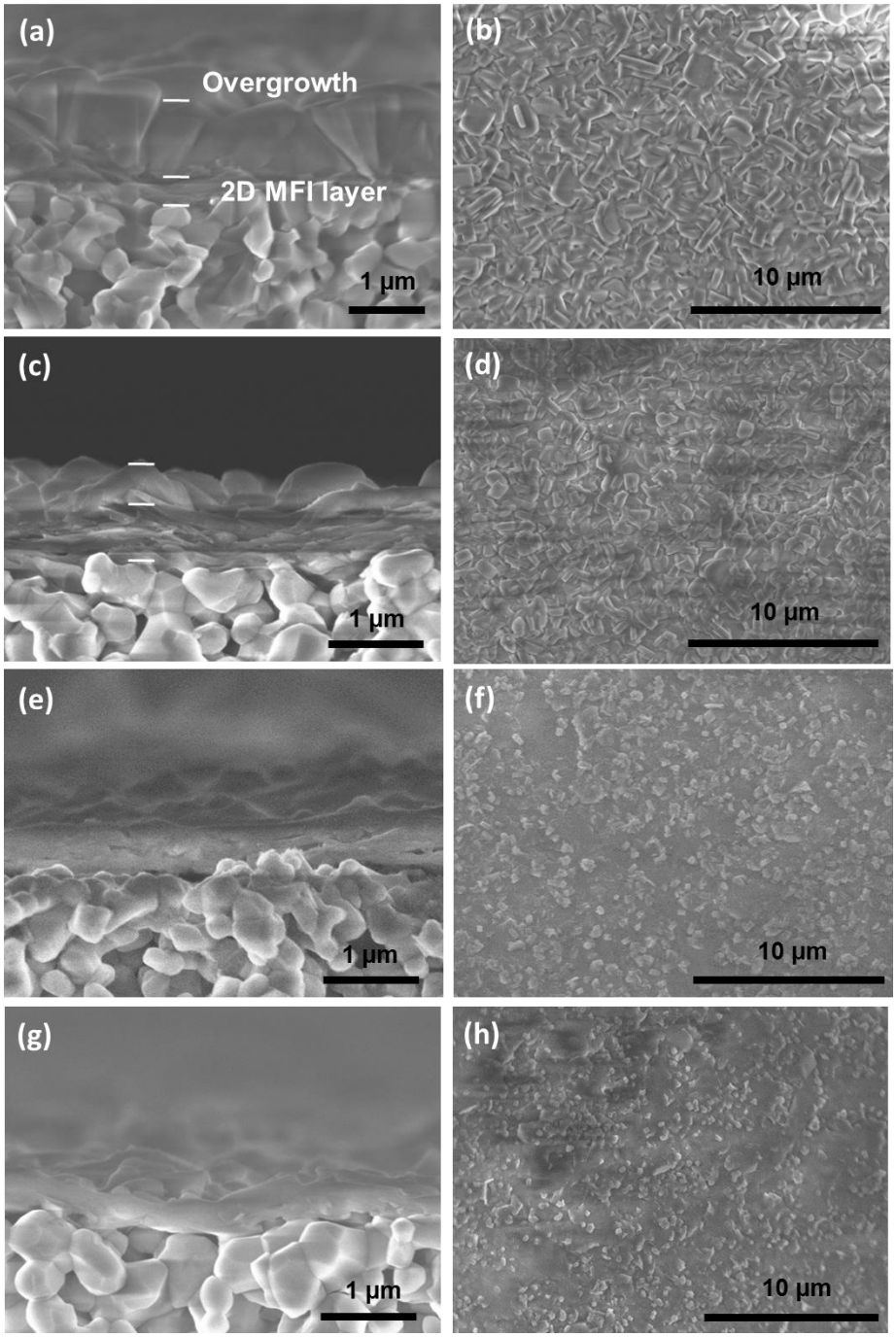

Figure 2.7 Top-view and cross-sectional SEM images of membranes treated with TPAF-containing sols for (a-b) 48 h; (c-d) 24 h; (e-f) 12 h; and (g-h) 6 h.

small gaps while continuing to preserve the orientation, the membrane was subjected to a second hydrothermal treatment with a TEAOH-containing silica sol. This treatment was carried out at 443 K for 48 h with a silica precursor solution of composition 1 SiO_2: 0.30

TEAOH: 100 H_2O. Representative SEM top-view and side-view images (**Figure 2.8(d)-(e)**) show that the membrane surface texture was preserved, although a few mis-oriented outgrowths can be occasionally observed. After this "tertiary growth" step, the membrane was significantly more well-intergrown and nanoscale gaps were eliminated as seen in the cross-section view. The membrane thickness somewhat increased to <800 nm after tertiary growth. Since the preceding TPAF secondary growth already produces an intergrown and mechanically stable membrane layer, the role of the TEAOH tertiary growth is now restricted to final closure of defects. Therefore, the membrane shows excellent adhesion to the alumina hollow fiber support after TEAOH tertiary growth, in contrast with direct TEAOH secondary growth which, as mentioned earlier, led to membrane delamination. The XRD pattern (**Figure 2.8(f)**) shows the dominant peak from the (020) reflection along with the enlarged inset showing the (040) reflection, confirming that the out-of-plane orientation of the membrane is successfully preserved. The $I(101)/I(020)$ ratio is now 0.25, which is still much lower than for the TPAOH medium. The slight increase over the secondary growth value is likely due to the occasional mis-oriented surface intergrowths (**Figure 2.8(d)-(e)**).

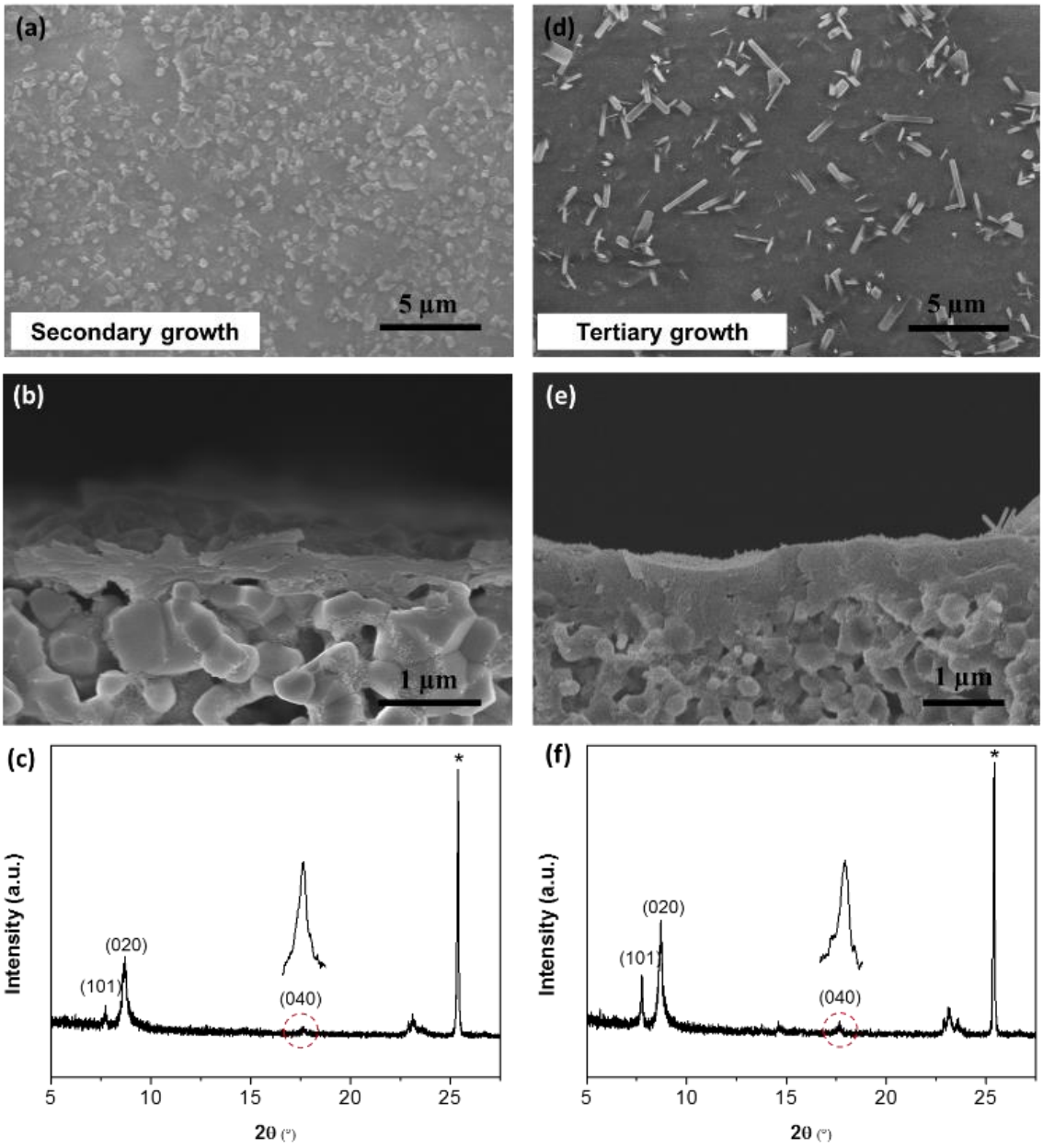

Figure 2.8 Top-view and cross-sectional SEM images, and XRD patterns of MFI membrane: (a-c) after 12 h secondary treatment in fluoride medium; (d-f) MFI membrane after additional tertiary treatment in TEAOH medium. Asterisks (*) in the XRD patterns indicate diffraction peaks of the α-alumina support.

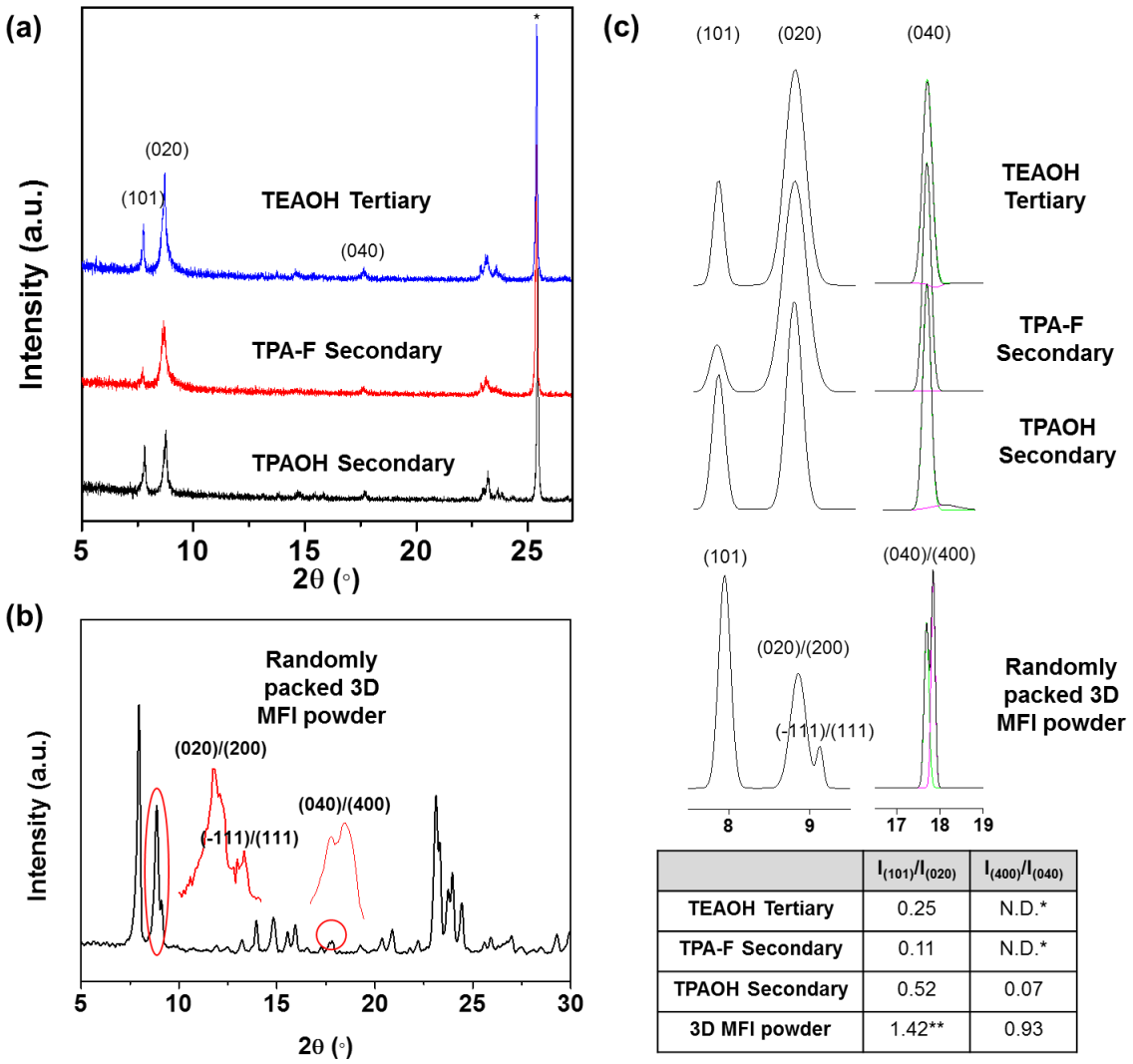

	$I_{(101)}/I_{(020)}$	$I_{(400)}/I_{(040)}$
TEAOH Tertiary	0.25	N.D.*
TPA-F Secondary	0.11	N.D.*
TPAOH Secondary	0.52	0.07
3D MFI powder	1.42**	0.93

*Not Determined
**$I_{(101)}/I_{((020)+(200))}$

Figure 2.9 (a) XRD patterns of hollow fiber membranes formed after secondary growth of MFI nanosheet coatings in TPA-OH and TPA-F media, and after tertiary growth of the TPA-F secondary-grown membrane in TEA-OH medium. Asterisk (*) indicates the peak from the α-alumina hollow fiber support. (b) XRD pattern of randomly packed 3D MFI powder (c) Deconvolution and the peak fitting of the (101), (020)/(200) and (040)/(400) peaks; and the integrated peak intensity ratio of I(101)/I(020) and I(400)/I(040) for each case (The peak fitting was not able to resolve the (020) and (200) peaks separately). Deconvolution of the dominant (040) peak showed negligible (400) peak for the TPA-F secondary growth membrane and TEAOH tertiary growth membrane (I(400)/I(040): Not Determined), while XRD peaks from randomly packed 3D MFI powder showed clearly resolved (040) and (400) peaks.

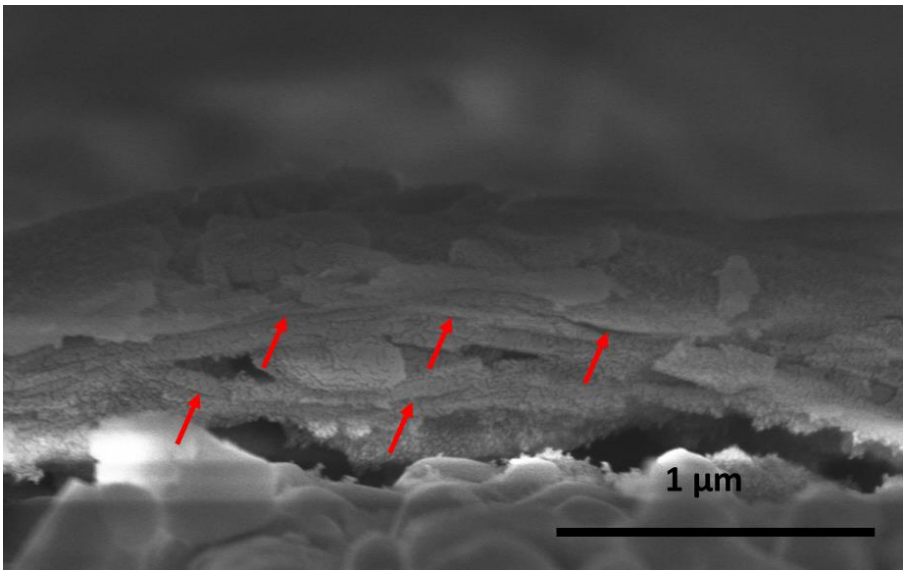

Figure 2.10 Cross-sectional SEM image of hydrothermally treated (with TPAF) membrane. The arrows show the presence of nanoscale gaps (dark areas between the nanosheets) that lower the separation selectivity.

2.3.3 Gas Permeation Properties of 2D MFI Membranes

Next, I examined the relationship of the membrane microstructures after each treatment with their separation properties. The membrane molecular sieving properties after TPAF treatment ("secondary growth") and TEAOH treatment ("tertiary growth") were evaluated by the separation of butane isomers. Equimolar *n*-butane/*i*-butane gas mixture separation performance was measured at 298 K using nine independently fabricated hollow fiber membranes, three of which were measured after the secondary treatment step and the remaining six were measured after both secondary and tertiary treatment steps. Measurements were also made with the initial 2D MFI nanosheet coatings as a baseline. **Figure 2.11** shows the data from individual membrane samples as well as the averages from the samples at each of the three stages of processing, and **Table 2.1** lists all the numerical values. While the initial nanosheet coatings show very high permeances

and no selectivity, clear and progressive molecular sieving effects are observed for all the secondary and tertiary-treated membranes. The secondary treatment leads to a large decrease in *n*-butane permeance relative to the nanosheet coating and a significant increase in separation factor to ~10. Tertiary treatment results in a large increase in separation factor to > 40 and a moderate decrease in *n*-butane permeance. These findings are fully consistent with the main microstructural events occurring during secondary treatment (filling of bulk voids between the nanosheets but incomplete closure of nanoscopic gaps) and tertiary treatment (filling of nanoscale gaps and some increase in membrane thickness). After tertiary treatment the MFI membranes exhibit excellent *n*-butane permeance of 382±100 GPU and a high *n*-butane/*i*-butane mixture separation factor of 42±4 at 298 K. Based upon the kinetic diameters of *n*-butane (0.43 nm) and *i*-butane (0.53 nm) as well as preferential adsorption of *n*-butane at lower pressures, MFI membranes are known to be selective for *n*-butane [21, 73]. At the present experimental conditions, the results are consistent with the analysis performed in previous works [73] and arise from competitive adsorption-diffusion phenomena. For consistency, permeation data from all membranes are reported after 1.5 h of post-degassing measurement, at which the permeance and separation factor reach a nominal steady state (**Figure 2.12**).

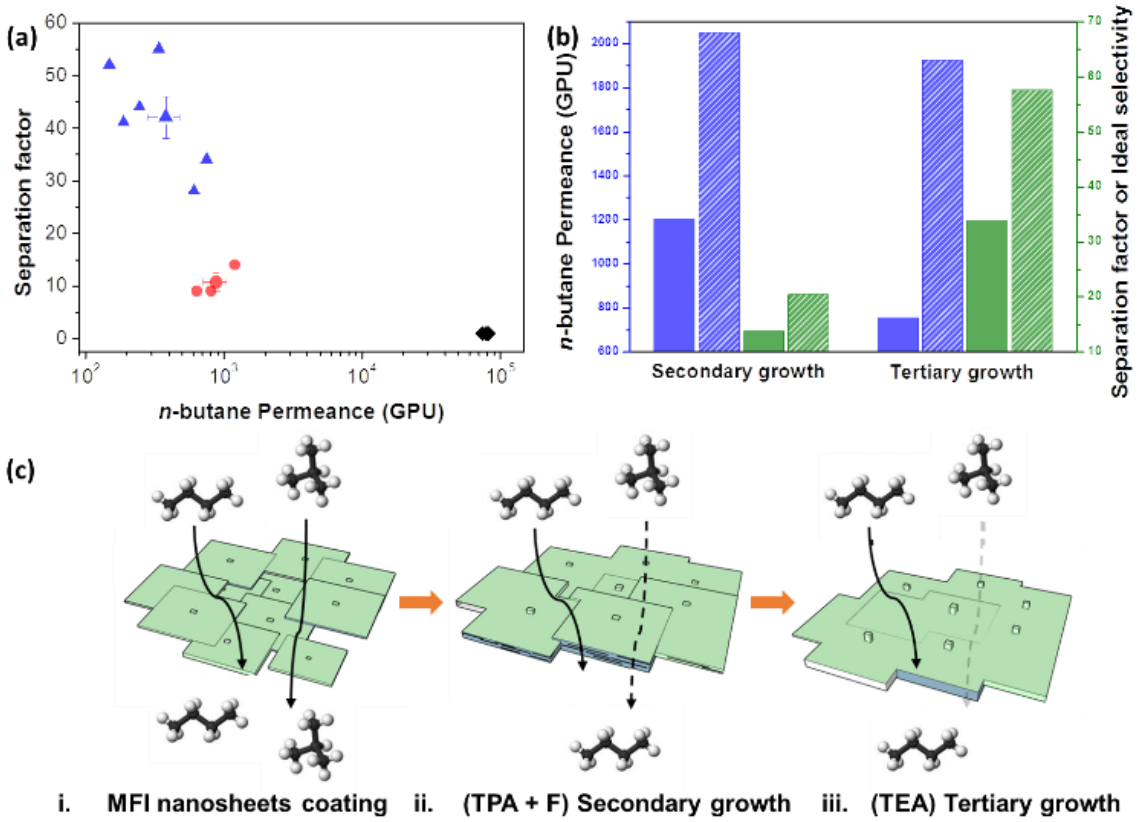

Figure 2.11 (a) Equimolar *n*-butane/*i*-butane mixture separation performance of MFI membranes at 298 K after each processing step: (I) MFI nanosheets (black diamonds), (II) TPA-F secondary treatment (red circles) and (III) TEAOH tertiary growth (blue triangles). Values from individual membrane samples as well as averaged values are shown in each case; (b) Comparison of single-component and binary butane isomers permeation after secondary (ST-1 from **Table 2.1**) and tertiary treatment (TT-1 from **Table 2.1**) at 298 K: binary *n*-butane permeance (solid blue bars), single-component *n*-butane permeance (hatched blue bars), binary separation factor (solid green bars), single-component selectivity (hatched green bars); (c) Schematic illustration of membrane microstructure evolution during the three steps.

Table 2.1 Butane isomers separation results measured from a *n*-/*i*-butane binary feed mixture at 298 K. 1 gas permeation unit (GPU) = 3.348×10^{-10} mol.m^{-2}.s^{-1}.Pa^{-1}. Three NS coatings, three ST membranes and six TT membranes were prepared and measured independently. Note: the NS, ST, and TT coating/membrane sets shown here are entirely independent samples since a coating or membrane, once mounted in the module for permeation measurements, cannot be removed and used to perform further growth steps.

Membrane sample	**Permeance [GPU]**		***n*-butane/*i*-butane Separation factor**
	***n*-butane**	***i*-butane**	
Nanosheets coating layer (NS)-1*	74000	74400	1
NS-2	80200	80400	1
NS-3	81700	81100	1
Average	78600 ± 2400	78600 ± 2100	1 ± 0
Secondary treatment (ST)-1	1201	77	14
ST-2	639	65	9
ST-3	811	80	9
Average	884 ± 166	74 ± 4	11 ± 2
Tertiary treatment (TT)-1	754	20	34
TT-2	189	6	41
TT-3	611	20	28
TT-4	340	6	55
TT-5	149	3	52
TT-6	247	5	44
Average	382 ± 100	10 ± 3	42 ± 4

* Nanosheets coating obtained from the 0.01 wt% coating suspension

However, it is known that longer measurements show a slow decrease in permeance with time [74-76], which has been attributed to small concentrations of impurity hydrocarbons in the butane feed that result in a much longer time requirement to approach a true steady-state. I therefore operated one membrane for up to 60 h on-stream (**Figure 2.12**), and also observed a slow decrease of the permeances of both *n*-butane and *i*-butane

(15% and 36%). The separation factor increased by about 35% to more than 75 while still maintaining a high *n*-butane permeance of 288 GPU.

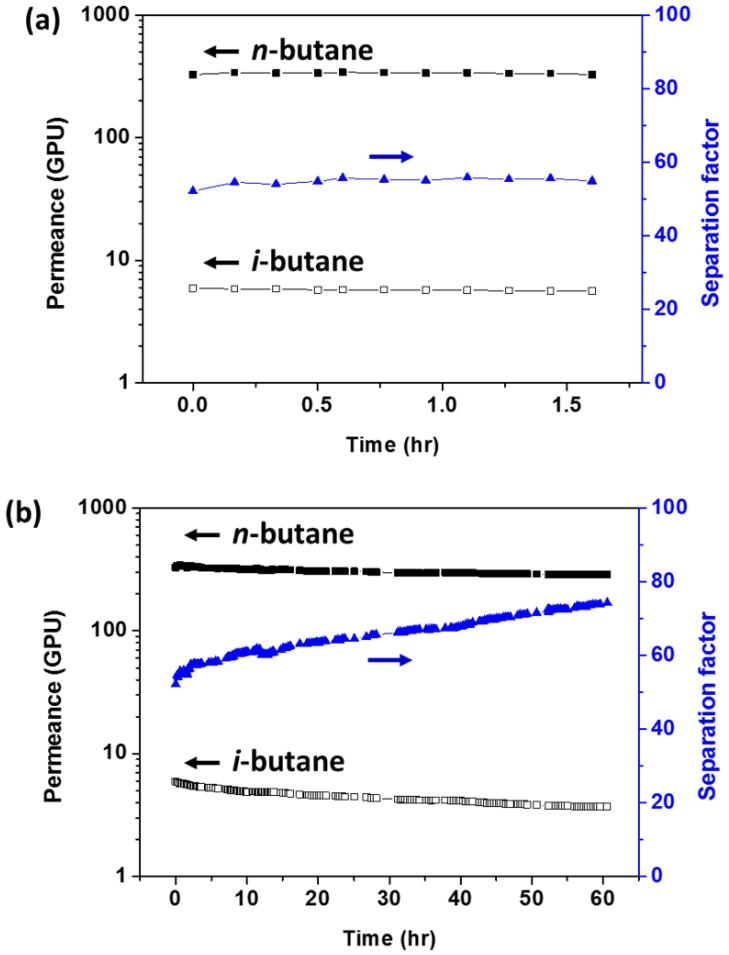

Figure 2.12 On-stream *n*-butane/*i*-butane separation performance of a single tertiary growth membrane (TT-4 from **Table 2.1**): (a) measurement up to 1.5 h, and (b) long-term operation up to 60 h.

Although mixture permeation data allow evaluation of the actual separation characteristics, they are affected by competitive adsorption and diffusion. Unary (single-component) data provide a cleaner characterization of the microstructural quality. **Figure 2.11(b)** compares binary and unary permeation data after secondary and tertiary treatments. In both cases, the unary *n*-butane permeances and selectivities are considerably higher than the corresponding binary permeances and separation factors. In binary permeation, *i*-

butane competes to a certain extent with *n*-butane in the straight (0*k*0) channels of MFI, reducing the *n*-butane permeance and selectivity [73, 75]. In unary permeation the membrane (particularly after tertiary treatment) shows very high *n*-butane selectivity and permeance. This clearly indicates the excellent microstructural quality of the membrane. Further, the difference between binary and unary cases is much more pronounced after tertiary treatment than after secondary treatment alone. After secondary treatment some permeation still occurs through non-selective nanoscopic defects. After tertiary treatment, practically all permeation is through the MFI pores wherein competitive effects are rather strong. **Table 2.2** compares the results of the present work with previous reports of MFI membranes (made by conventional polycrystalline film growth as well as with 2D MFI nanosheets) and other membrane types (polymeric, mixed matrix, ZIF). The present work is the first to report highly (0*k*0)-oriented MFI membranes on hollow fibers, that furthermore have excellent characteristics for butane isomers separation. In relation to MFI membranes prepared using Stöber silica-derived disk supports that show a separation factor of about 58 (average from **Table 2.2**), the present membranes have quite comparable separation factors (ca. 42 after 1.5 h and ca. 75 after 60 h). An exact comparison of separation factors between two selective membrane types may have only limited value, but possible reasons for the difference include the hydrothermal growth mechanisms (for example, delivery of silica reactants from support versus from liquid phase as well as the SDAs), different microstructures after calcination of curved (fiber) versus flat (disk) membranes [77], and different measurement times. Finally, I obtained preliminary data on the removal of natural gas liquid (NGL) components such as *n*-butane and propane from methane, currently carried out by cryogenic distillation [7]. In binary permeation

measurements over a realistic range of *n*-butane contents in methane (**Figure 2.13(a)**), MFI membranes exhibit exceptionally high permeance (2000-3000 GPU) and *n*-butane separation factor (35-300). For propane (**Figure 2.13(b)**), permeances of 5000-10000 GPU and separation factors of 10-45 are seen. Selective permeation of higher hydrocarbons from mixtures with methane is due to their strong adsorption selectivity in MFI, as confirmed by unary data (**Figure 2.13(c)**) wherein methane permeates much faster than *n*-butane and propane.

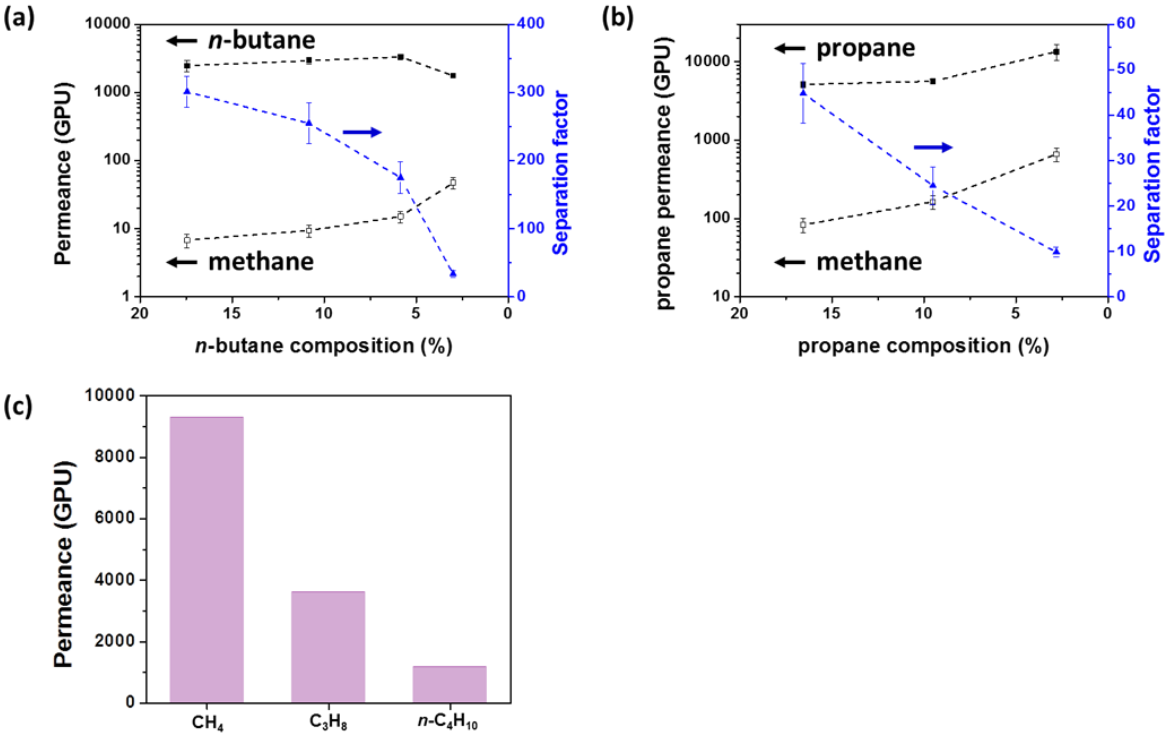

Figure 2.13 Separation performance of MFI membranes for hydrocarbon separations. Data and error bars are based upon averaging of membrane samples TT-4, 5 and 6 (**Table 2.1**). (a) *n*-butane/methane binary separation performance as a function of *n*-butane content in the methane stream; (b) propane/methane binary separation performance as a function of propane content in the methane stream; (c) single-component permeation data for each component in one membrane sample (TT-4).

Table 2.2 Reported butane gas permeation characteristics of MFI membranes grown on disks or tubes and other types of membranes; and comparison to data from hollow fiber membranes in this work. 1 gas permeation unit (GPU) = 3.348×10^{-10} $mol.m^{-2}.s^{-1}.Pa^{-1}$. * Denotes single-component measurement data.

Supp. Ref. No. **	Seed type	Out-of-plane Orientation	Thickness (μm)	Support type	Temperature (K)	*n*-butane permeance [GPU]	*n*-butane/*i*-butane Separation Factor or Ideal selectivity*
[78]	-	random	~ 7	α-alumina disk	298	90	52
[79]	-	random	> 100	Stainless steel tube	298	6	5
[79]	-	random	> 100	Stainless steel tube	298	105	5
[80]	Plate-like	(*h*00)	7.5	Silica-coated α-alumina disk	298	299	18
[80]	Randomly oriented	random	15	Silica-coated α-alumina disk	298	239	46
[37]	Randomly oriented	(00*l*)	8	α-alumina disk	298	299	35
[81]	-	random	50	unsupported	298	239	48
[82]	-	-	35	TiO_2-coated stainless steel disk	303	149	55
[83]	-	random	0.5	Asymmetric α-alumina disc	298	2927	9
[84]	Randomly oriented	(00*l*)	30	Silica-coated α-alumina disk	295	179	62
[85]	Randomly oriented	(00*l*)	15	α-alumina disk	295	60	71
[85]	Randomly oriented	(00*l*)	30	α-alumina disk	295	90	40
[86]	-	random	5	α-alumina disk	298	90	52
[87]	-	-	30-50	Stainless steel disk	303	149	25
[88]	-	-	15	TiO_2 coated stainless steel disk	303	418	45
[89]	-	-	30	TiO_2 coated stainless steel disk	303	209	28

Table 2.2 continued

[23]	b-oriented MFI plate	(0*k*0)	1	Silica-coated α-alumina disk	323	538	5
[41]	-	(0*k*0)	2-3	Silica-coated α-alumina disk	298	6*	3*
[35]	Exfoliated nanosheets	(0*k*0)	0.1-0.25	Stöber silica - coated sintered silica fiber disk	298	1284	62
[35]	Exfoliated nanosheets	(0*k*0)	0.1-0.25	Stöber silica - coated sintered silica fiber disk	298	699	47
[29]	Directly synthesized nanosheets	(0*k*0)	0.25-1	Stöber silica - coated sintered silica fiber disk	298	597	50
[65]	Directly synthesized nanosheets	(0*k*0)	0.5 -1.5	Stöber silica - coated sintered silica fiber disk	295	290	64
[65]	Directly synthesized nanosheets	(0*k*0)	0.5-1.5	Stöber silica - coated sintered silica fiber disk	295	986	69
[73]	Randomly oriented seed	(*h*0*l*)	8	α-alumina tube	333	714	27
[90]	6FDA-DAM polymer	-	30	unsupported	373	37 ± 2*	21 ± 2*
	MFI (35 wt%)-6FDA-DAM mixed matrix	-	30	unsupported	373	78 ± 2*	23 ± 2*
[91]	ZIF-90	-	3.1	Carbon hollow fiber	298	60	12
This work (secondary treatment)	**Directly synthesized nanosheets**	**(0*k*0)**	**0.5**	**α-alumina hollow fiber**	**298**	**884 ± 166**	**11 ± 2**
					298	**2047***	**20***
This work (tertiary treatment)	**Directly synthesized nanosheets**	**(0*k*0)**	**0.8**	**α-alumina hollow fiber**	**298**	**382 ± 100**	**42 ± 4**
					298	**1923***	**58***

2.4 Conclusion

In conclusion, I have exploited the use of 2D MFI nanosheet coatings to obtain thin, high-flux, highly selective membranes on a simple macroporous hollow fiber support without the need for highly engineered supports or the use of silica disk supports to provide membrane growth reactants. Vacuum filtration allows preparation of uniform 2D MFI nanosheet coatings on α-alumina hollow fibers. Sequential secondary and tertiary hydrothermal treatments with selected fluoride and tetraethylammonium-containing solutions are effective in closing macroscopic voids and nanoscopic defects respectively, while maintaining desired (0*k*0) out-of-plane orientation and adhesion with the alumina fiber. These results have significant implications for utilizing zeolite nanosheets to accelerate scale-up and applications of thin and selective membranes.

CHAPTER 3. MULTICOMPONENT HYDROCARBON MIXTURE SEPARATION PROPERTIES OF 2D MFI HOLLOW FIBER MEMBRANES: EXPERIMENTAL AND MODELING INVESTIGATION

3.1 Introduction

Natural gas from shale resources is steadily replacing coal for power generation [92], and its demand is expected to grow substantially through 2040 [93]. Shale gas is a multicomponent mixture containing methane (CH_4) as a major constituent (75-90%), a substantial amount of higher hydrocarbons such as ethane (C_2H_6), propane (C_3H_8), butanes (C_4H_{10}), and small quantities of higher hydrocarbons, CO_2, N_2, H_2S, and He [94]. Shale gas is usually classified as 'dry' or 'wet' gas according to the proportion of heavier hydrocarbons (C_{2+}) [7]. 'Wet' gas contains considerable amounts of C_{2+} hydrocarbons and less than 85 % of CH_4 [95] (**Table 3.1**). Therefore, a number of separation steps are necessary to remove contaminants (water, acid gases such as CO_2 and H_2S, and mercury) as well as the large quantities of C_{2+} hydrocarbons. The latter separation step is of high importance for several reasons, including (i) increasing the CH_4 content and fuel value, (ii) meeting the pipeline quality standards (950-1050 Btu/scf, dew point < 253 K), (iii) eliminating condensate formation [96], and (iv) valorizing the separated C_{2+} hydrocarbons as chemical feedstocks [25].

Conventionally, C_{2+} hydrocarbon recovery is performed by cryogenic distillation. Natural gas is expanded and then fractionated by a series of distillation columns

(demethanizer, deethanizer, depropanizer, and debutanizer) [97]. These processes are highly energy-intensive, thus creating a very large potential market for energy-efficient and compact membrane separation technology for the removal of higher hydrocarbons from natural gas [98]. Conventional glassy and crystalline polymer membranes for gas separations are not suitable since they selectively permeate methane, whereas it is desired to permeate and remove the minority C_{2+} components through the membrane. Elastomeric and microporous polymer membranes have some selectivity for heavier hydrocarbons due to stronger adsorption, and hence membranes of poly(dimethylsiloxane) (PDMS) [99], PIM-1 [100], and poly(trimethyl-silyl-propyne) (PTMSP) [101] have been studied. Although such membranes can be made at low cost, their permeability, selectivity, and low plasticization resistance [102] limit the potential for industrial applications.

Table 3.1 Composition of shale gas in different locations (adapted from [95]). Units are in vol% unless otherwise mentioned.

	USA					
	Bakken	**Marcellus**	**Utica**	**Niobrara**	**Eagle ford**	**San Juan County**
Methane	52.67	76.75	81.21	68.49	66.62	77.3
Ethane	24.6	12.58	12.84	11.21	16.30	11.2
Propane	12.86	5.06	3.72	10.41	8.52	5.8
***n*-butane**	3.78	1.00	0.72	3.68	2.71	2.3
***i*-butane**	1.34	1.08	0.47	1.03	1.14	
N_2	1.62	0.20	0.53	1.77	0.30	1.4
CO_2	0.37	2.42	0.09	1.39	1.99	0.8
H_2S (ppm)	10 – 400	N/A	0.00	N/A	N/A	-
C_{5+}	2.76	2.29	0.43	2.02	2.4	1.2

It has long been suggested that inorganic zeolite membranes offer an attractive route for removing C_{2+} hydrocarbons (also referred to as natural gas liquids, NGLs) because of their much higher flux, high selectivity, and structural robustness [7, 25, 103-105]. It is well-known that MFI-type zeolite membranes possess strong adsorption-based selectivity for higher hydrocarbons, thereby depleting the NGL components and enriching the methane composition in the retentate stream [7, 25, 103-107]. However, zeolite membranes have been limited by the lack of scalable and low-cost fabrication processes that typically involve deposition of nanoparticle seed layers followed by hydrothermal growth into a polycrystalline membrane. These steps create considerable difficulties in fabricating defect-free membranes on a large scale at sufficiently low cost. In recent years, it has been shown that the use of high-aspect-ratio (2D) MFI nanosheet coatings (instead of nanoparticle seed layers) can dramatically increase the quality of MFI membranes for hydrocarbon applications such as separation of xylene isomers or butane isomers [29, 35, 65]. However, the formation mechanism of these membranes still required the use of specially fabricated silica disk supports that are very expensive and not scalable at present. This is an important issue since the support accounts for the majority of the cost of zeolitic membrane fabrication. Recently, I showed that high-quality 2D nanosheet-based MFI membranes could be made on inexpensive α-alumina hollow fibers that are produced by a standard spinning process without any surface engineering or modification steps [76]. These membranes displayed high separation performance for butane isomers. Based upon these encouraging prior findings, and the known adsorption selectivity of MFI for heavier hydrocarbons over methane, the present work is mainly focused on a detailed investigation of the separation of multicomponent (binary, ternary and quaternary) C_1-C_4 hydrocarbon

mixtures by 2D nanosheet-based MFI hollow fiber membranes over a range of mixture compositions and pressures. Our experimental investigation is complemented by detailed modeling of multicomponent permeation in MFI membranes by the Maxwell-Stefan approach.

3.2 Experimental Methods

3.2.1 Permeation Measurements

Unary, Binary, ternary and quaternary gas permeation measurements were obtained in Wicke-Kallenbach mode at 298 K (**Figure 3.1**). A desired feed composition (total feed flow rate was set to 50 mL/min) was supplied to the feed side (shell side) of the hollow fiber membrane with a desired feed pressure, while Ar (10 mL/min for the unary, 60 mL/min for the mixture) was used as a sweep gas at the permeate side (bore side). For all cases, the pressure of the feed gas was adjusted using a back-pressure regulator (Cole Parmer, 0−300 psi range) and permeate were maintained at atmospheric pressure. The permeate was analyzed by an online gas chromatography unit (GC2014, Shimadzu) to obtain the compositions and fluxes of each component. This data was used to calculate the permeances of each component (i.e., the flux divided by the partial pressure driving force across the membrane) and the separation factor (i.e., the ratio of the mole fractions of the more permeable gas and the less permeable gas in the permeate divided by the same ratio of mole fractions in the feed). The 10/90 vol% *n*-butane/methane pre-mixed gas cylinder was purchased from NexAir. Pure *n*-butane, propane, ethane, and methane gas cylinders were purchased from Airgas. The compositions of gas mixtures were adjusted carefully with MFCs (Brooks Instruments) and a mixer before entering the feed side of the

membrane module. Separation of the 10/90 vol% *n*-butane/methane binary mixture pressure range of 1-10 bar. For separation of the 10/90 vol% propane/methane binary mixture, the mixture was fed to the module at a feed pressure range of 1-9 bar. For separation of 9/9/82 vol% ternary mixture of *n*-butane/propane/methane, and the 8/8/8/76 vol% quaternary mixture of *n*-butane/propane/ethane/methane, the feed pressure range was 1-9 bar.

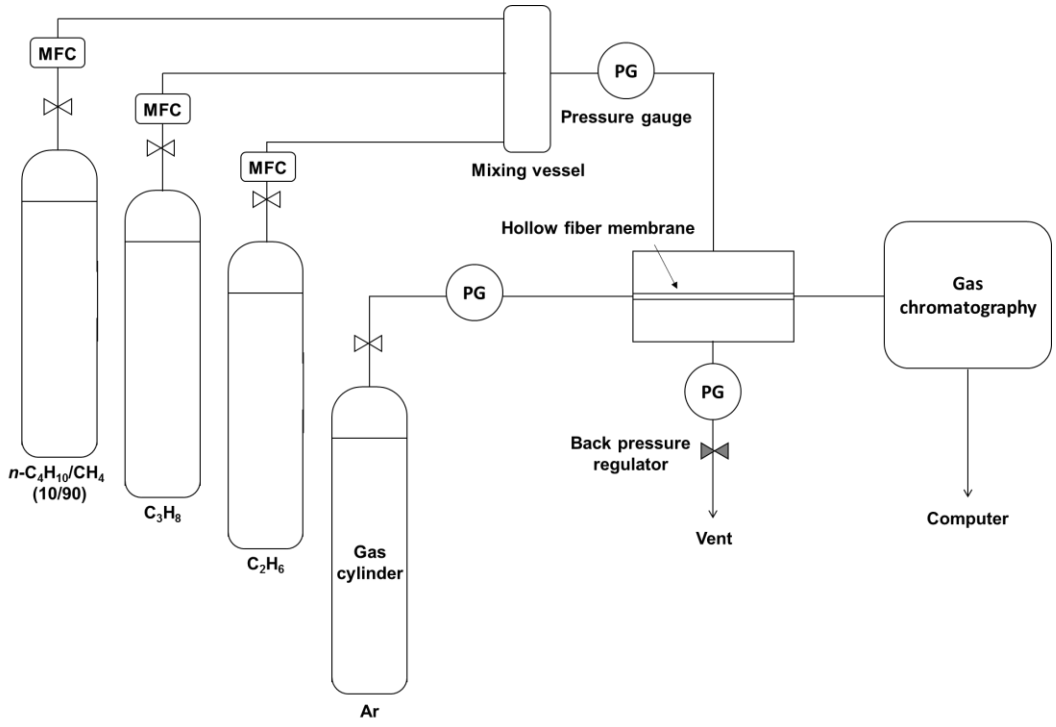

Figure 3.1 Schematic diagram of multicomponent membrane permeation system

3.3 Modeling Methods

3.3.1 Adsorption

The Peng-Robinson equation of state was used for all calculations of component fugacities and for conversion of vol% into mole fractions.

Table 3.2 Dual-site Langmuir parameters for unary adsorption in high-silica MFI zeolite [51].

		Dual-Site Langmuir (DSL) model parameters			
		Site A		**Site B**	
Component *i*	**Temperature/K**	**$K_{i,A}$ (Pa^{-1})**	**$q_{i,A}^{sat}$ ($mol.kg^{-1}$)**	**$K_{i,B}$ (Pa^{-1})**	**$q_{i,B}^{sat}$ ($mol.kg^{-1}$)**
Methane	300	0.00000486	1.9074	0.000000238	1.3872
Ethane	300	0.0000973	2.0808	0.000000438	0.5202
Propane	300	0.000964	1.9074	0.00000506	0.1734
n-Butane	300	0.016	1.5606	0.000011	0.1734

Unary adsorption parameters are obtained by fitting the experimental literature isotherms to the dual-site Langmuir (DSL) isotherm model (Equation (20)). The fitted parameters are already available in the literature reference and are listed in **Table 3.2**. Mixture adsorption loadings are then directly predicted by the extended dual-site Langmuir (EDSL) model (Equation (21)) [51].

$$q_i = q_{iA}^{sat} \frac{K_{iA} p_i}{1+K_{iA} p_i} + q_{iB}^{sat} \frac{K_{iB} p_i}{1+K_{iB} p_i},\ i,j = 1 \ldots N \text{ refers to the diffusing species} \quad (20)$$

$$q_i = q_{iA}^{sat} \frac{K_{iA} p_i}{1 + \sum_{j=1}^{N} K_{jA} p_j} + q_{iB}^{sat} \frac{K_{iB} p_i}{1 + \sum_{j=1}^{N} K_{jB} p_j} \quad (21)$$

where A or B represents the two different sites, q_i^{sat} is saturation loading of component i (mol.kg^{-1}), K_i is the Langmuir adsorption parameter (Pa^{-1}), p_i is the partial pressure (Pa), and N is the number of components.

3.3.2 Membrane Permeation

Multicomponent mixture permeation of an *M*-component mixture was modeled using the Maxwell-Stefan (M-S) formulation as discussed in **1.3.2 Multicomponent Mass Transport**[57]. The M-S equations are expressed in the M^{th} order matrix form of Equation (22)[60].

$$(N) = -\rho[q^{sat}][D](\nabla\theta) = -\rho[q^{sat}][B]^{-1}[\Gamma](\nabla\theta) \quad (22)$$

where (N) is the vector of molar fluxes of each species (mol.m^{-2}.s^{-1}), ρ is density of the membrane material (kg.m^{-3}), $[q^{sat}]$ is a diagonal M^{th} order matrix of saturation loadings of each species (where $q_i^{sat} = q_{iA}^{sat} + q_{iB}^{sat}$ mol.kg^{-1} based on the DSL model), $[D]$ is the M^{th} order Fick diffusivity matrix, and $(\nabla\theta)$ is the vector of gradients of fractional occupancy (θ) of each species. The Fick diffusivity matrix is the product of the two matrices $[B]^{-1}$ and $[\Gamma]$. The elements of these M^{th} order matrices are shown below (Equation (23)-(24)).

$$B_{ii} = \frac{1}{Đ_i} + \sum_{j=1, j\neq i}^{n} \frac{\theta_j}{Đ_{ij}} \tag{23}$$

$$\mathrm{B}_{ij} = -\frac{\theta_i}{Đ_{ij}}, i \neq j \tag{24}$$

Here, $Đ_i$ and $Đ_{ij}$ are the single-component M-S diffusivities ($m^2.s^{-1}$) of component *i*, and the exchange diffusivities of a pair of components *i* and *j*. The elements of the M^{th} order matrix $[\Gamma]$ are defined as:

$$\Gamma_{ij} \equiv (\frac{q_j^{sat}}{q_i^{sat}}) \frac{q_i}{p_i} \frac{\partial p_i}{\partial q_j} \tag{25}$$

These thermodynamic correction factors are introduced to express the chemical potential gradients in terms of the gradients of the fractional occupancy as given above[108]. In the present case, the partial derivative in Equation (25) are determined by numerical differentiation of the EDSL model (Equation (21)). The following assumptions and approximations were made:

(1) Only transport in the zeolite pores is considered, and contributions from defects are not included. This is an excellent assumption based upon the experimental data.

(2) Equilibrium exists at the interfaces between the membrane and the fluid phase. This is an established assumption in zeolite membrane modeling, and is valid for all but the thinnest (< 10 nm) membranes.

(3) The resistance of the support hollow fiber is neglected. Unlike the case of thicker membrane tubes and disks, the thin wall (~ 150 μm) of the hollow fiber leads to a very

high permeance of the support (e.g., 145,000 GPU for methane and 103,000 GPU for *n*-butane). Initial trials with unary M-S permeation equations indicated that the support effect was negligible, and it was not considered further.

(4) Concentration polarization effects are negligible. This is a reasonable assumption since the MFI pores (~ 0.55 nm) are permeable to all species and the feed pressures are not extremely high.

(5) Back-permeation of the argon sweep gas is neglected. Initial simulation trials that included argon back-permeation indicated that its effect was not significant due to its very weak adsorption in MFI, and it was not considered further.

(6) Preferred orientation effects were not explicitly included. Since the MFI membrane has significant <0*k*0> out-of-plane orientation, this effect is implicitly included in the fitted values of the diagonal M-S diffusivities as obtained from unary permeation data.

(7) The diagonal M-S diffusivities ($Đ_i$) is assumed to be independent of the loading. These assumptions are consistent with the simulation results in the literature[55, 58]. The off-diagonal components ($Đ_{ij}$) correspond to the diffusivities associated with the interaction between two different gas species.

(8) The Vignes relationship (Equation (26)) [51, 61] is used to estimate the counter-exchange (off-diagonal) diffusivities from the diagonal M-S diffusivities.

$$Đ_{ij} = Đ_i^{\theta_i/(\theta_i+\theta_j)} Đ_j^{\theta_j/(\theta_i+\theta_j)} \tag{26}$$

The M-S equations can be solved at any point along the axis of the hollow fiber membrane to determine the local flux, given the local composition of the feed and permeate. However, the experimental configuration (hollow fiber, with zeolite membrane

on the outer "shell" side and sweep gas on the inner "bore" side) also requires coupling the M-S equations to a differential mass balance on the sweep gas side. The "shell" side is assumed as perfectly mixed since there is a large feed flow rate which delivers a uniform composition at every location. On the "bore" side, the composition of the permeate changes from one end of the fiber to the other since the sweep gas progressively picks up the permeating components as it moves through the fiber. The differential mass balance for any component *i* on the sweep gas side is given by:

$$\frac{dn_i}{dz} = 2\pi r N_i \tag{27}$$

where z is the axial coordinate along the fiber (varying from 0 to L = 4 cm, which is the fiber length after epoxy sealing). n_i (mol.s^{-1}) is the molar flow rate of component *i* on the sweep gas side, r (m) is radius of the bore and N_i (mol.m^{-2}.s^{-1}) is permeate flux of component *i* entering the bore side at any location z, and is given by the M-S equations. Equation (27) was solved using an explicit method, simultaneously with equations (refer to M-S equations) based on a forward difference discretization scheme. The total molar flow rate of each species in the exit sweep gas is then divided by the total membrane area to obtain the average flux of that component through the membrane, which can then be used for permeance calculations using the same methods as in the experiments.

To solve these equations numerically, a MATLAB code was written by collaborator Akshay Korde.

3.4 Results and Discussion

3.4.1 Gas Permeation Properties of 2D MFI Membranes

Detailed membrane permeation measurements were carried out by techniques described in the **3.2.1 Permeation measurements** and **Figure 3.1**. The selected components were based upon a balance between realistic feed conditions (i.e., presence of the four main hydrocarbons of interest in the C_1-C_4 range) and the ease of producing feed mixtures over a wide pressure range using commercially available pre-mixed gas cylinders and pure components. Since our main focus is to examine the strong hydrocarbon adsorption effects, I do not include the small gas components such as CO_2, N_2, and H_2S. The mixtures also do not include *i*-butane or pentanes. The unary permeation properties of a 2D nanosheet-based MFI membrane at 298 K are shown in **Figure 3.2** as a function of transmembrane pressure differential. The flux values are obtained by measuring the molar flow rate of each species in the sweep when it exits the hollow fiber membrane, and then dividing by the total membrane surface area. The partial pressure driving forces (required for calculating the permeances) are obtained as the difference between the feed-side partial pressure and the partial pressure measured in the exit permeate stream. Because the partial pressures of the hydrocarbons in the exit sweep gas are very small, there is no significant need to use arithmetic or logarithmic-averaged partial pressures on the permeate side. The unary permeances decrease in the order of increasing carbon number of the hydrocarbons. This is because the smaller hydrocarbons have higher intrinsic (Maxwell-Stefan) diffusivities in the MFI pores.

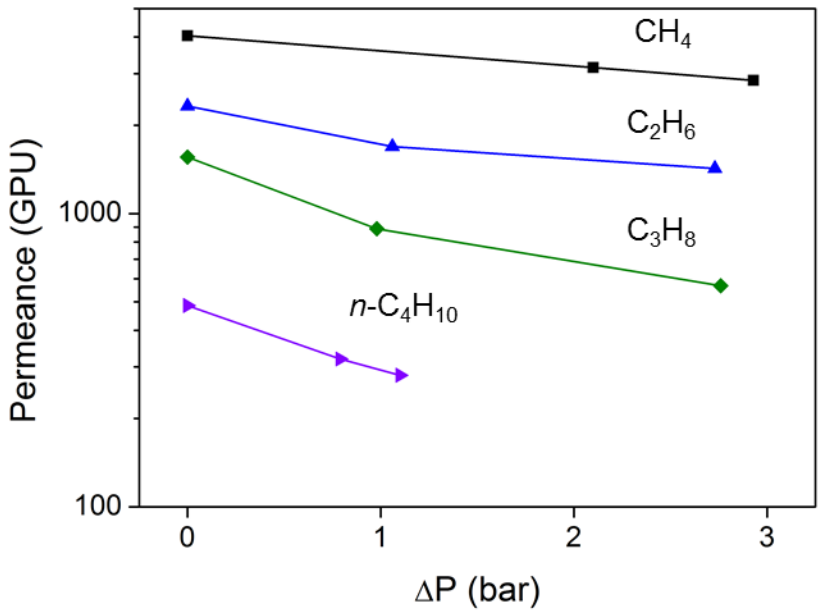

Figure 3.2 Unary permeances of hydrocarbons as a function of transmembrane pressure (ΔP) at 298 K.

Separation data for a 10/90 vol% *n*-butane/methane mixture is shown in **Figure 3.3(a)** as a function of transmembrane pressure differential. Whereas methane permeates much faster than *n*-butane in unary permeation, this effect is dramatically reversed in binary permeation. This is because of the strong competitive adsorption of *n*-butane in the MFI pores, thereby blocking adsorption and diffusion of methane. At higher zeolitic pore occupancies, the size entropy effect comes into play and boosts adsorption of methane to some extent [109], leading to lower (but still very high) *n*-butane/methane separation factor. The membrane exhibits excellent separation properties over the entire pressure range (*n*-butane permeance of 2500-800 GPU and separation factors of 250-125), with a strong pressure dependence, as expected for an adsorption-controlled separation.

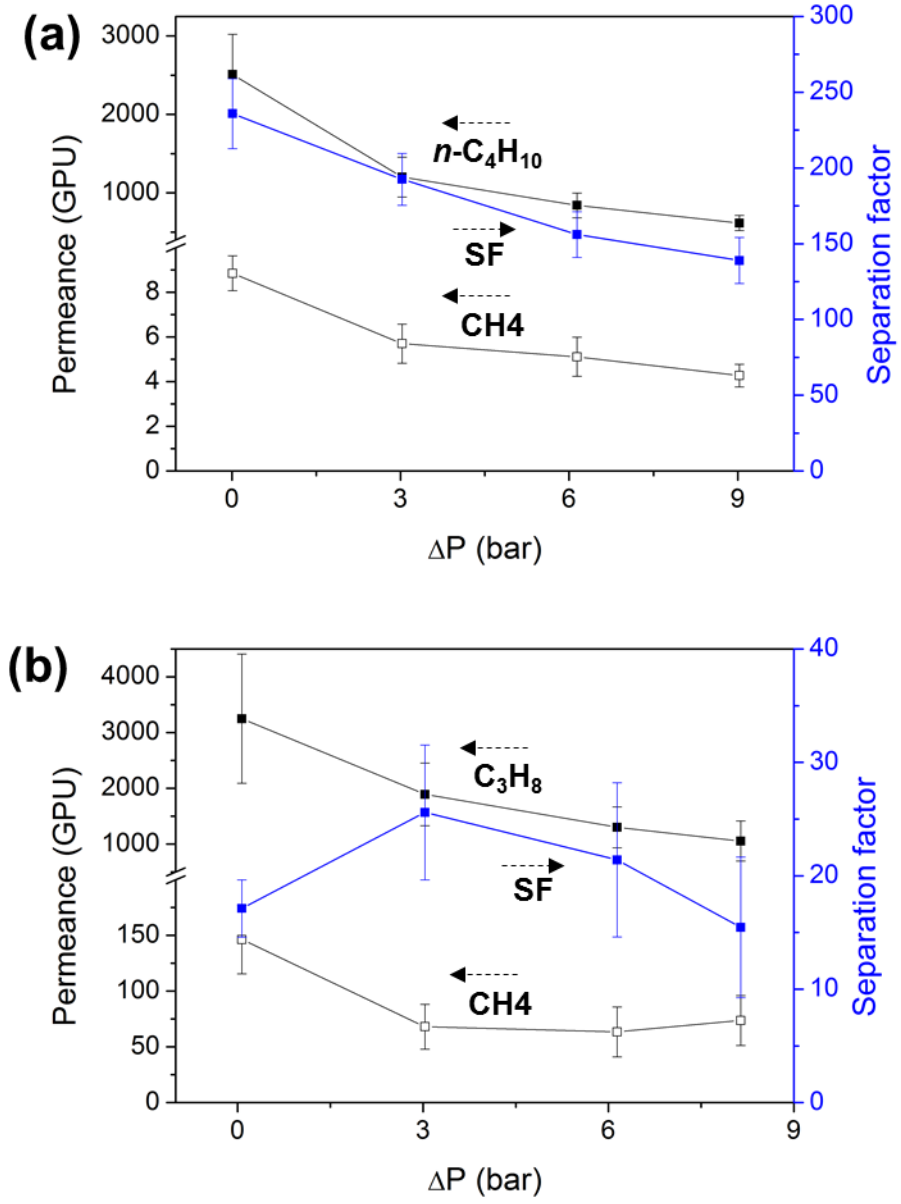

Figure 3.3 Permeances and separation factors at 298 K for (a) *n*-C_4H_{10}/CH_4 (10/90) binary mixture and (b) permeance and separation factor for C_3H_8/CH_4 (10/90) binary mixture, as a function of transmembrane pressure (ΔP). Error bars are obtained by measurements on three independently synthesized membrane samples.

The propane/methane binary separation behavior at 298 K is shown in **Figure 3.3(b)**. While high propane permeances (3200-1500 GPU) and good separation factors (15-25) are obtained, the pressure dependence of the separation factor and the methane permeance are substantially different from the *n*-butane/methane mixture. The separation factor shows a maximum at $\Delta P = 3$ bar and then decreases again. The permeance of methane initially decreases with increasing pressure, as expected, but it begins to rise again after 6 bar, with a ~20 GPU increase between 6 bar and 9 bar. This behavior cannot be explained as being due to non-zeolitic (defect) pores [110], since a 20 GPU permeance contribution from defects should also have been observed from the same membranes in the *n*-butane/methane case of **Figure 3.3(a)**, where the permeance of methane monotonically decreases. Rather, the above behavior is explained by the weaker adsorption of propane compared to *n*-butane. Propane requires a higher pressure than *n*-butane to saturate the MFI pores, and in this pressure region the separation factor increases with pressure as methane is progressively blocked. At higher pressures, methane is able to compete more effectively for adsorption with propane than with *n*-butane, resulting in a separation factor drop. A local maximum value in the separation factor at elevated feed pressure was also observed for ethane/methane mixtures in a previous report [87]. Overall, the binary mixture measurements clearly show the potential of the 2D nanosheet-based MFI hollow fiber membranes for NGL removal.

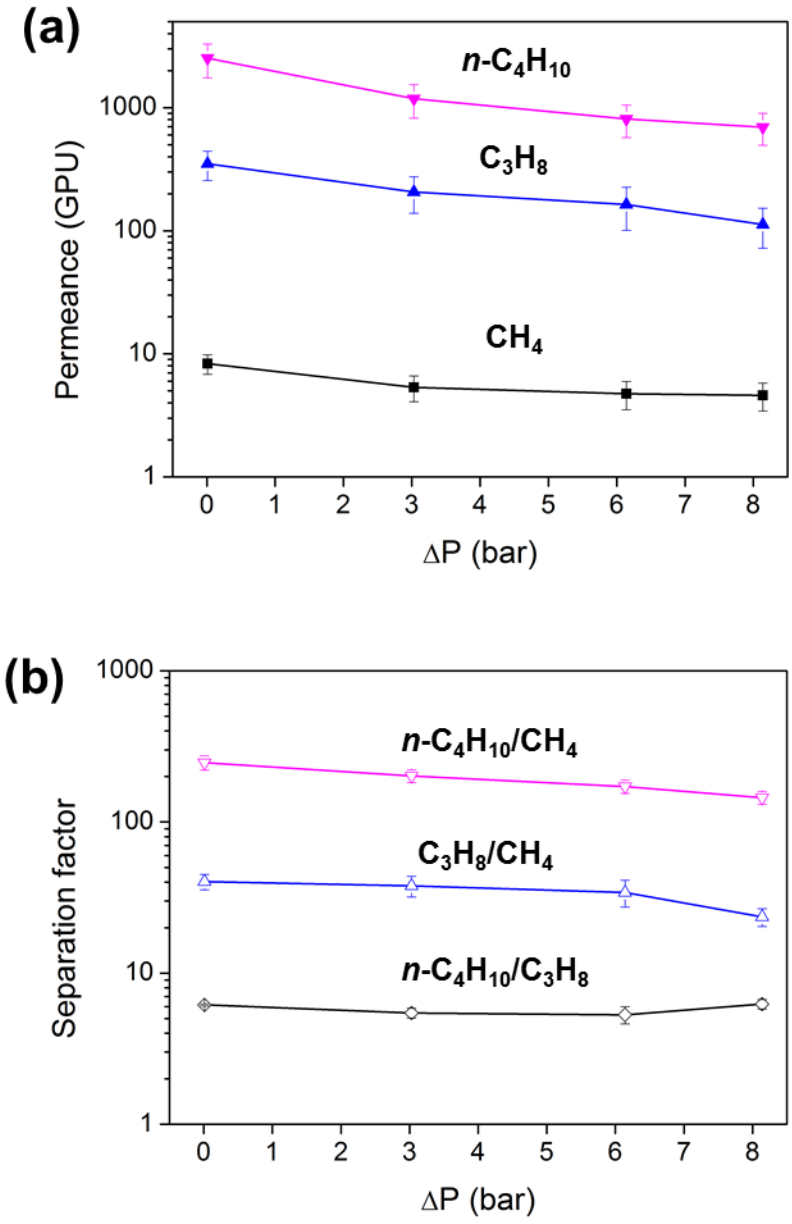

Figure 3.4 (a) Permeances and (b) separation factors observed for separation of *n*-$C_4H_{10}/C_3H_8/CH_4$ (9/9/82) ternary mixture as a function of transmembrane pressure (ΔP) at 298 K. Error bars are obtained by measurements on three independently synthesized membrane samples.

Next, I measured multicomponent ternary and quaternary mixture permeation properties of the membranes. **Figure 3.4(a)-(b)** show the ternary *n*-butane/propane/methane (9/9/82 vol%) mixture separation behavior at ΔP = 0-9 bar.

Excellent separation factors for higher hydrocarbons are maintained over the entire range of pressures. The largest difference between the ternary and binary cases is in the behavior of propane. The presence of *n*-butane is effective in greatly suppressing the permeation of methane in a manner similar to the binary case (**Figure 3.3(a)**). Although *n*-butane also suppresses the permeation of the weaker-adsorbing propane by almost an order of magnitude in comparison to **Figure 3.3(b)**, the net effect is that the propane/methane separation factor in **Figure 3.4(b)** (40-25 over the pressure range) is considerably enhanced over the binary case and no longer displays a maximum with increasing pressure. It is also worth noting that the membranes show a significant ternary *n*-butane/propane separation factor of ~6 over the pressure range.

In the final set of multicomponent measurements, I evaluated the membrane performance using an 8/8/8/76 vol% *n*-butane/propane/ethane/methane quaternary mixture (**Figure 3.5(a)-(b)**). The permeances follow the same trend as the adsorption strength of the species, and the membranes are selective towards all the C_{2-4} hydrocarbons over methane. The *n*-butane/methane and propane/methane separation factors are further enhanced over the ternary case. The membranes have a significant ethane/methane separation factor of 4-3 over the pressure range. The membranes show good *n*-butane/propane and propane/ethane separation factors over the entire pressure range. Additionally, the membranes display high performance in multicomponent feed mixtures at higher pressures. The detailed permeation data show no signs of significant non-zeolitic (defect) permeation over a large range of lower to higher feed pressures, leading to maintenance of significant selectivity between different pairs of hydrocarbons over the entire pressure range. As a result, the same MFI zeolite membranes can potentially be used

in multistage separations to debottleneck multiple distillation columns and produce enriched streams of all four hydrocarbons. The first stage (NGL removal from methane) would operate with higher-pressure feed gas (closer to the well-head pressure) to avoid recompression costs of the purified methane retentate product. On the other hand, the NGLs removed in the permeate of the first stage can be further separated at lower feed pressures without large recompression costs. The very high permeances of the MFI membranes enable this possibility as well.

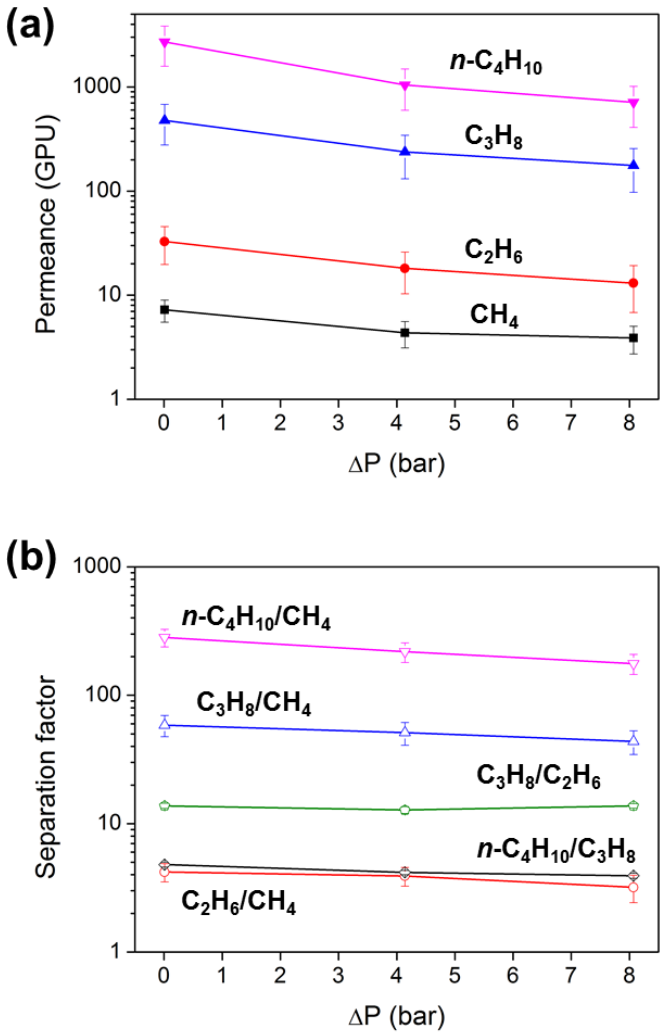

Figure 3.5 (a) Permeances and (b) separation factors observed for separation of a *n*-$C_4H_{10}/C_3H_8/C_2H_6/CH_4$ (8/8/8/76) quaternary mixture as a function of transmembrane pressure (ΔP) at 298 K. Error bars are obtained by measurements on three independently synthesized membrane samples.

Figure 3.6(a)-(b) show a comparison of the permeation properties of all four hydrocarbons in unary and mixture permeation at a total transmembrane differential pressure, $\Delta P = 0$ bar (ethane is included only in the unary and quaternary cases). As compared to the permeance of propane in the unary and propane/methane binary mixtures, it permeates an order-of-magnitude slower in the presence of *n*-butane in the ternary and quaternary mixtures. Ethane and methane also behave similarly, but to differing extents. The unary permeance of ethane is dramatically reduced by almost two orders of magnitude in mixture permeation, whereas methane permeation is reduced by nearly three orders of magnitude. On the other hand, the presence of propane and ethane has very little effect on *n*-butane permeance. The main feature of *n*-butane permeation is the dramatic permeance increase between the unary and mixture cases. In the unary case at 1 bar, *n*-butane has near-saturated adsorption and the actual driving force would not increase proportionally at such a saturated pore occupancy. Thus, the permeance based on the pressure difference decreases and it is lower than the mixture case in which partial pressure of *n*-butane is lower [111]. The separation factors of the three heavier hydrocarbons over methane show a general increase from the unary to the quaternary case, since the overall increase in their proportion leads to further suppression of methane permeation. This effect of a multicomponent mixture system on the separation selectivity is more clearly observed when a sweep gas is used to maintain a low hydrocarbon chemical potential on the permeate side (as in this work). It was not observed in previous work [7], in which the ternary separation factors were lower compared to the binary mixtures in the absence of a sweep gas. Indeed, the adsorption-dominated separation performance of MFI membranes is highly influenced by the desorption conditions on the permeate side, as demonstrated

previously [104]. **Figure 3.7** shows the corresponding data at the highest pressures studied (ΔP = 8 or 9 bar dependence on the mixture). Unary data were not measured at high pressures. The overall conclusions are similar to those discussed above.

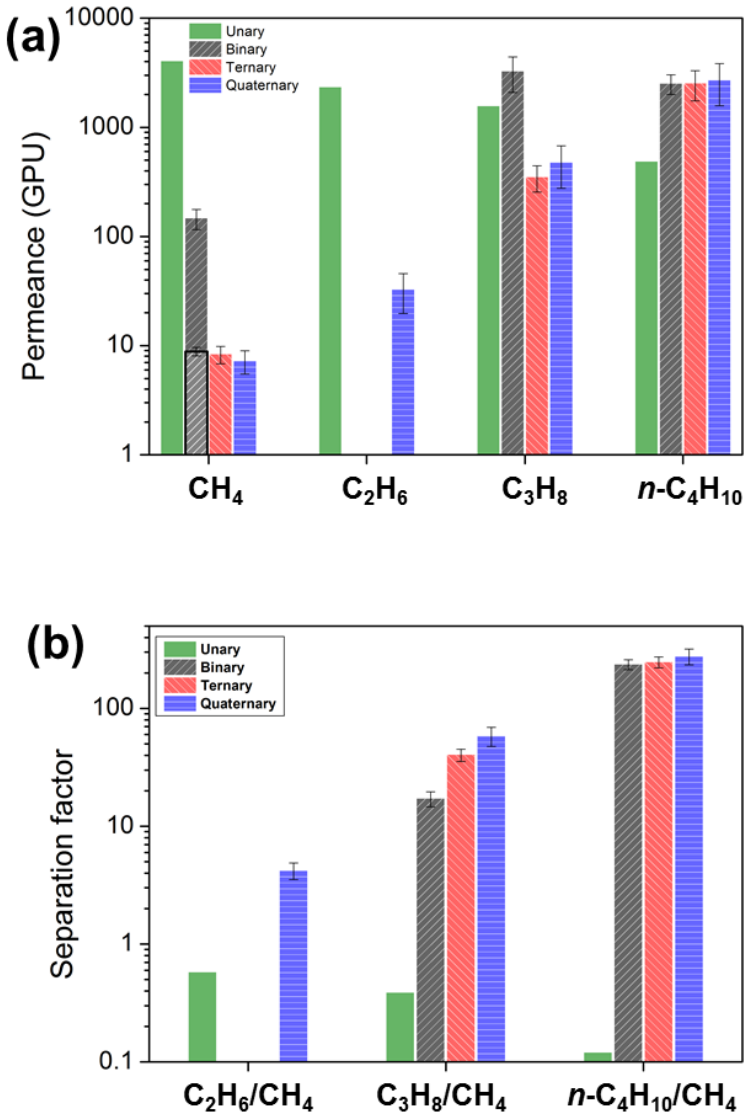

Figure 3.6 (a) Unary and multicomponent permeances in MFI membranes at 298 K and ΔP = 0 bar for CH_4, C_2H_6, C_3H_8 and *n*-C_4H_{10}; and (b) corresponding separation factors of C_2H_6/CH_4, C_3H_8/CH_4 and *n*-C_4H_{10}/CH_4 at ΔP = 0 bar. For unary permeation, ideal selectivities (ratios of unary permeances) are shown. Legend: Green = unary, Grey = binary (10/90 C_3H_8/CH_4 or *n*-C_4H_{10}/CH_4), Red = ternary (9/9/82 *n*-$C_4H_{10}/C_3H_8/CH_4$), Blue = quaternary (8/8/8/76 *n*-$C_4H_{10}/C_3H_8/C_2H_6/CH_4$). The CH_4 permeance for binary *n*-C_4H_{10}/CH_4 mixture is displayed with the border. The unary data is from a single membrane sample, whereas for the multicomponent data three independently fabricated samples were used.

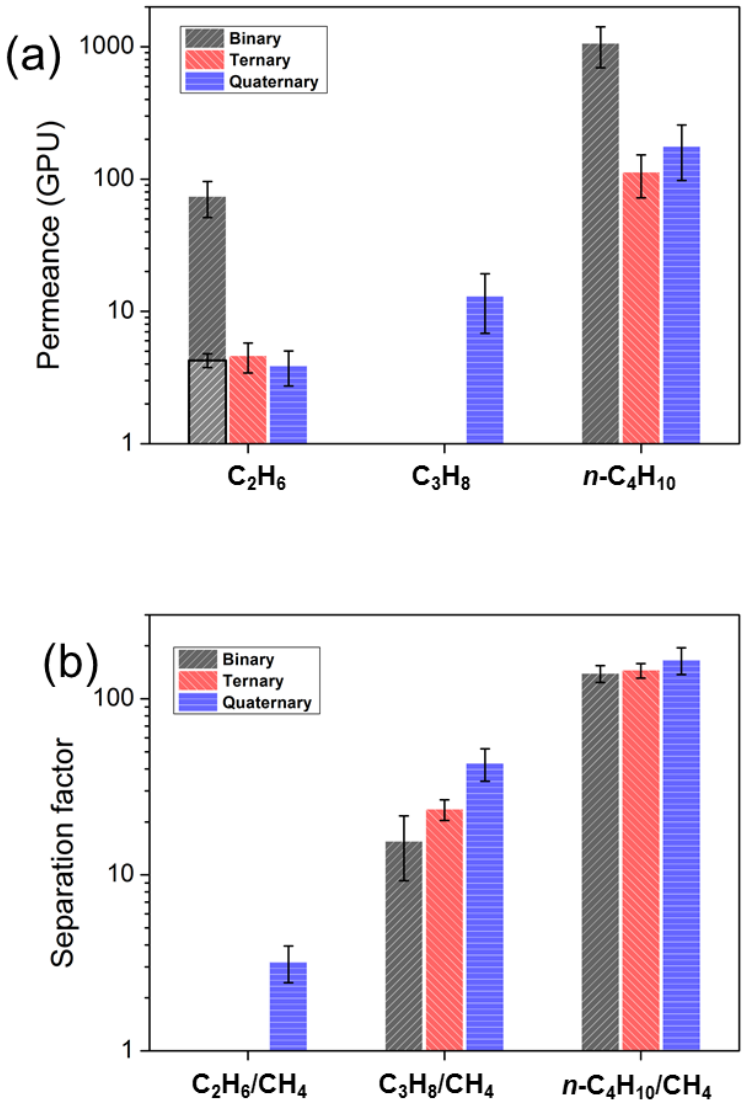

Figure 3.7 Multicomponent permeances in MFI membranes at 298 K and ΔP = 8 or 9 bar for CH_4, C_2H_6, C_3H_8 and *n*-C_4H_{10}; and (b) corresponding separation factors of C_2H_6/CH_4, C_3H_8/CH_4 and *n*-C_4H_{10}/CH_4 at ΔP = 0 bar. Grey = binary (10/90 C_3H_8/CH_4 or *n*-C_4H_{10}/CH_4), Red = ternary (9/9/82 *n*-$C_4H_{10}/C_3H_8/CH_4$), Blue = quaternary (8/8/8/76 *n*-$C_4H_{10}/C_3H_8/C_2H_6/CH_4$). The CH_4 permeance for binary *n*-C_4H_{10}/CH_4 mixture is displayed with the border. The multicomponent data is from three independently fabricated samples.

3.4.2 Prediction of Multicomponent Adsorption

To predict and understand the multicomponent permeation behavior in more detail, I and collaborator Akshay Korde modeled multicomponent transport in the MFI membranes with the Maxwell-Stefan (M-S) approach. Since there is a large range of possible feed compositions, pressures, and desorption conditions, a predictive multicomponent model can be very useful to ascertain the general trends in permeation behavior without need for extensive experimentation. This model could also be easily extended to add other components such as the small gases, butane isomers, or trace amounts of higher hydrocarbons (C_{5+}). Our objective here is not to make quantitatively accurate predictions over all the operating conditions by performing extensive parametrization. Rather, I take the approach of making qualitatively useful predictions, employing the unary adsorption (Configurational-bias Monte Carlo simulated data [51]) and experimental diffusion data to parametrize the M-S equations along with well-known theoretical approximations for multicomponent adsorption and exchange diffusion behavior. **3.3 Modeling Methods** contains a detailed account of the modeling methods and equations [57, 58, 60, 61, 108].

Detailed unary adsorption isotherm data are available for C_1-C_4 hydrocarbons in high-silica MFI zeolite at 300 K [51], which is close to the condition of our membrane permeation measurements and allows the data to be used directly. **Figure 3.8(a)** shows the fitted unary predictions with the dual-site Langmuir (DSL) model, revealing the large differences in adsorption behavior between the four components as a function of pressure. The DSL parameters are already shown to provide an excellent fit to the unary adsorption data [51], and these parameters are listed in **Table 3.2**. The DSL model accounts for the

presence of two different adsorption sites in the MFI pore structure, such as the channel intersections and the straight channels. There are several options available for multicomponent adsorption predictions. The ideal adsorbed solution theory (IAST) equations [112] are often used to predict the multicomponent adsorption isotherms. Although it is expected that the IAST model would predict the adsorption behavior of hydrocarbons in MFI quite well [55], its use in multicomponent M-S transport modeling is inconvenient due to its computational inefficiency. On the other hand, the extended dual-site Langmuir (EDSL) model is convenient due to its simple mathematical form that captures both the competitive and dual-site aspects of hydrocarbon adsorption in MFI. Initial trials showed that both methods predict identical trends in adsorption selectivity as a function of pressure and composition, although the numerical values of component uptakes and adsorptive separation factors can differ. Therefore, I proceeded to select the EDSL model for further calculations, without undertaking any detailed comparison of IAST and EDSL predictions. For example, **Figure 3.8(b)** shows the EDSL prediction of quaternary mixture adsorption as a function of total pressure with the same 8/8/8/76 vol% mixture used for membrane permeation measurements. The EDSL model clearly predicts the large suppression of ethane and methane adsorption in the presence of propane and *n*-butane. The EDSL model also predicts the strong pressure dependence of quaternary mixture adsorption separation factors, as shown in **Figure 3.8(c)**. The adsorption separation factor for a pair of components is defined as the ratio of the moles of the two components adsorbed in MFI, divided by the molar ratio of the components in the fluid phase. Similar to the observed quaternary mixture permeation trends, the adsorption separation factor decreases with increasing total pressure and the magnitude of the

adsorption separation factor (of higher hydrocarbons over methane) follows the order of adsorption strength of the higher hydrocarbon.

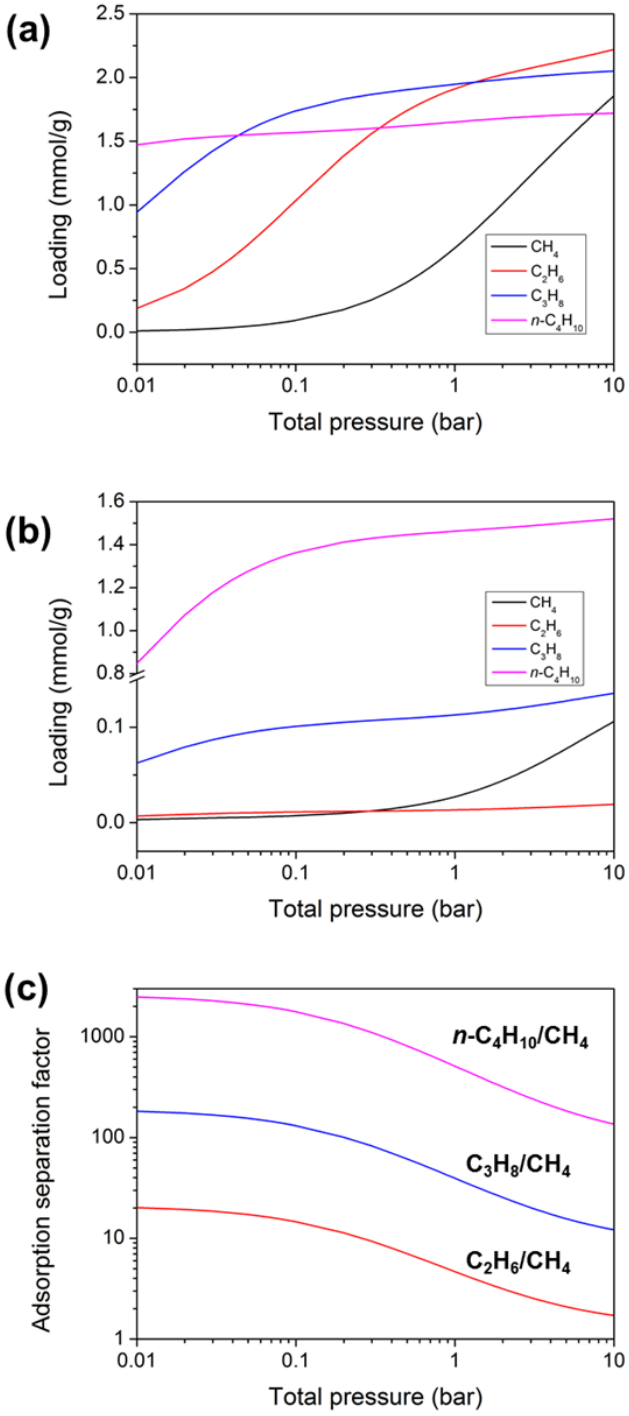

Figure 3.8 (a) Predictions of unary hydrocarbon adsorption in MFI at 300 K by the Dual-Site Langmuir model (fitted parameters in **Table 3.2** [51]). Predictions of adsorption from a quaternary mixture (8/8/8/76 vol% *n*-C_4H_{10}/C_3H_8/C_2H_6/CH_4) by the Extended Dual-Site Langmuir model: (b) adsorption uptakes of each mixture component at different total pressures, and (c) corresponding adsorption separation factors.

3.4.3 Prediction of Multicomponent Permeation

Membrane permeation was modeled by the multicomponent M-S equations (see **3.3 Modeling Methods** for details of the model formulation and assumptions). The required unary M-S diffusivity parameters were obtained by fitting our experimental unary permeation data (**Figure 3.2**) to the M-S equation for each component, with the DSL model to describe the unary adsorption characteristics. **Figure 3.9** shows these results. Considering the different approximations inherent in our approach, a reasonably good fit is obtained. As expected, the intrinsic M-S diffusivity of methane is much higher than that of the other components. With these diffusivity parameters and the multicomponent approximations listed in the **3.3 Modeling Methods**, I can investigate a number of different aspects of multicomponent separations with the MFI membranes.

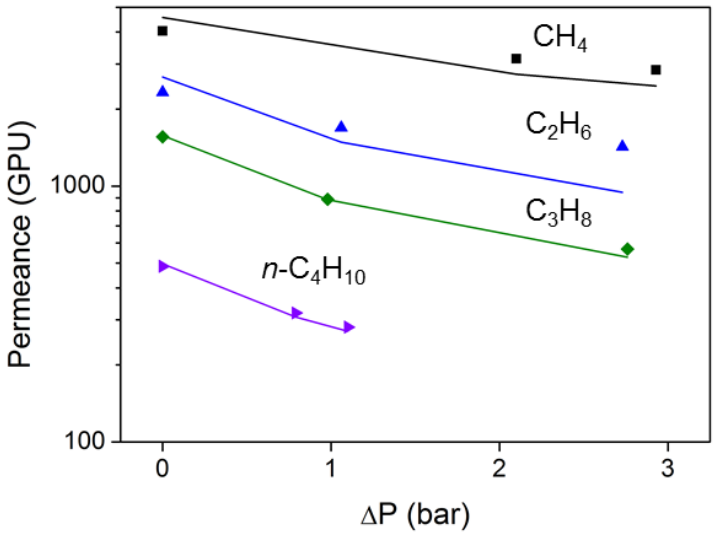

	methane	ethane	propane	*n*-butane
$Đ_i$ (10^{-12} m²/s)	120	17	8.3	2.5

Figure 3.9 Fitting of experimental unary permeation data (same as **Figure 3.2**) with the Maxwell-Stefan unary permeation equation (solid lines), and the fitted Maxwell-Stefan diffusivity values. The membrane thickness used was 830 nm based upon the SEM data.

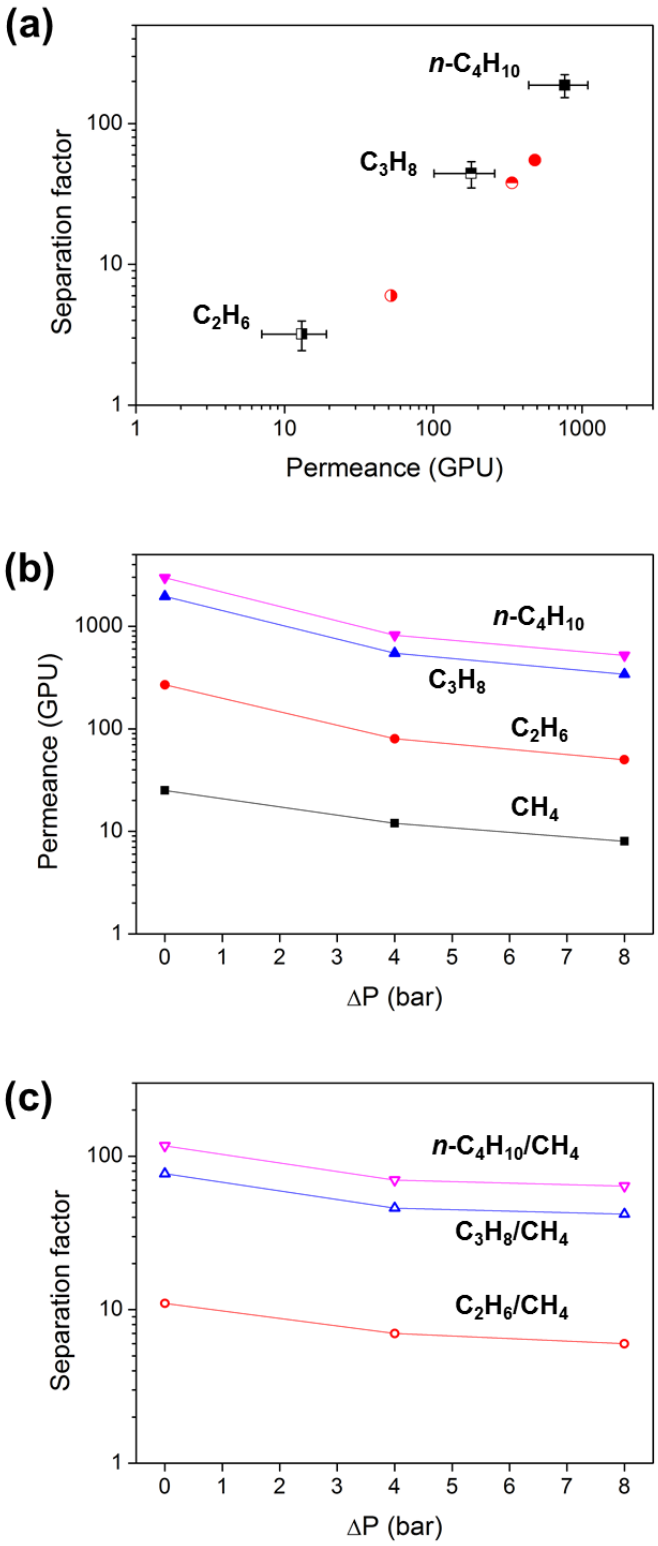

Figure 3.10 (a) Comparison of the Maxwell-Stefan predictions of permeances and separation factors for the quaternary mixture at ΔP = 8 bar with the experimental results. Maxwell-Stefan predictions of the pressure dependence of (b) permeances and (c) separation factors.

Figure 3.10(a) compares the M-S model predictions with experimental permeances and separation factors (of the three higher hydrocarbons over methane) for the quaternary mixture at $\Delta P = 8$ bar. The M-S model correctly captures both the remarkable inversion of selectivity relative to unary permeation, as well as the changes in order of magnitude of permeances of each component. Quantitative differences with the experimental data can be ascribed mainly to the limitations of the Vignes relationship for predicting the counter-exchange coefficient, and the EDSL approximation of the adsorption behavior. It was previously reported that the flux of weaker-adsorbing species (here, methane and ethane) can be over-predicted by Vignes relationship [113], leading to under-prediction of the *n*-butane separation factor over these species (as seen in **Figure 3.10(a)**). Furthermore, the pressure-dependences of all the permeances and separation factors (**Figure 3.10(b)-(c)**) predicts the same trends as seen in **Figure 3.5**. While quantitative discrepancies exist between the experimental and predicted values, the excellent qualitative correspondence supports the validity of the present model for examining the trends in separation performance under different operating conditions.

First, I modeled the effect of the permeate-side desorption conditions on the quaternary separation, by varying the sweep gas flow rate (**Figure 3.11(a)-(b)**). Upon reducing the sweep gas flow rate from 120 mL/min (60 mL/min is the value used in all the foregoing experiments and model calculations) to values as low as 10 mL/min, I find that the permeances of methane, ethane, and propane (and the corresponding separation factors) are not significantly affected. These components do not have difficulty in desorbing on the permeate side even with increased concentrations on the permeate side due to a reduction in sweep gas flow. On the other hand, the *n*-butane permeance shows a considerable

decrease (due to desorption limitations) upon lowering the sweep gas rate. Nevertheless, quite high *n*-butane permeances (> 300 GPU) and separation factors (~40) are still obtained at the lowest sweep flow rate. Moreover, the model under-predicts the *n*-butane permeance (as discussed earlier) and the actual permeance may be considerably higher. Next, I examined the effect of reducing the total NGL content in the feed stream at fixed $\Delta P = 8$ bar and sweep flow rate of 60 mL/min (**Figure 3.11(c)-(d)**). It is found that higher permeances and separation factors are obtained for all components at lower total NGL content. Even though the fluxes of NGL components would decrease somewhat because of the reduced driving force, it appears that methane permeance can still be substantially suppressed and high separation performance can be achieved even at smaller concentrations of NGL components. Finally, for the case of a 2/2/2/94 quaternary stream, I examine the effect of operating at a higher $\Delta P = 14$ bar since condensation at 6% total NGL is not a concern. As seen in **Figure 3.11(e)-(f)**, there is only a slight downward trend of permeances and selectivities with increasing pressure.

For all the above cases, the corresponding predicted fluxes (which are of greater practical interest than the permeances) are shown in **Figure 3.12**. Several noteworthy observations are made. First, a reduction in the sweep gas flow rate leads to a large decrease in the *n*-butane flux due to the inefficient permeate side desorption. Second, the C_2-C_4 hydrocarbon fluxes decrease when reducing the total NGL content in the feed stream. On the contrary, the methane flux increases due to the enhanced pressure gradient at lower total NGL content. Finally, for the 2/2/2/94 vol% quaternary stream, the higher operating feed pressure is found to increase the fluxes of all components, with the methane flux substantially affected due to the size entropy effect at higher pore occupancies. Despite

a slight decrease in selectivities, a high flux at high pressure can compensate for such a loss of selectivities.

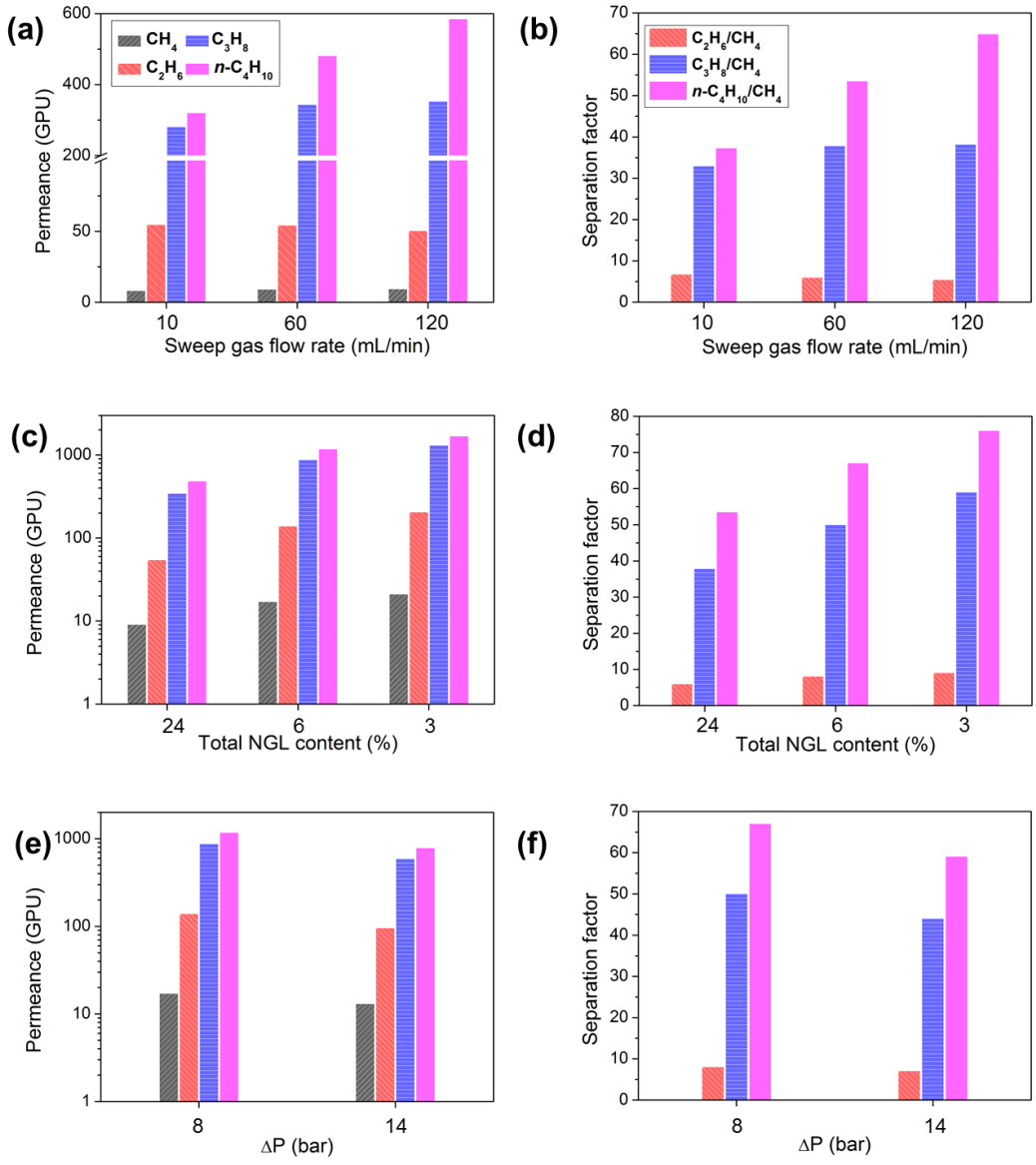

Figure 3.11 Predicted effect of sweep gas flow rate on (a) permeances and (b) separation factors in quaternary mixture separation at ΔP = 8 bar. Predicted effect of the total NGL content (with fixed 1/1/1 ratio *n*-butane/propane/ethane) on (c) permeances and (d) separation factors at Δ P = 8 bar. Predicted effect of operation at higher pressure (Δ P = 14 bar) for a 6% NGL feed (with fixed 1/1/1 ratio *n*-butane/propane/ethane) on (e) permeances and (f) separation factors.

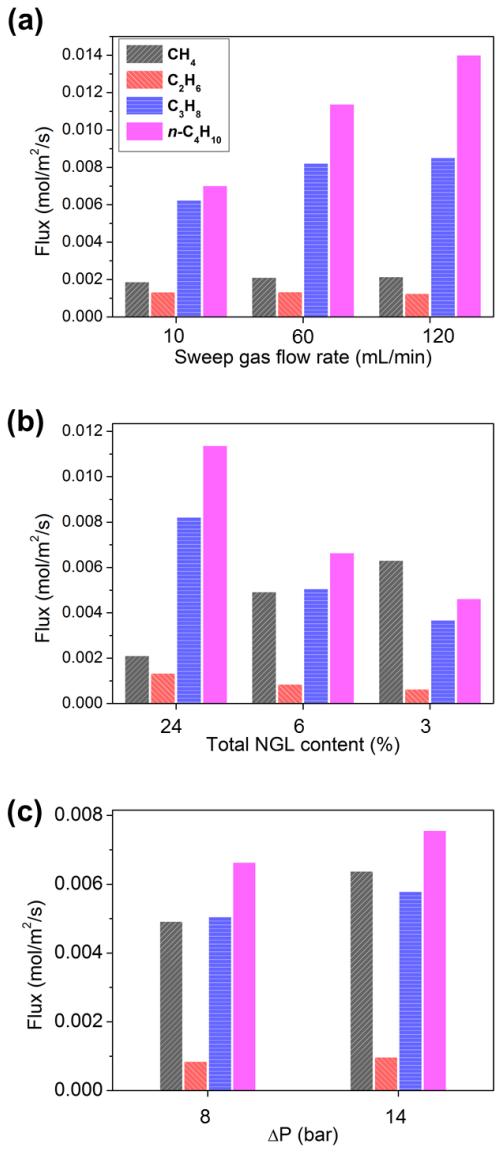

Figure 3.12 Predicted effect of (a) sweep gas flow rate, (b) total NGL content (with fixed 1/1/1 ratio *n*-butane/propane/ethane) at Δ P = 8 bar on fluxes in quaternary mixture and (c) Predicted effect of operation at higher pressure (Δ P = 14 bar) for a 6% NGL feed (with fixed 1/1/1 ratio *n*-butane/propane/ethane) on fluxes in quaternary mixture

Overall, these results have important implications for evaluating the performance economic viability of MFI hollow fiber membranes in the actual natural gas processing. Better quantitative accuracy in M-S modeling may be achieved by the use of molecular simulations to provide multicomponent adsorption data as well as better estimates of

counter-exchange diffusivities. Extension of the M-S model to include other components of shale gas (**Table 3.1**) would provide additionally realistic performance predictions.

3.5 Conclusion

In this study, 2D MFI-based hollow fiber membranes with favorable microstructure (thin and [0*k*0] out-of-plane orientation) were investigated for the removal of natural gas liquid (NGL) components (*n*-butane, propane, and ethane) from methane. The present membranes show excellent separation performance in the *n*-butane/propane/ethane/methane quaternary mixture at elevated feed pressures of up to 900 kPa. They are highly selective towards strongly adsorbing molecules such as *n*-butane and propane (e.g., *n*-butane/methane separation factor of 170 and *n*-butane permeance of 710 GPU at 900 kPa feed pressure) and also show selectivity for different pairs of hydrocarbons. As a result, such membranes could be used in a single stage for NGL removal from methane, and thereafter in a multistage cascade to fractionate the NGLs into streams rich in ethane, propane, and butane. Finally, I and collaborator Akshay Korde applied Maxwell-Stefan modeling to describe the multicomponent mixture transport behavior in a wide range of operating conditions (feed pressure, sweep gas flow rate and feed compositions), and demonstrated the potential utility of the present membranes in natural gas processing. The promising performance characteristics of the present membranes, combined with our concurrent advances in improving the scalability of zeolite membranes, could accelerate industrial applications of MFI zeolite membranes in hydrocarbon processing.

CHAPTER 4. SINGLE-STEP SCALABLE FABRICATION OF MFI HOLLOW FIBER MEMBRANES FOR HYDROCARBON SEPARATIONS

4.1 Introduction

Zeolite membranes have generated extensive attention over the past two decades because of their well-defined and robust microporous crystalline structures that enable molecular separation in industrially relevant chemical mixtures [114]. Among several different types of zeolite membranes, MFI-type zeolite membranes have been particularly studied for hydrocarbon separations. The MFI structure possesses pore sizes (0.56 nm × 0.54 nm along the *b*-axis and 0.51 nm × 0.55 nm along the a-axis) [23, 115] and adsorption properties that are attractive for the separation of xylene isomers [3], butane isomers [85] and removal of C_{2+} hydrocarbons from natural gas [7].

Despite a number of important advances in MFI membrane fabrication and performance, challenges persist in scalable, quality-controlled, and economical fabrication that hinder its industrial implementation [114]. There have been mainly two routes for the zeolite membrane synthesis: seeded secondary growth and in situ growth methods. The former technique involves a separate zeolite nanocrystal seeding step on the support and subsequent hydrothermal secondary growth into a continuous membrane. The crystal seeds promote nucleation and crystal growth on the substrate surface and thus membrane quality have less influence from the substrate chemistry and quality [43, 116]. This method also provides better control over membrane morphologies and parameters such as crystal

orientation [20, 36, 117] and thickness [35]. While high separation performance could be achieved, the multiple fabrication steps require delicate handling, limiting the reproducibility and transfer to larger scales [63]. In situ growth involves direct crystallization of the MFI zeolite membrane on the support without a separate seeding step. This method has the theoretical advantage of requiring only one step. However, due to the difficulty of nucleating MFI crystals with high surface density on the support, a single growth iteration is often not sufficient to form a defect-free membrane. Therefore, most previous reports have relied on multiple (2 – 5) iterations to achieve good selectivity. However, this results in thick membranes (several microns) with relatively low permeance (see **Table 4.1** for a comparison of several studies based upon this method). Recently, a third method has emerged based upon the use of high aspect ratio (2D) MFI zeolite nanosheets for coating/seeding the support before secondary growth. Unlike conventional seeding with nanoparticles, the nanosheets allow full coverage of the support surface. Minimal secondary growth is required to form a continuous membrane and hence the final membrane thicknesses can be much lower (< 100 nm). [28, 29, 33, 65, 76, 118, 119] Secondary growth can even be achieved without bulk hydrothermal conditions, by the use of special silica supports that can supply the silicate precursors to the membrane layer. While this method enables unprecedented permeances and selectivities, it still requires multiple fabrication steps including the preparation, potential exfoliation, and coating of the 2D MFI nanosheets. A common challenge in all the above-mentioned fabrication methods is scalability and cost. On the laboratory scale, it is common to fabricate membranes on flat or tubular supports. On a large scale, such supports would afford very low surface-to-volume ratios and membrane packing densities [120]. Also, asymmetrical

tubular supports are typically used to improve the membrane permeance and minimize the membrane defects. These highly engineered supports require multiple processing steps and would significantly increase the fabrication cost. Although high throughput associated with zeolite membranes may be able to reduce the overall membrane system size requirements significantly and thus drive down the "per-unit-purified-product" cost of the membrane separation, it is also necessary to lower the per-unit-area membrane costs which currently make zeolite membranes prohibitively expensive in large-scale gas or hydrocarbon separations [43, 116, 121, 122].

Recently, the Nair group has demonstrated the one-step fabrication of high-silica CHA zeolite membranes on low-cost *a*-alumina hollow fibers with the use of a concentrated precursor gel [123], which may be considered as a fourth method for zeolite membrane fabrication. Low-cost and mass-produced hollow fiber supports (with diameters < 1 mm) could be an excellent alternative to dramatically reduce the overall membrane fabrication cost and to increase the membrane area per unit volume. These small-pore (~0.38 nm) CHA hollow fiber membranes provided excellent permeances and selectivities for small gas molecules like H_2 and CO_2 over larger gases and hydrocarbons, but are not suitable for hydrocarbon separation applications. Zeolite membrane fabrication techniques are, in general, not readily transferable between different zeolite types since the conditions and characteristics of nucleation and growth of different zeolite frameworks can be vastly different. Inspired by our previous work on CHA membranes, our main objective in the present work is to develop a one-step in situ fabrication method for the preparation of high-quality (thin and defect-free) MFI membranes on *a*-alumina hollow fibers. Along this direction, I demonstrate a gel-based in situ method for the preparation of thin MFI zeolite

membranes in a technologically scalable manner, based upon the use of concentrated precursor gel containing MFI nanocrystals. This method results in thin (~ 1 μm) and highly selective MFI membranes exhibiting high separation performances for the separation of butane isomers and the removal of natural gas components (NGL) such as *n*-butane, propane, and ethane from methane.

Table 4.1 Summary of the reported MFI membranes prepared by in situ crystallization methods; and comparison to the MFI membranes in this work. (1 gas permeation unit (GPU)=3.348×10^{-10} $mol.m^{-2}.s^{-1}.Pa^{-1}$)

Support type	**Membrane fabrication method (in situ)**	**Characterizations**	***n*-butane (GPU), (*n*-/*i*-butane Separation factor)**	**Year**	**Reference**
Alumina tube (6.5 mm i.d.) with multiple layers of different alumina	▪ 2 – 3 times synthesis ▪ The membranes vertical orientation was switched	-	176, (20)	1995	[124]
Alumina disk	1 time synthesis	-	22, (18)	1995	[125]
Alumina disk	1 – 4 times synthesis	5 μm thickness	90, (52)	1996, 1998	[78, 86]
Stainless steel disk with a metal wool layer	1 time synthesis resulted in 80 % failure	30 – 50 μm thickness	149, (25)	1998	[87]
Unsupported	1 time synthesis	▪ 50 μm thickness ▪ Grown on the Teflon disk	239, (48)	2000	[81]

Table 4.1 continued

Stainless steel tube (7 mm i.d., 10 mm o.d.)	▪ Dipping-drying the gel (4 – 5 times) ▪ Steam-assisted crystallization ▪ 4 times synthesis	>100 µm thickness	6, (5)	2001	[79]
TiO_2 (100 nm) coated stainless steel disk	1-time synthesis	35 µm thickness	149, (55)	2001	[82]
Alumina tube (7 mm i.d., 10 mm o.d.)	1 – 2 times synthesis	-	-	2001	[126]
TiO_2 (100 nm) coated stainless steel tube (10 mm o.d.)	2 times synthesis at different temperature (nucleation & crystallization)	15 µm thickness	418, (45)	2005	[88]
Dual layer alumina disk	▪ 1-time synthesis ▪ Mesoporous silica sublayer	▪ *b*-oriented ▪ 2-3 µm thickness	(Pressure gradient method) 6, (3)	2005	[41]
Stainless steel tube, alumina tube	▪ 2 – 3 times synthesis ▪ Outer/inner side	-	(Pressure gradient method) 29, (8)	2008	[127]
Alumina fiber (1.2 mm i.d., 1.7 mm o.d.) with additional layers	▪ Pore-plugging (membrane formed within the support)	▪ Effective thickness 0.6-1.2 µm ▪ Support pore size has strong influence on the quality	-	2006, 2010	[120, 128]

Table 4.1 continued

Alumina fiber (2.5 mm i.d., 3.5 mm o.d.)	▪ Piranha treatment to introduce more hydroxyl groups on the support	-	-	2013	[129]
Alumina fiber (0.75 mm o.d.)	**▪ 1 time synthesis** **▪ Nanocrystal seed loaded concentrated gel**	**Highly reproducible, scalable**	**434, (60)**	**2020**	**This work**

4.2 Experimental Methods

4.2.1 Materials

For MFI nanocrystal and precursor gel preparation, sodium hydroxide (97 % wt.), silicic acid (99.9 % wt., 20 μm) and LUDOX SM-30 colloidal silica (30 % wt.) were purchased from Sigma-Aldrich. Tetrapropylammonium hydroxide solution (TPAOH, 40 % wt.) was purchased from EMD Millipore.

4.2.2 Preparation of the Precursor Gel

For the preparation of the precursor gel, MFI nanocrystals were synthesized as provided in previous literature [29] and detailed characterizations are given in **Figure 4.2**. The concentrated precursor gel was prepared based on the evaporation of the solvent with an initial sol composition of 1 SiO_2 : 0.12 TPAOH : 60 H_2O. Typically, 2.44 g of TPAOH (40 % wt.) was added to 36g of D.I. H_2O under stirring. Then, 8.01 g of LUDOX SM-30 silica sol (30 % wt.) was added, after which 0.12 g of MFI nanocrystals were added (the

MFI nanocrystal mass is fixed at 5 % wt. of the total mass of SiO_2 from the LUDOX SM-30 silica sol). The mixture was then stirred and evaporated in the oil bath (temperature was set to 373 K) to remove the excess H_2O and make the precursor gel to be concentrated. The mass of H_2O evaporated was periodically monitored to yield a final concentrate precursor gel with a composition of 1.0 SiO_2 : 0.12 TPAOH : 5 H_2O (mass of MFI nanocrystal is not included). 39.1 g of mass loss yielded a targeted final gel composition.

4.2.3 Synthesis of MFI Membranes via In Situ Methods

The preparation of α-alumina hollow fibers is generally the same as our recent work [76].

For liquid gel-based MFI membrane synthesis on the outer surfaces of the hollow fibers, I used the home-made cylindrical PTFE holders (⅞" OD) which have a ¼" drilled channel [123]. Prior to the synthesis, hollow fibers with a glaze-sealed end at the bottom were pre-filled with H_2O in the bore side to avoid the crystallization inside the bore. Since the liquid-like precursor gel is in contact with the hollow fiber during the synthesis, it is highly likely to have the penetration of the precursor gel into the inner side of the fiber which could result in crystal growth on the bore side. In order to avoid this, the bore side of the hollow fibers was pre-filled with H_2O before the crystallization, which is expected to help reduce the penetration of the precursor and the crystal growth on the inner side of the fiber. To fill the bore side with H_2O without remaining air pockets, hollow fibers were soaked into the H_2O and vacuum was applied. H_2O pre-filled 3 hollow fibers were inserted into the channel. Then, the concentrated precursor gel was injected into the channel. The level of the gel was adjusted so that the bore side of the hollow fibers were not filled with

the gel. The PTFE holder was then placed inside the 45 mL Teflon liner and sealed in a 45 mL autoclave. The 2 mL of H_2O was injected between the PTFE holder and the Teflon liner to avoid complete vaporization of the precursor gel. The sealed autoclave was then kept at 448 K for 16 or 32 h. After the synthesis, the fibers were removed from the holder and soaked in D.I. H_2O and then dried in an oven at 343 K. As-dried membranes were calcined under air in an oven at 753 K for 4 h with a ramping rate of 0.5 K/min. The membranes grown for "16 h" and "32 h" are denoted as "M1" and "M2" (**Table 4.2**), respectively.

For the synthesis of 10 membranes in a single batch, 10 hollow fibers were put into the same ¼" channel and the other preparation procedures were kept identical.

For membrane synthesis via the solid-gel vapor-phase crystallization method, the concentrated precursor gel was prepared as mentioned earlier. The concentrated precursor gel was put into the ¼" channel drilled PTFE holder. The bare hollow fiber was then vertically soaked into the gel and kept for 3 min for coating. After 3 min, the gel-coated fiber was slowly taken out from the PTFE holder and subjected to drying in an oven at 343 K for 15 min to form a solid coating layer. This coating-drying step was varied to ensure the complete coating without the vacancy (1 time ("M3") or 2-3 times ("M4"), **Table 4.2**). In this method, the pre-filling of the bore side was not necessary since the precursor gel was less likely to fill the bore during the sol coating step. Besides, the gel was coated on the outer surface of the fiber and formed a solid coating. Once the coating step was done, the solid-gel coated hollow fibers were put into the channel of the PTFE holder and this was placed inside the 45 mL Teflon liner. To accelerate the crystallization, 6 mL of 0.2 M TPAOH was injected between the PTFE holder and the Teflon liner. The sealed autoclave

was kept at 458 K for 96 h for the vapor-phase crystallization. Washing and calcination of the membrane were done as same as mentioned earlier.

Table 4.2 Summary of the membrane synthesis conditions

Membrane #	Synthesis method	Synthesis temperature (K)	Synthesis time (h)
M1	Liquid-phase in situ	448	16
M2	Liquid-phase in situ	448	32
M3	Solid-gel vapor-phase in situ (1 time coating)	458	96
M4	Solid-gel vapor-phase in situ (2-3 times coating)	458	96

4.2.4 Characterizations

SEM images of the membranes were collected with a Hitachi SU 8010 scanning electron microscope. Elemental analysis on membrane cross-sections was conducted with a Hitachi SU 8230 scanning electron microscope equipped with an Oxford Instruments X-Max^N Silicon Drift Detector. Powder XRD patterns were taken with a PANalytical X'Pert Pro diffractometer at room temperature using Cu Kα radiation. Grazing-angle XRD patterns were taken with a PANalytical Empyrean at room temperature using Cu Kα radiation. TEM images of the MFI nanocrystals were collected using an FEI Tecnai 30 at an acceleration voltage of 300 kV.

Gas permeation measurements were conducted in Wicke-Kallenbach mode at room temperature. Before permeation measurements, the membrane was kept in the membrane module under argon gas flow for 8 h.

For separation of equimolar butane isomers mixture, the pure *n*-butane and *i*-butane gas cylinders were purchased from Airgas. The 50/50 *n*-butane/*i*-butane gas mixture was obtained by adjusting the flow rate carefully with MFC (Brooks Instrument) and the mixture was well-mixed at a mixer before entering the feed side (shell side) of the membrane module. The total feed flow rate was set to 50 mL/min, while argon (30 mL/min) was used as a sweep gas at the permeate side (bore side).

For separation of 8/8/8/76 *n*-butane/propane/ethane/methane quaternary mixture using 10-membrane module, the 10/90 *n*-butane/methane pre-mixed gas cylinder was purchased from nexAir and the pure propane and ethane gas cylinders were purchased from Airgas. The compositions of gas mixtures were adjusted carefully by MFC (Brooks Instrument) and the mixture was well-mixed at a mixer before entering the feed side of the membrane module. The mixture (total feed flow rate was set to 125 mL/min) was fed to the feed side (shell side) of the membranes at a feed pressure range of 1-9 bar, while argon was set to 500 mL/min by using a flow meter regulator and used as a sweep gas at the permeate side (bore side).

For all cases, permeate side was maintained at atmospheric pressure and feed side pressure was adjusted by using a back-pressure regulator (Cole Parmer, 0-300 psi range). The permeate product was fed to an online gas chromatography unit (GC2014, Shimadzu) to analyze the compositions and the fluxes of each component in the permeate. The data

obtained from GC analysis was used to calculate the permeances of each component (i.e., the flux divided by the partial pressure driving force across the membrane) and the separation factor (i.e., the ratio of the mole fractions of the more permeable gas and the less permeable gas in the permeate divided by the same ratio of mole fractions in the feed).

4.3 Results and Discussion

4.3.1 Liquid-gel based In Situ Method

Figure 4.1 illustrates the fabrication process of the one-step technique for MFI membrane synthesis. The most important step is to prepare a precursor liquid containing concentrated silicate precursors and the SDA, that can be used to form a compact MFI layer with a minimal volume. The precursor liquid also contained 30-50 nm MFI nanocrystals (**Figure 4.2**) to seed the nucleation of the membrane. This liquid was subsequently concentrated into a viscous gel by evaporation of a substantial amount of water content (90 % of the original water content). Then, the bare α-alumina hollow fiber supports were placed in 0.25″ diameter channel drilled into a PTFE holder and the concentrated gel was poured into the holder. The fabrication and characterization of the hollow fiber supports is fully detailed in our previous work [76] and is not described here. This was followed by hydrothermal treatment at 448 K for varied synthesis durations. The composition of the precursor gel and the hydrothermal synthesis conditions were important parameters, that were evaluated and optimized by a number of initial membrane synthesis trials carried out in the channel of the PTFE holder.

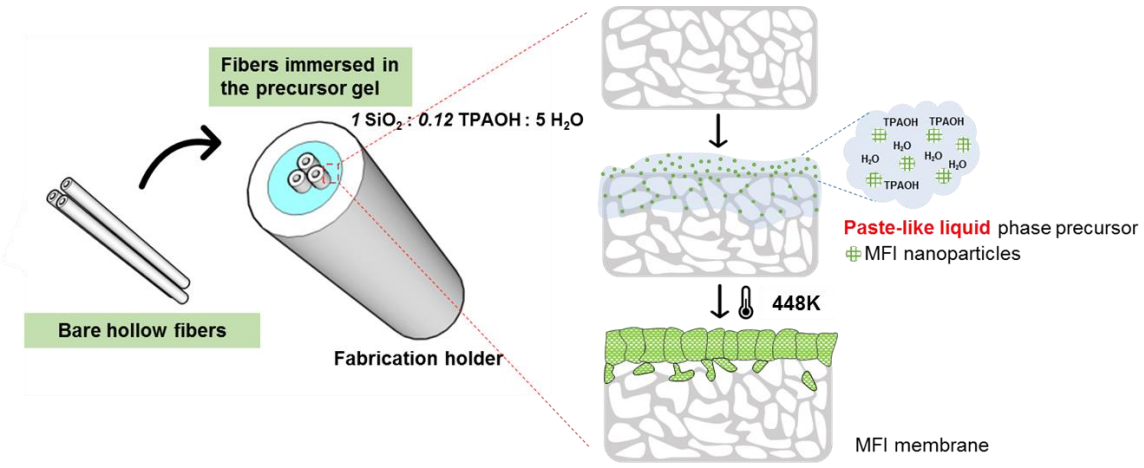

Figure 4.1 Schematic illustration of the one-step in situ membrane synthesis using the highly concentrated liquid gel containing MFI nanocrystals.

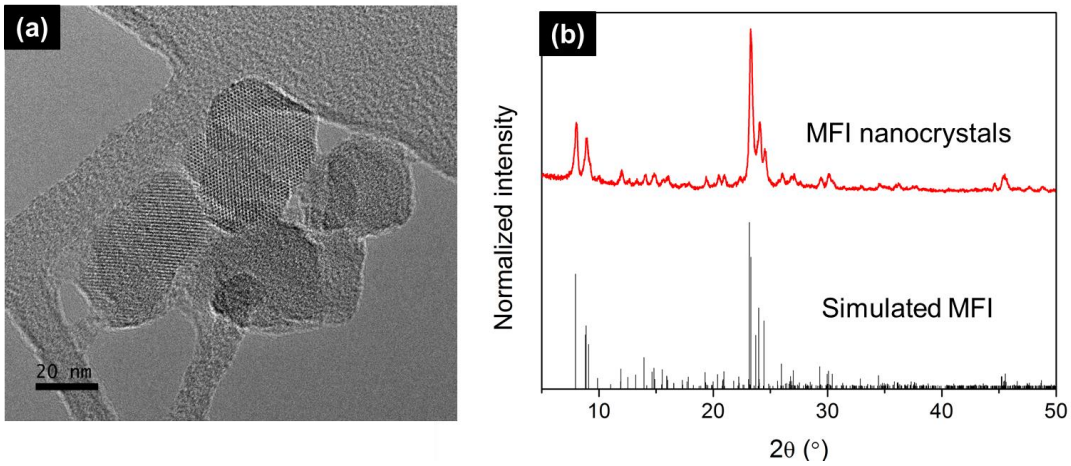

Figure 4.2 (a) TEM image of the MFI nanocrystals and (b) XRD patterns of the MFI nanocrystals with simulated MFI characteristic peaks.

4.3.2 Microstructures of MFI Membranes Prepared by Liquid-gel Conversion

Figure 4.3 presents SEM images of the films grown for different synthesis durations. Presence of an MFI layer on the hollow fiber support was initially confirmed by x-ray diffraction (XRD). The formation of well-intergrown MFI films on the outer surface

of the hollow fiber support is observed at 16 hours (**Figure 4.3(a)**) or more (**Figure 4.3(b)**) of crystallization, suggesting that the highly concentrated precursor gel containing MFI nanocrystals can induce heterogeneous crystallization at the surface of the α-alumina fiber support. The intergrown polycrystalline film appears to have a high density of grain boundaries and small grain sizes (< 300 nm, **Figure 4.4(a)**). This distinctive film morphology suggests that the continuous intergrown film may be formed from primary aggregates of MFI nanoparticles. MFI nanoparticles promote the fast formation of a large number of grains on the support. Subsequently, they interlock into a continuous film. The M1 (16 h) membrane has an apparent thickness of 300-600 nm whereas M2 (32 h) has a range of 500-1200 nm. Prolonged synthesis duration results in an overlayer of larger MFI crystals on the surface of the membrane (**Figure 4.4(b)**). EDX mapping of Si (from zeolite) and Al (from support) content in **Figure 4.3(c)-(d)** shows that the continuous MFI films M1 and M2 are primarily formed on the outer surface of the hollow fiber, but some silica-based material (possibly also MFI) is also detected within the support. The XRD patterns (**Figure 4.3(e)**) of the membranes indicate that the precursor gel was completely converted into an MFI zeolite membrane, due to the absence of broad amorphous silica peaks. It is important to note that the membrane is formed in a single-step crystallization on a low-cost hollow fiber support. Besides, the membrane appears well-intergrown, continuous, and thin (submicron in the case of M2). The conventional in situ methods usually require multiple iterations (**Table 4.1**) to synthesize highly intergrown films due to the low density of nuclei in the original hydrothermal solution or gel.

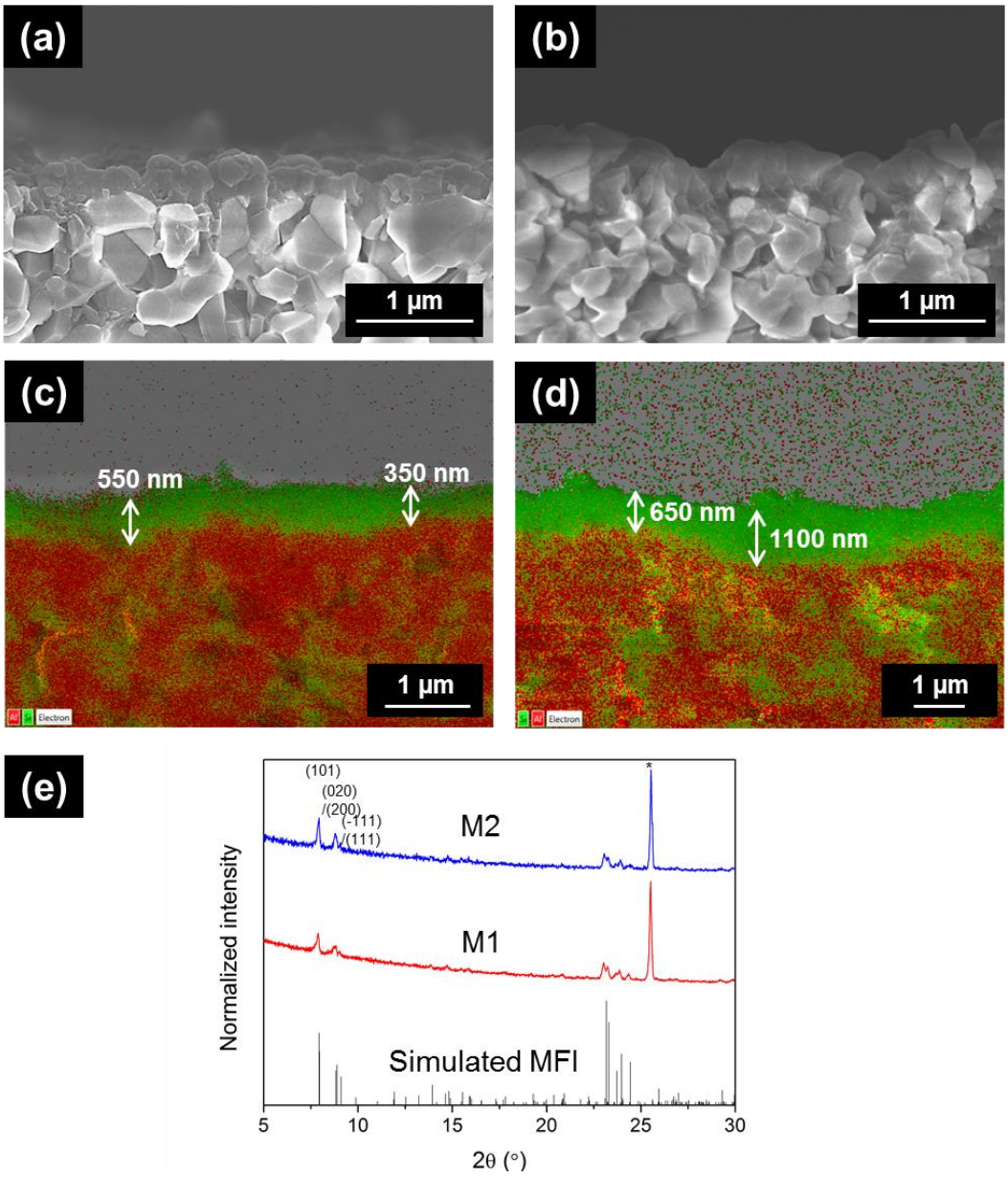

Figure 4.3 SEM images of the MFI membranes grown for (a) 16 h (M1) and for (b) 32 h (M2); the Si (green) and Al (red) element mapping images for the MFI membranes grown for (c) 16 h (M1) and for (d) 32 h (M2); (e) corresponding XRD patterns (* α-alumina support).

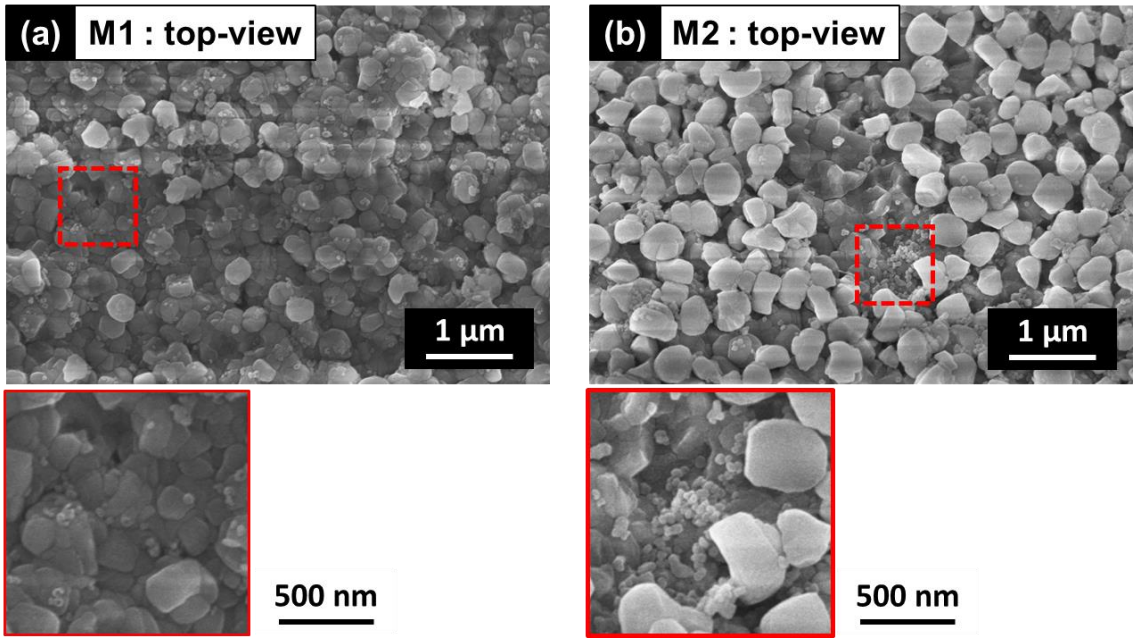

Figure 4.4 SEM images of the surface of the MFI membranes grown for (a) 16 h and for (b) 32 h; and their enlarged images.

4.3.3 Gas Permeation Properties of MFI Membranes Prepared by Liquid-gel Conversion

The separation performance of the MFI membranes synthesized at different durations (M1 and M2) was evaluated by equimolar butane isomers (50/50 *n*-butane/*i*-butane) permeation measurements at room temperature (298 K) in a Wicke-Kallenbach setup. **Figure 4.5(a)** presents the separation performance of 16 membrane samples prepared independently, six of which were grown for 16 hours (M1) and the remaining ten were grown for 32 hours (M2). The numerical data for each sample is shown in **Table 4.3**. The permeances and separation factors shown in **Figure 4.5(a)** are calculated after 8 h of degassing (in argon at 298 K) and 1.5 h of separation measurement, by which time the permeance and separation factor reaches a nominal steady-state (**Figure 4.6(a)**). Clear molecular sieving effects are observed in both M1 and M2 membranes, and considerably

enhanced separation factor is also observed in M2 membranes. The averaged *n*-butane permeance of M1 membranes was obtained as 1000 GPU with a moderate *n*-butane/*i*-butane separation factor of 12. With a longer synthesis time (M2), the averaged *n*-butane permeance decreased to 430 GPU and the separation factor increased to an excellent value of 60 which is one of the highest reported to date (**Table 4.1**). The reduction in the permeance and increase in separation factor observed in M2 membranes is attributed to the increase in the thickness and the lower concentration of defects than the M1 membranes. The difference in the contribution of the transport through the defects can be explained by the pressure dependence of the separation properties. The effect of closing membrane defects can be clearly seen in the pressure dependence of the permeances and separation factors of M1 and M2 membranes (**Figure 4.5(b)-(c)**). In the M1 membrane, the permeance of *n*-butane monotonically drops from 1200 GPU at 1 bar feed pressure to 690 GPU at 2 bar, demonstrating that the major transport path of *n*-butane is through the zeolite MFI pores. On the other hand, the permeance of the less favored species *i*-butane increases from 88 GPU to 110 GPU. This is known to be a characteristic of defective membranes in which Knudsen or viscous transport through the non-zeolitic intercrystalline defects is significant [110]. As a result, the separation factor substantially drops from 12 to 6 with only 1 bar pressure increase. On the other hand, M2 shows a decrease in permeance for both isomers with increasing pressure, and maintenance of a high separation factor. This behavior is highly characteristic of competitive adsorption and permeation of *n*-butane and *i*-butane in zeolite pores and the negligible influence of defects [73]. I operated one of the M2 membranes for up to 36 h on-stream (**Figure 4.6(b)**) and observed a small decrease of the permeances of both *n*-butane (16 %) and *i*-butane (12 %). Despite this reduction, *n*-butane

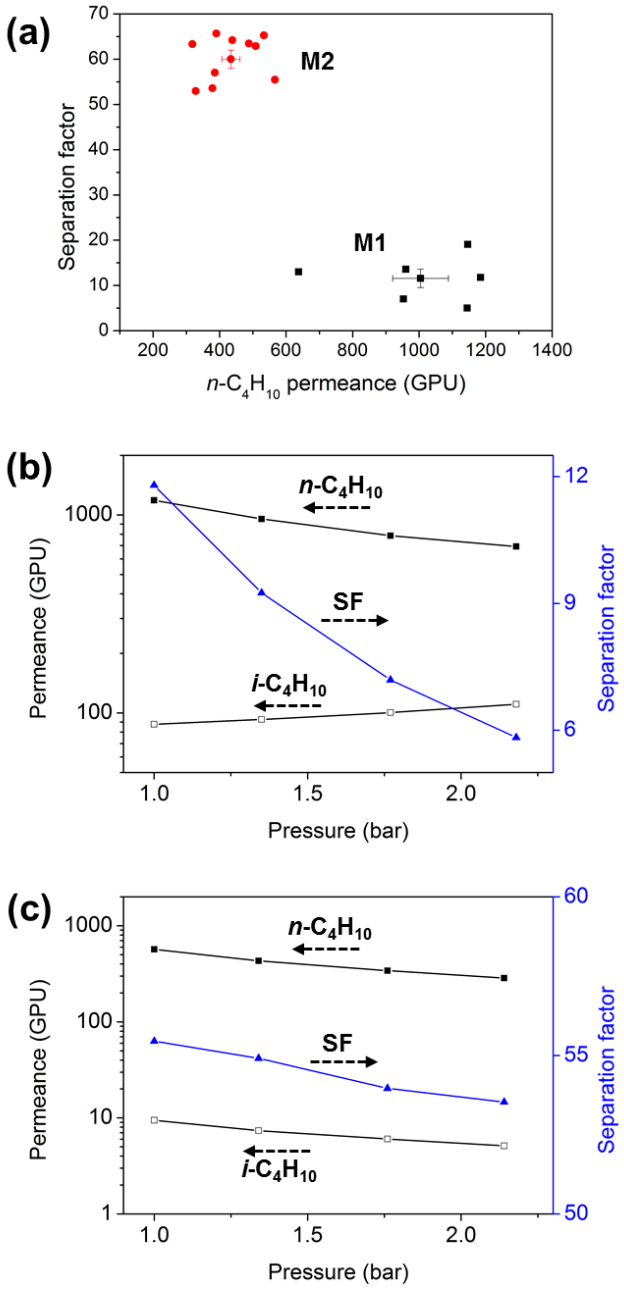

Figure 4.5 (a) Equimolar *n*-butane/*i*-butane mixture separation performance of MFI membranes (M1, M2) at 298 K; and pressure dependence of separation performances observed from (b) M1 and (c) M2 (All permeation results were collected after 1.5 h operation and results were available in **Table 4.3**)

permeance is still as high as 320 GPU and it maintains nearly constant and high separation factor of 55. This result from longer measurements might be due to the presence of small concentrations of higher alkane impurities in the feed, or slight blocking of the MFI pores by small quantities of high-molecular weight organics desorbing slowly from the epoxy that was used to mount the hollow fibers in the permeation module, as reported in our previous work [74-76].

Table 4.3 Equimolar butane isomers separation results measured at 298 K obtained from the membranes grown for 16 h (M1), 32 h (M2) and M2 10-membrane module (1 gas permeation unit (GPU)=3.348×10^{-10} $mol.m^{-2}.s^{-1}.Pa^{-1}$)

	Membrane sample	Permeance [GPU]		*n*-butane/*i*-butane Separation factor
		***n*-butane**	***i*-butane**	
A.	Membranes grown for 16 h (M1)-1	953	127	7
	M1-2	1145	85	5
	M1-3	638	43	13
	M1-4	1146	52	19
	M1-5	960	63	14
	M1-6	1185	88	12
	Average	1004 ± 84	76 ± 12	12 ± 2
B.	Membranes grown for 32 h (M2)-1	391	6	66
	M2-2	318	5	63
	M2-3	378	7	54
	M2-4	438	6	64
	M2-5	533	8	65
	M2-6	488	7	63
	M2-7	509	8	63
	M2-8	567	9	55
	M2-9	328	6	53
	M2-10	386	6	57
	Average	434 ± 27	7 ± 0.4	60 ± 2
C.	10-membrane module*	278	5	53

*Total feed flow rate was increased to 76 mL/min, sweep gas flow rate was increased to 60 mL/min

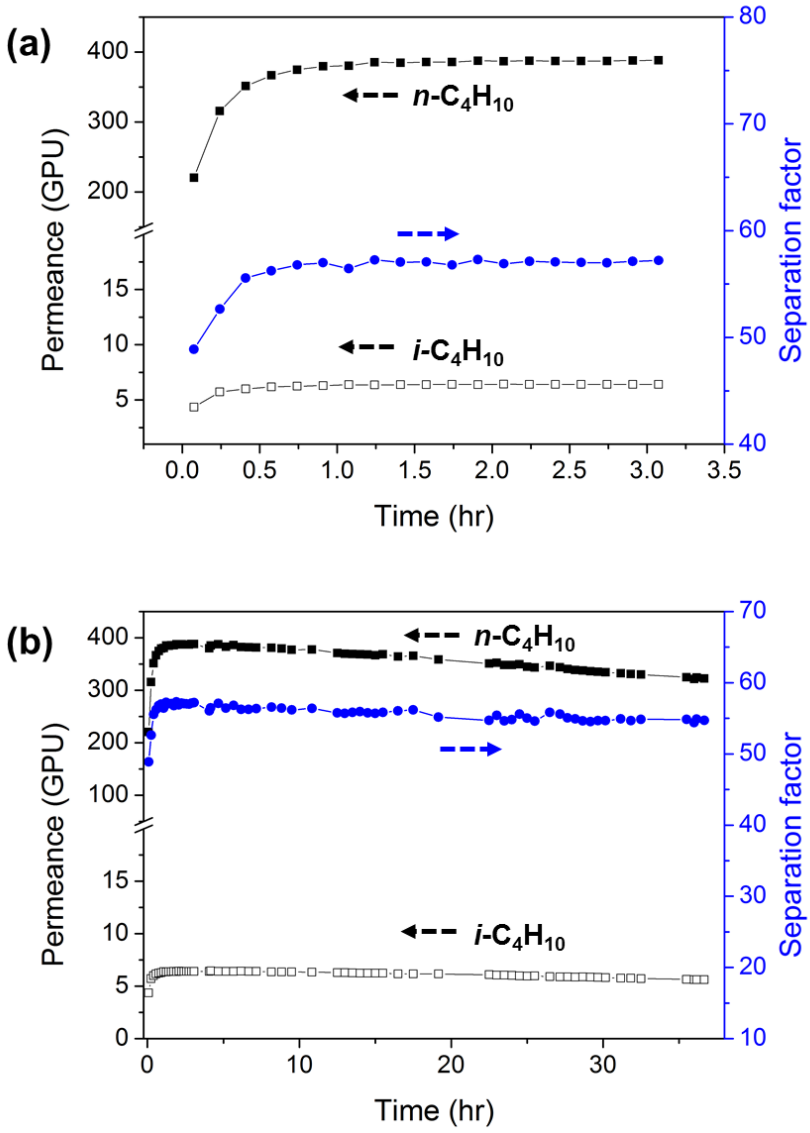

Figure 4.6 On-stream *n*-butane/*i*-butane separation performance of a membrane (M2-10) (a) measurement up to 3 h, and (b) measurement up to 36 h

According to the comparison shown in **Figure 4.7**, the MFI membranes prepared from our single-step method outperform previous MFI membranes prepared by conventional in situ growth methods [41, 78, 79, 81, 82, 86-89, 120, 124-130], conventional seeded growth methods [23, 37, 73, 80, 83-85], and other types of membranes

(polymeric [90], MFI mixed matrix [90], ZIF [91]) with regard to butane isomers separation. The observed performance is also comparable to that of MFI membranes prepared from 2D MFI nanosheets [29, 35, 65, 76]. In addition to this, our method has been developed with high reproducibility on 750 µm diameter α-alumina hollow fiber supports that do not have any specially engineered surface characteristics or microstructures. So far, most reports on in situ MFI membranes were limited to small flat disks (2 cm^2), large-diameter (10 mm) OD tubes, or surface-modified tubes/hollow fibers of large diameters (1.7-3.5 mm, **Table 4.1**).

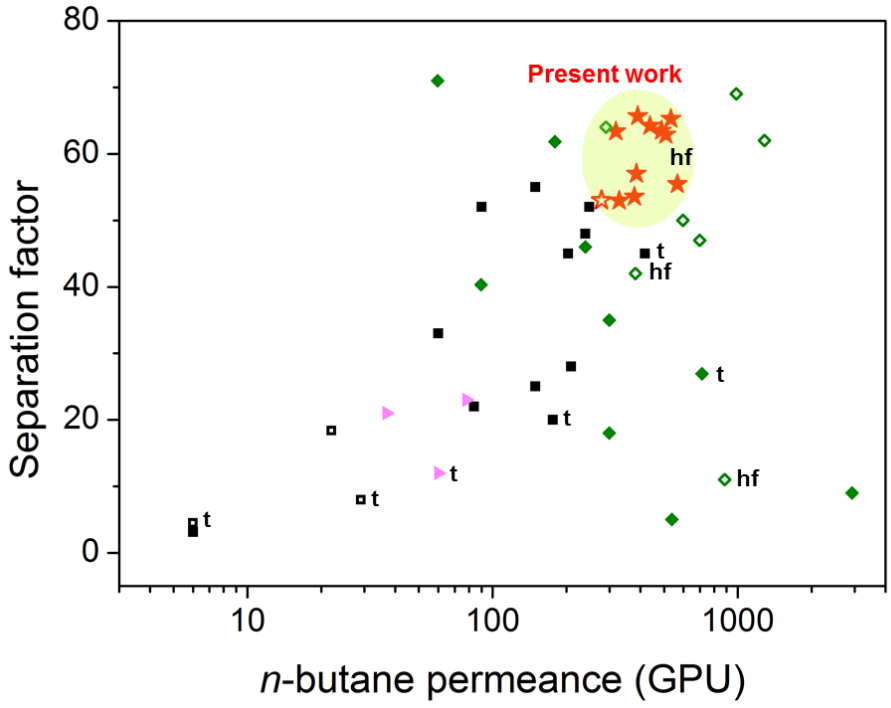

Figure 4.7 Comparison of the butane isomers separation performance of our MFI membranes with those of other membranes in the previous literatures (Triangle: ZIF-90, MFI mixed-matrix membrane, Polymer membranes; filled rectangle: MFI membranes by multiple in situ; unfilled rectangle: MFI membranes by single in situ; filled diamond: MFI membranes by seed-based secondary growth; unfilled diamond: MFI membranes by 2D MFI seed-based secondary growth; filled star symbol: present work; open star symbol: 10-membrane module from present work; t: membrane supported on the tubular support, hf: membrane supported on the hollow fiber support), all others on disk supports. (data from in situ method are available in **Table 4.1 and 4.3**)

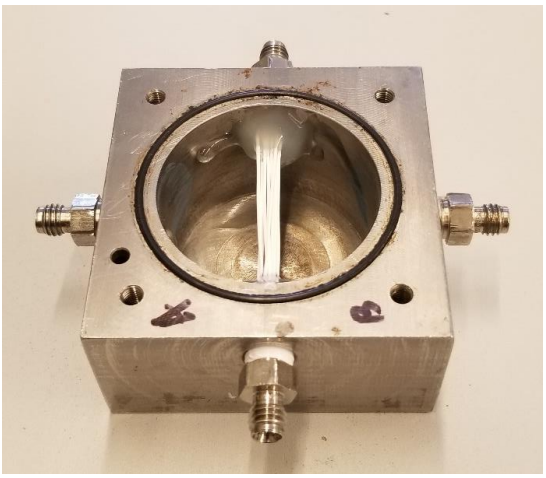

Figure 4.8 M2 10-membrane module for the gas mixture permeation tests

To demonstrate the scalability of our method, another 10 hollow fiber membranes were synthesized simultaneously (this time in a single synthesis run) using our PTFE holder. 10 hollow fibers were put into the same 0.25" channel PTFE holder and the synthesis gel was poured into the holder. The use of the same size channel and the same quantity of synthesis gel for both 3 membranes synthesis (for single membrane test) and 10 membranes synthesis imply remarkably efficient utilization of the reactant. The 10-membrane module (assembled by potting these membranes in epoxy) is shown in **Figure 4.8**, and was evaluated by separating an equimolar binary mixture of butane isomers. High *n*-butane permeance of 280 GPU and *n*-butane/*i*-butane separation factor of 53 are seen in **Figure 4.7** (open star symbol) and **Table 4.3**, and are comparable to the results from single-membrane samples (filled star symbols). However, the *n*-butane permeance is observed to be the lowest of all our hollow fiber membranes (star symbols) in **Figure 4.7**. Then, I extended the investigation of this 10-membrane module to the separation of natural gas liquid (NGL) components (*n*-butane, propane, and ethane) from methane. Removal of such higher hydrocarbons from methane is currently performed by energy-intensive cryogenic distillation, and cannot easily be addressed by conventional polymer membranes. I

evaluated the gas permeation properties of a quaternary gas mixture containing 8/8/8/76 *n*-butane/propane/ethane/methane as a function of feed pressure (**Figure 4.9**). The membrane was strongly selective towards higher hydrocarbons. At 9 bar, the membrane exhibits a high *n*-butane/methane separation factor of 97 with high *n*-butane permeance of 460 GPU. For propane, the permeance is 220 GPU with a propane/methane separation factor of 48. For ethane, the permeance of 31 GPU with an ethane/methane separation factor of 7 is observed. This selective permeation of higher hydrocarbons over methane is clearly attributed to their strong adsorption. Consequently, the order of the selectivity follows the order of heats of adsorption which increases with the carbon number [131].

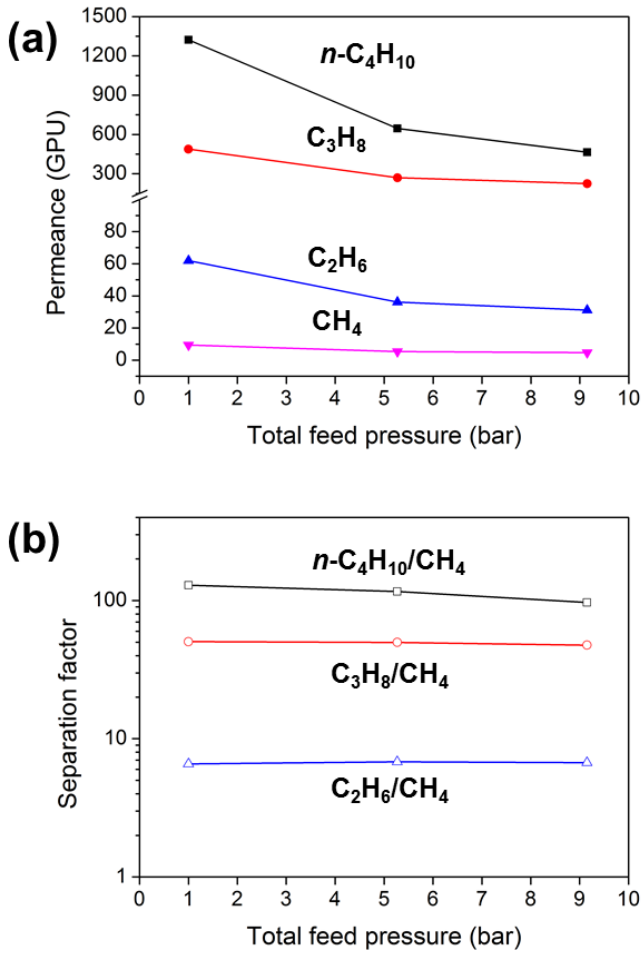

Figure 4.9 (a) Permeance and (b) separation factor observed for separation of *n*-$C_4H_{10}/C_3H_8/C_2H_6/CH_4$ (8/8/8/76) quaternary mixture by the 10-membrane module as a function of total feed pressure

These quaternary mixture separation permeation results at 9 bar were then compared with what was observed from the single-fiber membrane (M2-10), randomly chosen from the 10 M2 samples available (**Table 4.3**). As in the case of binary butane isomers separation, the *n*-butane permeance of the 10-membrane module in quaternary hydrocarbon separation is significantly lower than that of M2-10. Interestingly, all the separation factors are quite comparable, and the permeances of propane and ethane are also quite comparable in the two cases. Thus, it is suspected that the differences observed are not indicative of lower quality of the 10-membrane module, but related to operational factors that most strongly affect *n*-butane (the strongest-adsorbed component). The sweep flow rates in the two cases (**Table 4.4**) are selected such that each fiber bore carries roughly the same (50-60 mL/min) sweep flow rate. As a result, desorption of *n*-butane on the permeate side is not significantly different in the two cases and is not expected to limit the permeance in the 10-membrane module. On the other hand, our feed side mass flow controller is limited to 125 mL/min. Hence, I expect substantially more concentration polarization in the 10-membrane module because the high *n*-butane flow through 10 membranes strongly depletes the *n*-butane and increases the concentration of the other permeating species at the membrane surface as compared to the that in the bulk feed stream, thereby decreasing the actual transmembrane driving force for *n*-butane and thus decreasing its apparent permeance (which is obtained by division of the flux by the apparent driving force based on the inlet bulk feed and outlet permeate compositions) [21, 132]. Therefore, I expect that optimization of the operation conditions - using an appropriate flow controller that can provide higher feed flow rates - would lead to the same *n*-butane performance of the 10-membrane module and single-fiber membranes. The

observed high separation performance at high pressure (9 bar) in a 10-membrane module demonstrates its scalable, compact and low-cost separation membrane system for the industrially important application.

Table 4.4 Separation performances observed from single membrane (M2-10: randomly chosen) and 10-membrane module at P_{feed} = 9 bar (1 gas permeation unit (GPU)=3.348×10^{-10} $mol.m^{-2}.s^{-1}.Pa^{-1}$)

Membrane sample	Permeance (GPU)				Separation factor		
	***n*-butane**	**propane**	**ethane**	**methane**	***n*-butane/methane**	**propane/methane**	**ethane/methane**
M2-10*	878	244	37	6	132	41	6
10-membrane module**	464	224	31	5	97	48	7

*125 mL/min total feed flow rate, 60 mL/min sweep gas flow rate, **125 mL/min total feed flow rate, 500 mL/min sweep gas flow rate

4.3.4 Solid-gel Vapor-phase based In Situ Method

As an additional variation of this one-step in situ method, I investigated the vapor-phase crystallization approach. For a large-scale synthesis of zeolite membranes, vapor-phase synthesis offers additional advantages over the liquid-phase hydrothermal synthesis. The main advantages of vapor-phase synthesis are (1) controllable precursor coating regardless of the geometry of the support, (2) reduction in the use of pricey reactants, (3) reusable precursor gel, and (4) easy washing step with the reduced wastes [42, 79].

To be able to fabricate the uniform MFI zeolite membrane film on supports with arbitrary geometry via vapor-phase crystallization, the formation of the uniform solid-gel layer is essential. However, the solid-gel vapor-phase crystallization method still requires multiple steps including support modifications and multiple hydrothermal reactions and it has not been successfully transferred to the inexpensive hollow fiber support yet. This

might be attributed to the limited mobility of the precursor species in a solid gel, thereby resulting in much higher activation energy for the crystallization (80 kJ/mol) compared to the aqueous phase precursor (40 kJ/mol) [42].

Here, I extended our method to the solid-gel vapor-phase crystallization method for the synthesis of MFI hollow fiber membranes. The major differences between liquid-phase and solid-gel vapor-phase crystallization methods are as follows (1) formation of the uniform solid-gel layer, (2) TPAOH-H_2O vapor-phase treatments without direct contact with liquid-phase gel and (3) synthesis at a higher temperature for a longer synthesis time.

In the first step, the hollow fiber support was dip-coated with the liquid precursor gel and left for 3 min for uniform coating. The gel-coated fiber was then dried in a convection oven at 333 K. This coating step was repeated 2 ~ 3 times to ensure uniformity. This initial solid gel layer which contains a highly concentrated structure-directing agent, amorphous silica source, and MFI nanocrystals not only allows relatively efficient reconstruction of the original amorphous SiO_2 network into the crystallized zeolite layer but also helps the continuity and compactness of the final MFI layer. As noted earlier, in the case of crystallization of the precursor species in a solid gel, crystallization is kinetically restricted due to the high activation energy. Therefore, a higher synthesis temperature (448 K → 458 K) and a longer synthesis time (32 h → 96 h) conditions were chosen to promote the crystallization and demonstrate the possibility of the concept.

In the process of MFI crystallization, the solid gel layer is transformed to the MFI membrane by the interaction of the TPAOH-H_2O vapor with the SiO_2-based solid gel during the heat treatment.

4.3.5 Microstructures of MFI Membranes Prepared by Solid-gel Conversion

Figure 4.10(a)-(b) presents SEM images of the solid gel coating and the film obtained after the vapor-phase crystallization. The solid-gel deposited on the support is very dense and uniform. The cross-section SEM images show that solid gel is infiltrated within the support layer which can enhance the adhesion of the precursor gel and the support. After the crystallization, a continuous zeolite film is formed on the support with some crystal embedded within the support layer as similar to the liquid-phase crystallization method. The thickness of the dense membrane layer formed on top of the support is 500 - 1000 nm. On the surface of the dense layer, aggregations of nanosized particles are present which might be attributed to the initial MFI nanocrystals embedded in the thick solid-gel layer that didn't grow into the continuous film. This non-continuous nanoparticle layer is expected to not contribute to the transport of gas transport. EDS mapping analysis (**Figure 4.10(c)**) indicates the location of the newly formed SiO_2-based zeolite layer on top of the Al support. However, due to the aggregated MFI nanocrystals present on the zeolite film, it was difficult to determine the effective thickness of the membrane from the EDS analysis.

The XRD pattern of the initial solid-gel layer before the vapor-phase crystallization verify that MFI nanoparticles and amorphous silica network are present (**Figure 4.10(d)**). The XRD analysis after the vapor-phase crystallization demonstrates the amorphous silica phase disappears and strong MFI characteristics peaks are evolved, indicating the solid-gel has been transformed to MFI crystalline phase. Due to its simplicity of the coating step, the solid precursor gel is expected to be potentially formed on the substrates of any geometries.

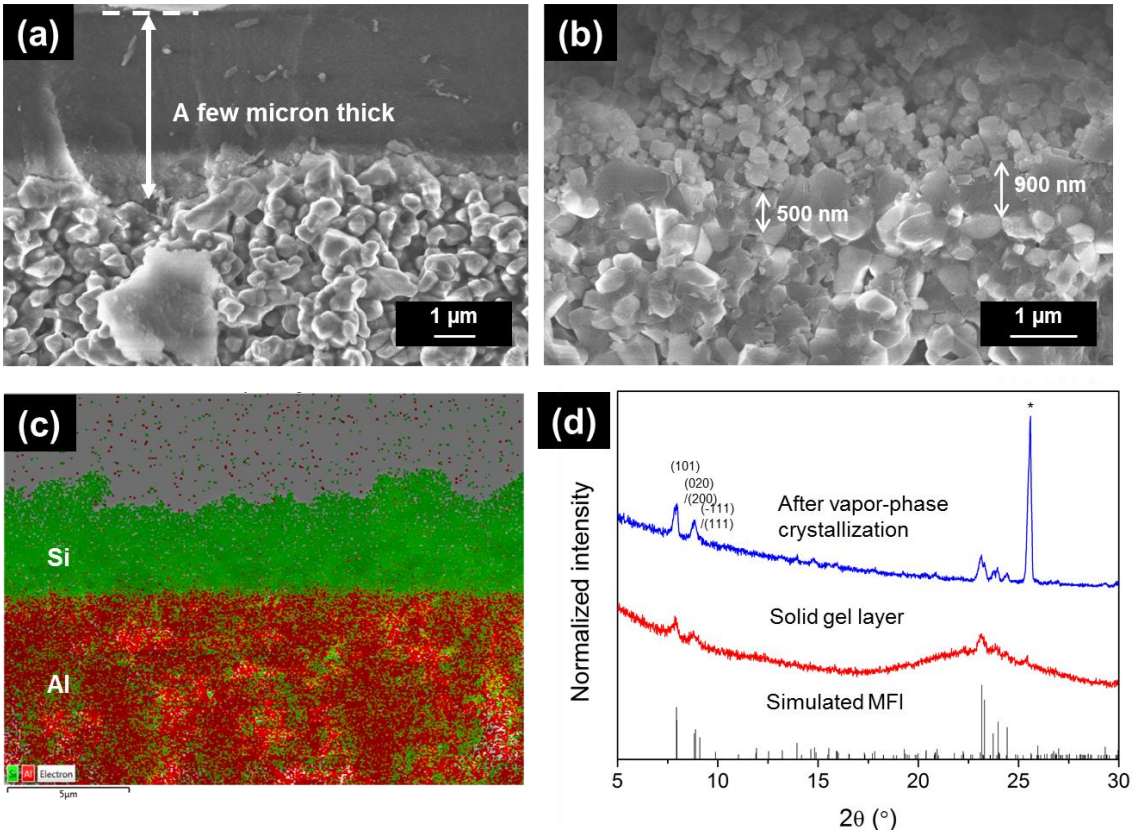

Figure 4.10 SEM images of (a) the solidified gel, and (b) the MFI membrane grown by vapor-phase crystallization; (c) the Si (green) and Al (red) element mapping image of the MFI membrane; (d) XRD patterns corresponding to the solidified gel before/after vapor-phase crystallization

4.3.6 Gas Permeation Properties of MFI Membranes Prepared by Solid-gel Conversion

Next, I investigated the butane isomers molecular sieving properties of the membrane prepared by the solid-gel vapor-phase crystallization. The solid-gel layer before the crystallization was tested as a baseline and the membranes prepared by varying the number of gel coating times (M3, M4) were evaluated. Total 13 membrane samples prepared independently, one of which was the solid-gel layer before the crystallization, three of which were membranes crystallized after 1-time gel coating (M3), and the

remaining nine were crystallized after 2-3 times gel coating (M4). The numerical data for each sample is shown in **Table 4.5**.

While the initial solid-gel layer shows very low permeance and no selectivity, progressive improvements in the molecular sieving properties are observed after the vapor-phase crystallization. For consistency, permeation data are collected after 1.5 h of post-degassing measurement (**Figure 4.12(a)**). M3 Membranes crystallized after a one-time coating of the precursor gel started to show a separation factor (~ 2) with high permeance of *n*-butane (890 GPU). Then, the M4 membranes prepared by 2-3 times coating results in a significantly increased separation factor of 37 and the reduced permeance of *n*-butane (450 GPU), indicating the minimized defects sites. However, the permeance continuously decreases as the measurement time increases whereas membrane grown in a liquid-gel (M2) very quickly reaches a nominal steady-state (**Figure 4.6**). One of the M4 membranes (M4-3) was tested for 65 h of on-stream operation and consequently results in the decrease in the permeance of *n*-butane (315 GPU → 81 GPU) and *i*-butane (5.6 GPU → 1.6 GPU), 74 % and 71 % reduction in the permeance respectively. The separation factor is nearly constant as 50. The decrease in the permeance might be caused by the micropore channel clogging with *i*-butane and small concentrations of impurity hydrocarbons in the feed stream [74-76]. While liquid-gel based M2 membrane shows a 16 % reduction in 36 h of operation, the M4 membrane shows a 66 % reduction in the same period of the operation time. Much more significant reduction of permeance and such a long transient state observed from the membrane grown in a vapor-phase crystallization (M4) is still questionable. It can be hypothesized that local structural differences (such as degree of

crystallization) between the liquid-based and vapor-based membranes can play a major role in these different permeation behaviors.

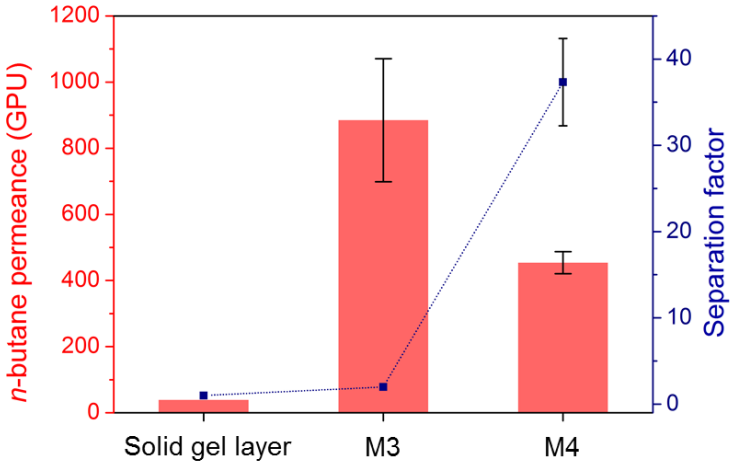

Figure 4.11 Equimolar *n*-butane/*i*-butane mixture separation performance of the solid gel layer before the crystallization and MFI membranes (M3 and M4) (Crystallization condition is identical for all samples, all permeation results were collected after 1.5 h operation)

Table 4.5 Equimolar butane isomers separation results measured at 298 K obtained from the solid gel layer, membranes grown after 1 time gel coating (M3), 2-3 times gel coating (M4) (1 gas permeation unit (GPU)=3.348×10^{-10} mol.m^{-2}.s^{-1}.Pa^{-1})

Membrane sample	Permeance [GPU]		*n*-butane/*i*-butane Separation factor
	n-butane	*i*-butane	
A. Solid gel layer	39	39	1
B. Membranes grown after 1 time gel coating, M3-1	1075	504	2
M3-2	1066	596	2
M3-3	514	298	2
Average	885 ± 186	466 ± 88	2 ±0
C. Membranes grown after 2-3 times gel coating, M4-1	331	5	58
M4-2	476	9	52
M4-3	315	6	53
M4-4	489	13	34
M4-5	596	28	20
M4-6	361	9	36
M4-7	458	16	28
M4-8	496	11	41
M4-9	566	37	14
Average	454 ± 33	15 ± 4	39 ± 5

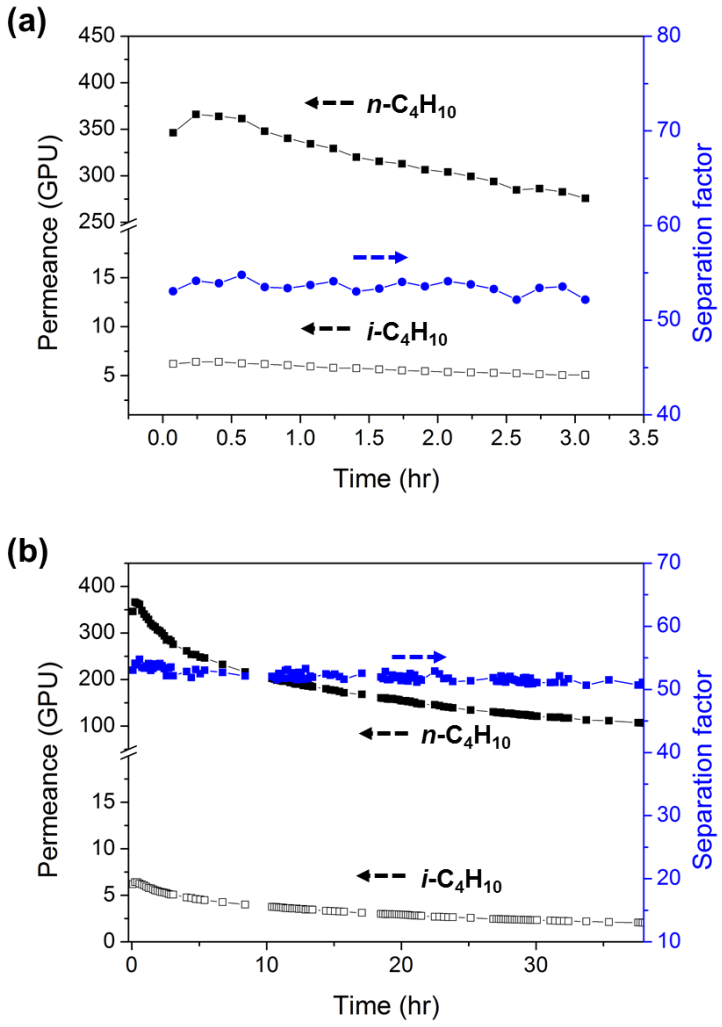

Figure 4.12 On-stream *n*-butane/*i*-butane separation performance of a membrane (M4-3) (a) measurement up to 3 h, and (b) measurement up to 36 h

The present permeation results clearly indicate a non-selective low permeable amorphous SiO_2 layer is transformed to a selective highly permeable membrane. Also, progressive improvements in molecular sieving properties observed for the membranes prepared from 1 time gel coating and the 2-3 times repeated gel coating suggest that repeated gel coating step would be necessary to ensure the uniformity of the gel and provide sufficient source for the formation of the continuous membrane. These observations clearly support that further optimizations of the solid-gel vapor-phase crystallization method

would eventually enable the economic and environment-friendly preparation of high-quality MFI membranes on various types of support.

4.4 Conclusion

In conclusion, I have successfully demonstrated a facile and scalable fabrication method to directly grow highly selective and thin MFI membranes on a low-cost ceramic hollow fiber support in a one-step crystallization. Highly concentrated precursor gel containing MFI nanocrystals is expected to induce a fast formation of a high density of nuclei and promote compact heterogeneous crystallization in the vicinity of the support. This synthesis strategy doesn't require a separate seeding step and the use of specialty engineered supports, thereby this can greatly simplify the fabrication steps and reduce the production cost. The MFI membranes were identified as substantially thin (~ 1 μm) and high-quality, therefore they are highly permeable and highly selective for the separation of butane isomers mixture. The scalability of this fabrication method is demonstrated by synthesizing the 10 membranes in a single batch. The 10-membrane module shows comparably high separation performances for the butane isomers separation and its application was extended to the removal of higher hydrocarbons (*n*-butane, propane, and ethane) from methane. Furthermore, I demonstrated that MFI membranes can be synthesized via a solid-gel vapor-phase crystallization method. The present methods offer alternatives for scalable and reliable production of high-quality but low-cost MFI membranes by eliminating the complex fabrication steps such as seeding step, multiple crystallizations, and engineering of the supports.

CHAPTER 5. CONCLUSIONS AND FUTURE WORK

5.1 Main Findings

The work presented in this thesis has made significant progress towards the overall research goal of developing zeolite membrane fabrication strategies and understanding hydrocarbon permeation properties to enable the technological implementation of thin and highly selective MFI zeolite membranes.

In chapter 2, a scalable fabrication methodology for the preparation of the highly *b*-oriented and thin MFI membranes on low-cost ceramic hollow fiber supports was presented. Using 2D MFI nanosheets, a continuous coating of *b*-oriented 2D MFI nanosheets was obtained on the outer surface of the hollow fiber via vacuum filtration. A key finding is that sequential secondary and tertiary hydrothermal treatments with the TPA-fluoride and TEA-containing solutions are effective in closing macroscopic voids and nanoscopic defects, respectively, while preserving the (0*k*0) out-of-pore orientation and thin thickness (< 1 μm). As a result, the membranes after tertiary growth exhibit excellent molecular sieving properties for butane isomers. The membrane fabrication approach employing 2D zeolite nanosheets and low-cost macroporous hollow fiber support reported here allows appropriate membrane microstructures for excellent molecular sieving properties and a compact and low-cost separation system. This is a significant step toward the scale-up of the zeolite membranes.

In chapter 3, I further evaluated the separation performances of these 2D MFI-based membranes for wet shale gas processing, with a particular focus on the removal of NGL

components (*n*-butane, propane, ethane) from methane at elevated feed pressures (1 – 10 bar). In the quaternary mixture system, the membrane shows the remarkable inversion of selectivity relative to unary permeation due to the adsorption dominated separation. It is highly selective towards highly adsorbing species such as *n*-butane and propane (e.g., *n*-butane/methane and propane/methane separation factor of 280-170 and 60-40, respectively). It also shows significant separation factors for different pairs of hydrocarbons over the entire pressure range. These results imply that the present 2D MFI membranes can potentially be used in multistage separations to replace/supplement the current multistage distillation and fractionate the streams with all four hydrocarbons. Furthermore, the Maxwell-Stefan (M-S) model integrated with the cross-flow model was developed for the prediction of multicomponent permeation behaviors in the present membranes. M-S predictions show the excellent qualitative correspondence with the experimental results, thereby a number of different aspects of multicomponent separations (such as feed compositions, feed pressures, and sweep gas effect) can be predicted without extensive experimentation. These experimental and simulation results provide important implications for evaluating the performance and economic viability of 2D MFI hollow membranes in actual shale gas processing.

In chapter 4, I developed a further simplified membrane synthesis strategy, i.e. one-step in situ crystallization method. The key features of this strategy are: (1) it does not require a separate nanoparticle seeding or nanosheet coating step, (2) one-time crystallization step ensures high-quality membranes and (3) scalability and reliability. The use of highly concentrated precursor gels containing the MFI nanocrystals allows a fast formation of a high density of nuclei. As a result, this method produces compact and thin

MFI membranes on low-cost macroporous hollow fiber supports in a one-step crystallization and the membranes show excellent molecular sieving properties. Furthermore, the simultaneous synthesis of multiple membranes (10 ea) and high separation performances (butane isomers and removal of NGL components from methane) observed from the 10-membrane module demonstrate scalability and reliability of the present fabrication process. Along with the liquid-gel crystallization method, I also demonstrated that high-quality MFI membranes can be synthesized via a solid-gel vapor-phase crystallization method that offers additional advantages such as controllable coating process and minimal usage of the precursor gel. These gel-based in situ membrane fabrication approaches will further minimize the complexity of the fabrication process and reduce the membrane production costs for the successful implementation of the compact zeolite membrane system in the industrial process.

5.2 Future Work and Challenges

5.2.1 Scale-up of MFI Membranes by Adopting Microwave Heating and UV Treatment Processes

This work has made considerable advances that have removed (or lowered) several significant engineering barriers in achieving reliable scaling of zeolite MFI membrane fabrication processes. There are still some hurdles and inefficiencies that will have an impact on large-scale membrane production: (1) the time-consuming (order of hours) process for membrane growth, (2) possibility of non-uniform membrane growth due to thermal/density gradients during the conventional heating, and (3) necessity of high-

temperature calcination for organic SDA removal. To address these challenges, future works, could focus on combining the methodologies developed in this thesis with microwave heating for the membrane growth, as well as ultraviolet (UV) treatment for non-thermal SDA extraction. Microwave heating reduces not only the membrane growth time to a few hours but also eliminates thermal/density gradients by supplying the energy with an electric field directly to the materials [133]. In large-scale production of the membrane, local differences in the temperature and the density during the synthesis can deteriorate the uniformity of the membrane and reproducibility. Along with this, the conventional heating process for SDA extraction can be replaced with UV treatment. Dr. Shaowei Yang in the Nair group has demonstrated that UV treatment is effective for SDA decomposition and removal from CHA zeolite membranes [134], and a demonstration also exists for MFI membranes [35]. Combining our synthesis methodologies with fast and energy-saving membrane growth and SDA removal processes would further enable a continuous manufacturing process and fabrication of bundles of long fiber membranes for future industrial applications.

5.2.2 Membrane Synthesis without Hydrothermal Reaction

It is highly desirable to eliminate the hydrothermal growth step for the scale-up of the membrane production and continuous manufacturing process. So far, the synthesis of selective MFI membranes without hydrothermal reaction has been limited to a few works. Choi. et. al reported MCM-22 (MWW framework, disk-like crystal shape)/silica selective flake nanocomposite membranes by layer-by-layer deposition of thin MCM-22 and

mesoporous silica [135]. Recently, Zhang. et. al reported the non-hydrothermal fabrication method which involves the exfoliation of the multilamellar MFI by melt compounding, SDA removal by acid treatment, and deposition of the exfoliated 2D MFI nanosheets on polymer support [33]. Despite relatively lower separation performances observed in both works, these works successfully provide clear evidence that highly selective zeolite membranes via non-hydrothermal treatment can be potentially obtained with the use of high-aspect-ratio zeolite.

As noted earlier, 2D MFI nanosheets from bottom-up synthesis have advantages such as high yield production and μm-scale lateral dimension, thereby they would have merits to form more high-quality zeolite coatings and highly selective membranes without the need of multiple fabrication steps. However, these 2D MFI nanosheets have non-uniform thickness due to the presence of the seed at the center of the nanosheets, therefore the stacking of the nanosheets tends to have interparticle voids in scale from dozens of nanometers to hundreds of nanometers and the contribution from non-selective transport prevails. To enable such an improved 2D MFI-based membrane via non-hydrothermal treatment, further developments should be directed to the optimization of packing of the zeolite nanosheets by seed removal from the nanosheets or synthesizing the 2D zeolite nanosheets with the uniform thickness. Furthermore, the systematic variation of the gap-filling materials (such as microporous silica materials or highly permeable polymers) is required to seal the non-selective interparticle gaps and to obtain a separation performance enhancement by employing the right combination of membrane materials.

REFERENCES

1. Sholl, D.S. and R.P. Lively, *Seven chemical separations to change the world.* Nature, 2016. **532**(7600): p. 435-437.

2. Davis, M.E. and R.F. Lobo, *Zeolite and Molecular-Sieve Synthesis.* Chemistry of Materials, 1992. **4**(4): p. 756-768.

3. Xomeritakis, G., Z.P. Lai, and M. Tsapatsis, *Separation of xylene isomer vapors with oriented MFI membranes made by seeded growth.* Industrial & Engineering Chemistry Research, 2001. **40**(2): p. 544-552.

4. Yuan, W.H., Y.S. Lin, and W.S. Yang, *Molecular sieving MFI-type zeolite membranes for pervaporation separation of xylene isomers.* Journal of the American Chemical Society, 2004. **126**(15): p. 4776-4777.

5. Matsufuji, T., et al., *Separation of butane and xylene isomers with MFI-type zeolitic membrane synthesized by a vapor-phase transport method.* Journal of Membrane Science, 2000. **178**(1-2): p. 25-34.

6. Bernal, M.P., G. Xomeritakis, and M. Tsapatsis, *Tubular MFI zeolite membranes made by secondary (seeded) growth.* Catalysis Today, 2001. **67**(1-3): p. 101-107.

7. Yu, L., M. Grahn, and J. Hedlund, *Ultra-thin MFI membranes for removal of C3+ hydrocarbons from methane.* Journal of Membrane Science, 2018. **551**: p. 254-260.

8. *Materials Research for Separations Technologies: Energy and Emission Reduction Opportunities*. 2005, BCS Incorporated, Oak Ridge National Laboratory.

9. Zhang, K., et al., *Adsorption of Water and Ethanol in MFI-Type Zeolites.* Langmuir, 2012. **28**(23): p. 8664-8673.

10. Korde, A., et al., *Effect of Si/Al Ratio on the Catalytic Activity of Two-Dimensional MFI Nanosheets in Aromatic Alkylation and Alcohol Etherification.* Chemcatchem, 2019. **11**(18): p. 4548-4557.

11. Beving, D.E., et al., *Corrosion resistant high-silica-zeolite MFI coating - One general solution formulation for aluminum alloy AA-2024-T3, AA-5052-H32, AA-6061-T4, and AA-7075-T6.* Journal of the Electrochemical Society, 2006. **153**(8): p. B325-B329.

12. Li, Z.J., et al., *Mechanical and dielectric properties of pure-silica-zeolite low-k materials.* Angewandte Chemie-International Edition, 2006. **45**(38): p. 6329-6332.

13. Shu, X.J., et al., *High-Flux MFI Zeolite Membrane Supported on YSZ Hollow Fiber for Separation of Ethanol/Water.* Industrial & Engineering Chemistry Research, 2012. **51**(37): p. 12073-12080.

14. Bernal, M.P., et al., *Separation of CO2/N-2 mixtures using MFI-type zeolite membranes.* Aiche Journal, 2004. **50**(1): p. 127-135.

15. Sebastian, V., et al., *Zeolite membrane for CO2 removal: operating at high pressure.* Desalination, 2006. **199**(1-3): p. 464-465.

16. Korelskiy, D., et al., *Efficient ceramic zeolite membranes for CO2/H-2 separation.* Journal of Materials Chemistry A, 2015. **3**(23): p. 12500-12506.

17. Li, S.G., J.L. Falconer, and R.D. Noble, *SAPO-34 membranes for CO2/CH4 separation.* Journal of Membrane Science, 2004. **241**(1): p. 121-135.

18. Wang, Z.B., et al., *High Performance Zeolite LTA Pervaporation Membranes on Ceramic Hollow Fibers by Dipcoating-Wiping Seed Deposition.* Journal of the American Chemical Society, 2009. **131**(20): p. 6910-6911.

19. Tomita, T., K. Nakayama, and H. Sakai, *Gas separation characteristics of DDR type zeolite membrane.* Microporous and Mesoporous Materials, 2004. **68**(1-3): p. 71-75.

20. Lai, Z.P., et al., *Microstructural optimization of a zeolite membrane for organic vapor separation.* Science, 2003. **300**(5618): p. 456-460.

21. Mittal, N., et al., *A mathematical model for zeolite membrane module performance and its use for techno-economic evaluation of improved energy efficiency hybrid membrane-distillation processes for butane isomer separations.* Journal of Membrane Science, 2016. **520**: p. 434-449.

22. Katharina Hunger, N.S., Harold B. Tanh Jeazet, Christoph Janiak, Claudia Staudt, Karl Kleinermanns, *Investigation of cross-linked and additive containing polymer materials for membranes with improved performance in pervaporation and gas separation.* Membranes, 2012. **2**(4): p. 727-763.

23. Lai, Z.P., M. Tsapatsis, and J.R. Nicolich, *Siliceous ZSM-5 membranes by secondary growth of b-oriented seed layers.* Advanced Functional Materials, 2004. **14**(7): p. 716-729.

24. *Butanes Market - Global Industry Size, Market Share, Trends, Analysis, And Forecasts 2019 - 2027*. 2020.

25. Arruebo, M., et al., *Separation of hydrocarbons from natural gas using silicalite membranes.* Separation and Purification Technology, 2001. **25**(1-3): p. 275-286.

26. *Natural Gas Market Outlook: How Latin America and the Caribbean Can Benefit from the US Shale Boom*. 2015.

27. Choi, M., et al., *Stable single-unit-cell nanosheets of zeolite MFI as active and long-lived catalysts.* Nature, 2009. **461**(7261): p. 246-249.

28. Varoon, K., et al., *Dispersible Exfoliated Zeolite Nanosheets and Their Application as a Selective Membrane.* Science, 2011. **334**(6052): p. 72-75.

29. Jeon, M.Y., et al., *Ultra-selective high-flux membranes from directly synthesized zeolite nanosheets.* Nature, 2017. **543**(7647): p. 690-694.

30. Gouzinis, A. and M. Tsapatsis, *On the preferred orientation and microstructural manipulation of molecular sieve films prepared by secondary growth.* Chemistry of Materials, 1998. **10**(9): p. 2497-2504.

31. Tung, C.T.P., H.S. Kim, and K.B. Yoon, *Growth of Uniformly Oriented Silica MFI and BEA Zeolite Films on Substrates.* Science, 2011. **334**(6062): p. 1533-1538.

32. Caro, J. and M. Noack, *Zeolite membranes - Recent developments and progress.* Microporous and Mesoporous Materials, 2008. **115**(3): p. 215-233.

33. Zhang, H., et al., *Open-Pore Two-Dimensional MFI Zeolite Nanosheets for the Fabrication of Hydrocarbon-Isomer-Selective Membranes on Porous Polymer Supports.* Angewandte Chemie-International Edition, 2016. **55**(25): p. 7184-7187.

34. Morigami, Y., et al., *The first large-scale pervaporation plant using tubular-type module with zeolite NaA membrane.* Separation and Purification Technology, 2001. **25**(1-3): p. 251-260.

35. Agrawal, K.V., et al., *Oriented MFI Membranes by Gel-Less Secondary Growth of Sub-100 nm MFI-Nanosheet Seed Layers.* Advanced Materials, 2015. **27**(21): p. 3243-3249.

36. Pham, T.C.T., T.H. Nguyen, and K.B. Yoon, *Gel-Free Secondary Growth of Uniformly Oriented Silica MFI Zeolite Films and Application for Xylene Separation.* Angewandte Chemie-International Edition, 2013. **52**(33): p. 8693-8698.

37. Choi, J., et al., *Grain Boundary Defect Elimination in a Zeolite Membrane by Rapid Thermal Processing.* Science, 2009. **325**(5940): p. 590-593.

38. Zhang, B.Q., et al., *Selective Defect-Patching of Zeolite Membranes Using Chemical Liquid Deposition at Organic/Aqueous Interfaces.* Advanced Functional Materials, 2008. **18**(21): p. 3434-3443.

39. Zhou, R.F., et al., *Defect-Patching of Zeolite Membranes by Surface Modification Using Siloxane Polymers for CO2 Separation.* Industrial & Engineering Chemistry Research, 2015. **54**(30): p. 7516-7523.

40. Hong, Z., et al., *A simple method for healing nonzeolitic pores of MFI membranes by hydrolysis of silanes.* Journal of Membrane Science, 2011. **366**(1-2): p. 427-435.

41. Zhang, F.Z., M. Fuji, and M. Takahashi, *In situ growth of continuous b-oriented MFI zeolite membranes on porous alpha-alumina substrates precoated with a mesoporous silica sublayer.* Chemistry of Materials, 2005. **17**(5): p. 1167-1173.

42. Dong, J.H., et al., *Synthesis of MFI-type zeolite membranes on porous-alumina supports by wet gel crystallization in the vapor phase.* Journal of Materials Science, 2003. **38**(5): p. 979-985.

43. Lin, Y.S. and M.C. Duke, *Recent progress in polycrystalline zeolite membrane research.* Current Opinion in Chemical Engineering, 2013. **2**(2): p. 209-216.

44. Tsapatsis, M., *Toward High-Throughput Zeolite Membranes.* Science, 2011. **334**(6057): p. 767-768.

45. Geus, E.R., M.J. Denexter, and H. Vanbekkum, *Synthesis and Characterization of Zeolite (Mfi) Membranes on Porous Ceramic Supports.* Journal of the Chemical Society-Faraday Transactions, 1992. **88**(20): p. 3101-3109.

46. Agrawal, K.V., et al., *Solution-processable exfoliated zeolite nanosheets purified by density gradient centrifugation.* Aiche Journal, 2013. **59**(9): p. 3458-3467.

47. Angelo Basile, A.F., Mohamed Khayet, *Pervaporation, Vapour Permeation and Membrane Distillation: Principles and Applications*. 2015: Woodhead Publishing. 480.

48. Li, D.F., R. Wang, and T.S. Chung, *Fabrication of lab-scale hollow fiber membrane modules with high packing density.* Separation and Purification Technology, 2004. **40**(1): p. 15-30.

49. M.Nageeb Rashed, P.N.P., *Zeolites and Their Applications*. 2018: IntechOpen.

50. Burggraaf, A.J., *Single gas permeation of thin zeolite (MFI) membranes: theory and analysis of experimental observations.* Journal of Membrane Science, 1999. **155**(1): p. 45-65.

51. Krishna, R. and R. Baur, *Modelling issues in zeolite based separation processes.* Separation and Purification Technology, 2003. **33**(3): p. 213-254.

52. Barcia, P.S., et al., *Modeling adsorption equilibria of xylene isomers in a microporous metal-organic framework.* Microporous and Mesoporous Materials, 2012. **155**: p. 220-226.

53. Myers, A.L. and J.M. Prausnitz, *Thermodynamics of Mixed-Gas Adsorption.* Aiche Journal, 1965. **11**(1): p. 121-127.

54. Lee, S., J.H. Lee, and J. Kim, *User-friendly graphical user interface software for ideal adsorbed solution theory calculations.* Korean Journal of Chemical Engineering, 2018. **35**(1): p. 214-221.

55. Krishna, R. and R. Baur, *Analytic solution of the Maxwell-Stefan equations for multicomponent permeation across a zeolite membrane.* Chemical Engineering Journal, 2004. **97**(1): p. 37-45.

56. Krishna, R., *Multicomponent Surface-Diffusion of Adsorbed Species - a Description Based on the Generalized Maxwell-Stefan Equations.* Chemical Engineering Science, 1990. **45**(7): p. 1779-1791.

57. van den Broeke, L.J.P., et al., *Binary permeation through a silicalite-1 membrane.* Aiche Journal, 1999. **45**(5): p. 976-985.

58. Kapteijn, F., et al., *Temperature-Dependent and Occupancy-Dependent Diffusion of N-Butane through a Silicalite-1 Membrane.* Microporous Materials, 1994. **3**(3): p. 227-234.

59. Krishna, R. and J.A. Wesselingh, *Review article number 50 - The Maxwell-Stefan approach to mass transfer.* Chemical Engineering Science, 1997. **52**(6): p. 861-911.

60. Kapteijn, F., J.A. Moulijn, and R. Krishna, *The generalized Maxwell-Stefan model for diffusion in zeolites: sorbate molecules with different saturation loadings.* Chemical Engineering Science, 2000. **55**(15): p. 2923-2930.

61. Vignes, A., *Diffusion in Binary Solutions - Variation of Diffusion Coefficient with Composition.* Industrial & Engineering Chemistry Fundamentals, 1966. **5**(2): p. 189-199.

62. Kosinov, N., et al., *Recent developments in zeolite membranes for gas separation.* Journal of Membrane Science, 2016. **499**: p. 65-79.

63. Rangnekar, N., et al., *Zeolite membranes - a review and comparison with MOFs.* Chemical Society Reviews, 2015. **44**(20): p. 7128-7154.

64. Sanket Sabnis, V.A.T., Chao Li, Jiaxin Zhu, Vivek Vattipalli, Stephen S. Nonnenmann, Guan Sheng, Zhiping Lai, H. Henning Winter, Wei Fan, *Exfoliation of two-dimensional zeolites in liquid polybutadienes.* Chemical Communications, 2017. **53**: p. 7011-7014.

65. Kim, D., et al., *para-Xylene Ultra-selective Zeolite MFI Membranes Fabricated from Nanosheet Monolayers at the Air-Water Interface.* Angewandte Chemie-International Edition, 2018. **57**(2): p. 480-485.

66. Kwon, Y.H., et al., *Ion-Exchanged SAPO-34 Membranes for Krypton-Xenon Separation: Control of Permeation Properties and Fabrication of Hollow Fiber Membranes.* Acs Applied Materials & Interfaces, 2018. **10**(7): p. 6361-6368.

67. Dr. Shaowei Yang, Y.H.K., Prof. Dr. Dong-Yeun Koh, Byunghyun Min, Dr. Yujun Liu, Prof. Dr. Sankar Nair, *Highly Selective SSZ-13 Zeolite Hollow Fiber Membranes by Ultraviolet Activation at Near-Ambient Temperature.* chemnanomat, 2018. **4**.

68. Shete, M., et al., *Nanoscale Control of Homoepitaxial Growth on a Two-Dimensional Zeolite.* Angewandte Chemie-International Edition, 2017. **56**(2): p. 535-539.

69. Davis, T.M., et al., *Mechanistic principles of nanoparticle evolution to zeolite crystals.* Nature Materials, 2006. **5**: p. 400-408.

70. Kim, D., M. Shete, and M. Tsapatsis, *Large-Grain, Oriented, and Thin Zeolite MFI Films from Directly Synthesized Nanosheet Coatings.* Chemistry of Materials, 2018. **30**(10): p. 3545-3551.

71. Korelskiy, D., et al., *An experimental study of micropore defects in MFI membranes.* Microporous and Mesoporous Materials, 2014. **186**: p. 194-200.

72. Zhou, M., et al., *AUniformly Oriented MFI Membrane for Improved CO2 Separation.* Angewandte Chemie-International Edition, 2014. **53**(13): p. 3492-3495.

73. Wang, Q., et al., *Highly (h0h)-oriented silicalite-1 membranes for butane isomer separation.* Journal of Membrane Science, 2017. **540**: p. 50-59.

74. Coronas, J., R.D. Noble, and J.L. Falconer, *Separations of C-4 and C-6 isomers in ZSM-5 tubular membranes.* Industrial & Engineering Chemistry Research, 1998. **37**(1): p. 166-176.

75. Hrabanek, P., et al., *Butane isomer separation with composite zeolite MFI mebranes.* Desalination, 2009. **245**(1-3): p. 437-443.

76. Min, B., et al., *Continuous Zeolite MFI Membranes Fabricated from 2D MFI Nanosheets on Ceramic Hollow Fibers.* Angewandte Chemie-International Edition, 2019. **58**(24): p. 8201-8205.

77. Chen, C.H., et al., *Effect of substrate curvature on microstructure and gas permeability of hollow fiber MFI zeolite membranes.* Aiche Journal, 2018. **64**(9): p. 3419-3428.

78. Keizer, K., et al., *Two component permeation through thin zeolite MFI membranes.* Journal of Membrane Science, 1998. **147**(2): p. 159-172.

79. Alfaro, S., et al., *Preparation of MFI type tubular membranes by steam-assisted crystallization.* Microporous and Mesoporous Materials, 2001. **50**(2-3): p. 195-200.

80. Choi, J., et al., *MFI zeolite membranes from a- and randomly oriented monolayers.* Adsorption-Journal of the International Adsorption Society, 2006. **12**(5-6): p. 339-360.

81. Gora, L., J.C. Jansen, and T. Maschmeyer, *Controlling the performance of silicalite-1 membranes.* Chemistry-a European Journal, 2000. **6**(14): p. 2537-2543.

82. Gora, L., et al., *Highly reproducible high-flux silicalite-1 membranes: optimization of silicalite-1 membrane preparation.* Separation and Purification Technology, 2001. **22-3**(1-3): p. 223-229.

83. Hedlund, J., et al., *High-flux MFI membranes.* Microporous and Mesoporous Materials, 2002. **52**(3): p. 179-189.

84. Xomeritakis, G., et al., *Growth, microstructure, and permeation properties of supported zeolite (MFI) films and membranes prepared by secondary growth.* Chemical Engineering Science, 1999. **54**(15-16): p. 3521-3531.

85. Xomeritakis, G., S. Nair, and M. Tsapatsis, *Transport properties of alumina-supported MFI membranes made by secondary (seeded) growth.* Microporous and Mesoporous Materials, 2000. **38**(1): p. 61-73.

86. Vroon, Z.A.E.P., et al., *Transport properties of alkanes through ceramic thin zeolite MFI membranes.* Journal of Membrane Science, 1996. **113**(2): p. 293-300.

87. van de Graaf, J.M., et al., *Effect of operating conditions and membrane quality on the separation performance of composite silicalite-1 membranes.* Industrial & Engineering Chemistry Research, 1998. **37**(10): p. 4071-4083.

88. Gora, L. and J.C. Jansen, *Hydroisomerization Of C-6 with a zeolite membrane reactor.* Journal of Catalysis, 2005. **230**(2): p. 269-281.

89. Nishiyama, N., et al., *Evaluation of reproducible high flux silicalite-1 membranes: gas permeation and separation characterization.* Separation and Purification Technology, 2001. **22-3**(1-3): p. 295-307.

90. Liu, J.Q., et al., *Butane isomer transport properties of 6FDA-DAM and MFI-6FDA-DAM mixed matrix membranes.* Journal of Membrane Science, 2009. **343**(1-2): p. 157-163.

91. Eum, K., et al., *Zeolitic Imidazolate Framework Membranes Supported on Macroporous Carbon Hollow Fibers by Fluidic Processing Techniques.* Advanced Materials Interfaces, 2017. **4**(12).

92. *February 2020 Monthly Energy Review*. 2020: U.S. Energy Information Administration.

93. *Annual Energy Outlook 2015*. 2015, Energy Information Agency.

94. Saeid Mokhatab, W.A.P.a.J.Y.M., *Handbook of Natural Gas Transmission and Processing Principles and Practices*. 2015: Gulf Professional Publishing.

95. Michael W. Conder, K.A.L., *Production Characteristics Of Liquids-Rich Resource Plays Challenge Facility Design*, in *The American Oil & Gas Reporter*. 2014, National Publishers Group.

96. Baker, R.W., *Future directions of membrane gas separation technology.* Industrial & Engineering Chemistry Research, 2002. **41**(6): p. 1393-1411.

97. Park, J.H., et al., *Techno-economic evaluation of a novel NGL recovery scheme with nine patented schemes for offshore applications.* Journal of Natural Gas Science and Engineering, 2015. **27**: p. 2-17.

98. Scholes, C.A., G.W. Stevens, and S.E. Kentish, *Membrane gas separation applications in natural gas processing.* Fuel, 2012. **96**(1): p. 15-28.

99. Raharjo, R.D., et al., *Pure and mixed gas CH4 and n-C4H10 permeability and diffusivity in poly (dimethylsiloxane).* Journal of Membrane Science, 2007. **306**(1-2): p. 75-92.

100. Thomas, S., et al., *Pure- and mixed-gas permeation properties of a microporous spirobisindane-based ladder polymer (PIM-1).* Journal of Membrane Science, 2009. **333**(1-2): p. 125-131.

101. Pinnau, I. and L.G. Toy, *Transport of organic vapors through poly(1-trimethylsilyl-1-propyne).* Journal of Membrane Science, 1996. **116**(2): p. 199-209.

102. Schmeling, N., et al., *Functionalized copolyimide membranes for the separation of gaseous and liquid mixtures.* Beilstein Journal of Organic Chemistry, 2010. **6**: p. 789-800.

103. Wohlrab, S., et al., *On the performance of customized MFI membranes for the separation of n-butane from methane.* Journal of Membrane Science, 2011. **369**(1-2): p. 96-104.

104. Dragomirova, R., et al., *Desorption-controlled separation of natural gas alkanes by zeolite membranes.* Rsc Advances, 2014. **4**(104): p. 59831-59834.

105. Neubauer, K., et al., *Combination of membrane separation and gas condensation for advanced natural gas conditioning.* Journal of Membrane Science, 2014. **453**: p. 100-107.

106. Dragomirova, R., et al., *Operational Criteria for the Separation of Alkanes by Zeolite Membranes.* Chemie Ingenieur Technik, 2017. **89**(7): p. 926-934.

107. Geus, E.R., et al., *High-Temperature Stainless-Steel Supported Zeolite (Mfi) Membranes - Preparation, Module Construction, and Permeation Experiments.* Microporous Materials, 1993. **1**(2): p. 131-147.

108. Krishna, R. and D. Paschek, *Separation of hydrocarbon mixtures using zeolite membranes: a modelling approach combining molecular simulations with the Maxwell-Stefan theory.* Separation and Purification Technology, 2000. **21**(1-2): p. 111-136.

109. Krishna, R., *Diffusion of binary mixtures across zeolite membranes: Entropy effects on permeation selectivity.* International Communications in Heat and Mass Transfer, 2001. **28**(3): p. 337-346.

110. Poshusta, J.C., R.D. Noble, and J.L. Falconer, *Temperature and pressure effects on CO2 and CH4 permeation through MFI zeolite membranes.* Journal of Membrane Science, 1999. **160**(1): p. 115-125.

111. van de Graaf, J.M., F. Kapteijn, and J.A. Moulijn, *Methodological and operational aspects of permeation measurements on silicalite-1 membranes.* Journal of Membrane Science, 1998. **144**(1-2): p. 87-104.

112. Simon, C.M., B. Smit, and M. Haranczyk, *pyIAST: Ideal adsorbed solution theory (IAST) Python package.* Computer Physics Communications, 2016. **200**: p. 364-380.

113. Krishna, R., et al., *Investigation of slowing-down and speeding-up effects in binary mixture permeation across SAPO-34 and MFI membranes.* Separation and Purification Technology, 2008. **60**(3): p. 230-236.

114. Kim, W.G. and S. Nair, *Membranes from nanoporous 1D and 2D materials: A review of opportunities, developments, and challenges.* Chemical Engineering Science, 2013. **104**: p. 908-924.

115. Flanigen, E.M., et al., *Silicalite, a New Hydrophobic Crystalline Silica Molecular-Sieve.* Nature, 1978. **271**(5645): p. 512-516.

116. Caro, J., et al., *Zeolite membranes - state of their development and perspective.* Microporous and Mesoporous Materials, 2000. **38**(1): p. 3-24.

117. Choi, J., et al., *Uniformly a-oriented MFI zeolite films by secondary growth.* Angewandte Chemie-International Edition, 2006. **45**(7): p. 1154-1158.

118. Cao, Z.S., et al., *Ultrathin ZSM-5 zeolite nanosheet laminated membrane for high-flux desalination of concentrated brines.* Science Advances, 2018. **4**(11).

119. Liu, Y., et al., *Uniform hierarchical MFI nanosheets prepared via anisotropic etching for solution-based sub-100-nm-thick oriented MFI layer fabrication.* Science Advances, 2020. **6**(7).

120. Deng, Z., et al., *Nanocomposite MFI-alumina hollow fibre membranes prepared via pore-plugging synthesis: Influence of the porous structure of hollow fibres on the gas/vapour separation performance.* Journal of Membrane Science, 2010. **364**(1-2): p. 1-8.

121. Das, J.K., N. Das, and S. Bandyopadhyay, *Highly oriented improved SAPO 34 membrane on low cost support for hydrogen gas separation.* Journal of Materials Chemistry A, 2013. **1**(16): p. 4966-4973.

122. Caro, J., M. Noack, and P. Kolsch, *Zeolite membranes: From the laboratory scale to technical applications.* Adsorption-Journal of the International Adsorption Society, 2005. **11**(3-4): p. 215-227.

123. Yang, S.W., Y.D. Chiang, and S. Nair, *Scalable One-Step Gel Conversion Route to High-Performance CHA Zeolite Hollow Fiber Membranes and Modules for CO2 Separation.* Energy Technology, 2019. **7**(9).

124. Bai, C.S., et al., *Preparation and Separation Properties of Silicalite Composite Membranes.* Journal of Membrane Science, 1995. **105**(1-2): p. 79-87.

125. Yan, Y.S., M.E. Davis, and G.R. Gavalas, *Preparation of Zeolite Zsm-5 Membranes by in-Situ Crystallization on Porous Alpha-Al2o3.* Industrial & Engineering Chemistry Research, 1995. **34**(5): p. 1652-1661.

126. Algieri, C., et al., *Preparation of thin supported MFI membranes by in situ nucleation and secondary growth.* Microporous and Mesoporous Materials, 2001. **47**(2-3): p. 127-134.

127. Lee, J.B., et al., *High selectivities in defective MFI membranes.* Journal of Membrane Science, 2008. **321**(2): p. 309-315.

128. Miachon, S., et al., *Nanocomposite MFI-alumina membranes via pore-plugging synthesis - Preparation and morphological characterisation.* Journal of Membrane Science, 2006. **281**(1-2): p. 228-238.

129. Fan, S.J., et al., *Fabrication of zeolite MFI membranes supported by alpha-Al2O3 hollow ceramic fibers for CO2 separation.* Journal of Materials Research, 2013. **28**(13): p. 1870-1876.

130. Vroon, Z.A.E.P., et al., *Preparation and characterization of thin zeolite MFI membranes on porous supports.* Journal of Membrane Science, 1998. **144**(1-2): p. 65-76.

131. Jin, H., et al., *Length dependency of hydrocarbon adsorption on nanostacked MFI zeolite by tracer chromatography.* Applied Surface Science, 2010. **256**(17): p. 5508-5512.

132. Avila, A.M., et al., *Concentration polarization in SAPO-34 membranes at high pressures.* Journal of Membrane Science, 2009. **335**(1-2): p. 32-36.

133. Li, Y.S. and W.S. Yang, *Microwave synthesis of zeolite membranes: A review.* Journal of Membrane Science, 2008. **316**(1-2): p. 3-17.

134. Yang, S.W., et al., *Highly Selective SSZ-13 Zeolite Hollow Fiber Membranes by Ultraviolet Activation at Near-Ambient Temperature.* Chemnanomat, 2019. **5**(1): p. 61-67.

135. Choi, J. and M. Tsapatsis, *MCM-22/Silica Selective Flake Nanocomposite Membranes for Hydrogen Separations.* Journal of the American Chemical Society, 2010. **132**(2): p. 448-449.